Spin Degrees of Freedom in Electromagnetic Nuclear Physics

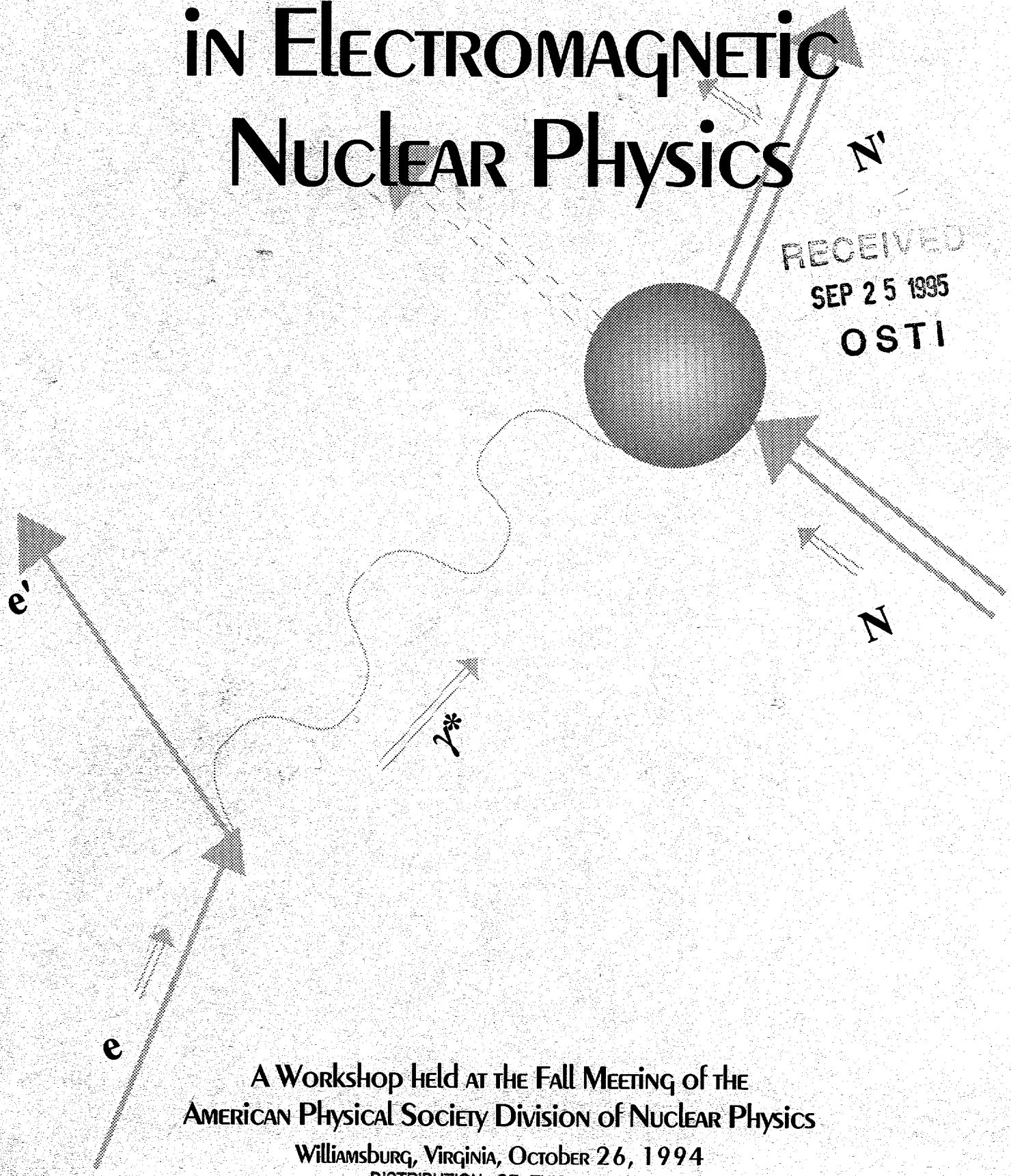

A Workshop Held at the Fall Meeting of the
American Physical Society Division of Nuclear Physics
Williamsburg, Virginia, October 26, 1994

DISCLAIMER

Portions of this document may be illegible in electronic image products. Images are produced from the best available original document.

CEBAF R–94–004

Spin Degrees of Freedom in Electromagnetic Nuclear Physics

26 October 1994

Workshop Chair
Volker Burkert, CEBAF

The Continuous Electron Beam Accelerator Facility (CEBAF) is a national physics user facility managed by the Southeastern Universities Research Association (SURA), Inc., for the U.S. Department of Energy (DOE) under contract DE-AC05-84ER40150.

For more information or copies of this report contact:

CEBAF User Liaison Office, MS 12B
12000 Jefferson Avenue
Newport News, VA 23606
Phone: (804) 249–7586
Fax: (804) 249–7398
E-mail: users@cebaf.gov

Table of Contents

PREFACE

On 26 October 1994 a workshop on Spin Degrees of Freedom in Electromagnetic Nuclear Physics was held in conjunction with the Fall meeting of the American Physical Society Division of Nuclear Physics (APS DNP). One hundred twenty–nine scientists registered for this one–day workshop to discuss technical as well as physics issues related to use of polarized electron and photon beams, polarized solid state targets, and recoil polarimetry.

Although presently limited to relatively low–current electron sources with high polarization using strained GaAs crystal, these sources have already been used in experiments where the current was limited due to other factors such as the performance of the polarized target. Many of the upcoming experiments at electron accelerators will greatly benefit from the implementation of such a source.

Additionally, new and potentially fruitful developments have been reported in the area of polarized photon beams based on Compton backscattering. An important advantage of this technique over coherent bremsstrahlung beams is that the photon flux is concentrated at the high energy part of the spectrum thus eliminating much of the background problems present in bremsstrahlung beams.

Furthermore, recoil polarimetry is becoming a mature technique. Recoil polarimeters have been calibrated up to 2.4 GeV for protons and 700 MeV for deuterons and are now being used as focal plane polarimeters in magnetic spectrometers.

The workshop's talks also included the latest experimental results from the polarized structure function measurements on hydrogen and deuterium targets at SLAC and CERN, and the interpretation of polarized structure function measurements in the deep inelastic region and at low momentum transfers.

Other topics included the upcoming measurements of polarization observables in $(e,e'p)$ reactions on nuclear reactions and in experiments on the nucleon to study electromagnetic and weak formfactors of the ground–state nucleon as well as excited baryon states.

An obvious conclusions of the workshop: the use of spin polarization in electromagnetic nuclear physics at intermediate energies will greatly enhance the potential of the experiments to discover new phenomena.

Volker Burkert, workshop chair
July, 1995

Spin Polarization in Electromagnetic Physics at Intermediate Energies

Volker D. Burkert
CEBAF, 12000 Jefferson Avenue, Newport News, Virginia 23606, USA

ABSTRACT

Aspects of the spin responses functions of protons and neutrons at low and intermediate momentum transfers and energy transfers are discussed, with emphasis on the region of the nucleon resonances. Experiments at CEBAF will use polarization to measure inclusive asymmetries A_1^p, A_2^p and A_1^n in a large Q^2 and W range, the electric formfactor of the neutron, and resonance excitations in pion and vector meson production.

1. Introduction

The results of measurements at CERN[1–3] and at SLAC[5,4] on the deep inelastic polarized proton structure functions have prompted intense theoretical research about the spin structure of the nucleon in the deep-inelastic region. Surprisingly, the spin of the proton and neutron appear to be carried mostly by objects other than quarks. It is worth noting that some of the experiments on the neutron use data sets with Q^2 as low as 1 GeV^2. While such low Q^2 values have been used in the analysis of unpolarized lepton scattering there is lack of convincing evidence that polarized structure functions exhibit true scaling behavior at such low Q^2. Moreover, the W range used in these analyses ($W \geq 2\ GeV$) overlaps part of the resonance region. Resonant states have been observed for masses up to 2.8 GeV/c^2 and many more states are predicted to exist in the mass region above 2.0 GeV. This raises the question what their contributions are to the spin sum rules and how to correct for them when interpreting the measurements in terms of the total spin carried by quarks. As the conclusion about the nucleon spin rests on relatively small differences between theoretical predictions and the data it is important to study such contributions before far-reaching conclusions about the origin of the nucleon spin may be drawn.

Studies of the spin structure function of the nucleon in the resonance region and at low ν are interesting in their own right. The study of the non-perturbative regime of the strong interaction was one of the main motivations for the construction of continuous wave electron accelerators at various locations around the world. CEBAF, in particular, with its initial maximum energy of 4 GeV will play an important role in unravelling the spatial and spin structure of the light quark baryons in this regime.

One of the major programs at CEBAF is the study of excited states of the proton and neutron, and the measurement of their transition formfactors from the ground state nucleon.[6] The formfactors contain information on both the internal spatial structure as well as the spin structure of the transition. The expected accuracy and completeness of the experimental data should improve the empirical information about the known states dramatically, and should generate significant information about predicted, yet undiscovered states.

Microscopic models of the nucleon structure, such as relativistic versions of the quark model, bag models, QCD sum rules, and others may be tested in detail against these results. Significant improvements of our understanding of the strong interaction force in the non-perturbative regime will hopefully result from this effort.

The nucleon is likely more complex than the simple constituent quark picture suggests. Gluonic excitations, or hybrids, may play an active role in spectroscopy, and pionic contributions may be important at small momentum transfers. The nucleon may be written as a Fock state expansion:

$$|N>=\alpha|q^3>+\beta|q^3G>+\gamma|q^3(q\bar{q})>+\ldots$$

Understanding the relative importance of these contributions is necessary for a detailed understanding of the nucleon structure. For example, while gluonic excitations have been predicted by QCD inspired models, solid evidence for such states is still lacking. From a comparison with the quark model, we can learn whether the strength of the $|q^3>$ states can exhaust the full resonant strength of the spin integrals. If this is the case, there will be little room left for gluonic or other states. The opposite is also correct, a lack of 3-quark strength in the spin integral would provide evidence for non-quark contributions to the spin sum rules.

Another possibility is that some of the proton spin resides in orbital angular momentum contributions. Such contributions are necessarily associated with extended objects and therefore cannot be probed in deep inelastic scattering, but they may be accessible at lower energies and momentum transfers. The low Q^2, ν region may therefore contain significant information about the internal spin structure of the nucleon.

Finally, measurement of the polarization asymmetries at low Q^2 and ν will provide constraints for models describing the Q^2 evolution of the polarized structure functions from the deep inelastic to the confinement regime.

2. The Structure of the Nucleon.

The interest in the structure of the ground state nucleon, its excited states, and their role in nuclear properties has dramatically increased in recent years and is one of the major motivations in support of the experimental program at the new electron machines. The structure of the nucleon may be probed in elastic electron nucleon scattering and in inelastic reactions induced by electrons or photons. These experiments measure the charge and current distribution of the nucleons and the transition currents of their excitations. Knowledge of these quantities allows tests of models describing the nucleon structure at low and intermediate energy and momentum transfers. With increasing momentum transfer Q^2 the transition from the

non-perturbative regime to the perturbative regime can be studied, where simple quark counting rules and power laws may apply.[7] Many of the relevant experiments either require measurement of spin observables, or the sensitivity to fundamental quantities is increased significantly in spin observables.

2.1. Electromagnetic Formfactors.

In elastic electron nucleon scattering the hadronic current is specified by the electric and magnetic Sachs formfactors $G_E(Q^2)$ and $G_M(Q^2)$. The usual technique for measuring the elastic formfactors is the Rosenbluth separation, where one makes use of the different angular dependence of the electric and the magnetic term in the unpolarized elastic cross section to separate $|G_E|$ and $|G_M|$.

$$\frac{d\sigma}{d\Omega} = (\frac{d\sigma}{d\Omega})_M \frac{E'}{E}[(G_E^2 + \tau G_M^2) + 2\tau(1+\tau)G_M^2 tg^2\frac{\theta}{2}] \tag{2}$$

where $\tau = \frac{Q^2}{4M^2}$. This technique ceases to be useful, when either $G_E^2 \ll G_M^2$, or at high values of Q^2, where the magnetic contribution dominates both the angular dependent and the angular independent term. Experimental information on the neutron electric formfactor G_{En} is rather poor for all non-zero Q^2. In the absence of a free neutron target, we have to rely on scattering from the few-nucleon systems. Unlike for the proton, the Rosenbluth separation of G_{En} from G_{Mn} is difficult even at low Q^2 because of the small size of G_{En} compared to G_{Mn}. The slope of G_{En} versus Q^2 has been accurately measured at low Q^2, and it is positive, indicating that the neutron appears to have a slightly positive core surrounded by a region of negative charge. At $Q^2 < 1\ GeV^2$, G_{En} has been extracted from elastic electron-deuteron scattering data. Using this procedure it is necessary to assume a model for the deuteron structure. The most recent analysis[8] allows for a 15% systematic uncertainty in G_{En} for $Q^2 < 0.8 GeV^2$. For larger values of Q^2, uncertainties in the deuteron wavefunction render this method unreliable.

The electric formfactor of the proton has been measured at SLAC using Rosenbluth separation for Q^2 up to about 6 GeV^2, with error bars of 20% at the highest momentum transfer. The proton magnetic formfactor has been measured for Q^2 up to 31 GeV^2. Knowledge of the neutron magnetic formfactor comes from inclusive quasi-elastic eD scattering at $Q^2 < 20\ GeV^2$, where the proton contribution has been subtracted using elastic ep scattering data. G_{Mn} is poorly known, with large systematic uncertainties. Our knowledge of G_{Mn} should improve significantly with new experiments at MAMI[11] and CEBAF.[12]

2.2. Polarization Techniques to Measure G_{En} and G_{Ep}

Two methods appear very promising in that they allow measurement of the ratio G_{En}/G_{Mn} in a model independent fashion even if $G_{En} << G_{Mn}$. Both methods employ quasi elastic scattering of polarized electrons off deuterium. In the first method, proposed by Dombey[13] for measurement of the electric formfactor of the proton, electrons are scattered off a polarized hydrogen or deuterium target.[14] The second method uses an unpolarized deuterium (hydrogen) target and the polarization

of the recoil neutron (proton) is measured in a second scattering experiment.[15] Both methods are equivalent, and allow measurement of the polarization asymmetry

$$A_{en} = \frac{2\tau cos\theta v'_T + 2\sqrt{2\tau(1+\tau)} \cdot (G_{En}/G_{Mn}) sin\theta cos\phi v'_{TL}}{v_L(1+\tau)(G_{En}/G_{Mn})^2 + 2\tau v_T} \qquad (3)$$

where v_L,v_T,v'_T, v'_{TL} are known kinematic quantities and ϕ and θ define the orientation of the nucleon spin relative to the scattering plane.. By varying θ, the angle between the nucleon spin and the direction of momentum transfer, it is possible to separate the longitudinal and transverse pieces of the quasi elastic spin-dependent cross section. In particular, if $\theta = 90°$, the asymmetry is proportional to G_{En}/G_{Mn}. Knowing G_{Mn} the electric formfactor can be determined. The first method uses a polarized deuterium (or ^3He) target, either as an ultra thin gas target in an electron storage ring, or a solid state target (ND_3), or a dense ^3He gas target, in an external electron beam. In case the polarization asymmetry is measured using vector polarized deuterium, it will be necessary to measure the recoil neutron in coincidence with the scattered electron to eliminate the much larger contributions to the asymmetry from the polarized proton in the deuteron. Model calculations[16] show that the polarization asymmetry is linearly dependent on G_{En}/G_{Mn} as long as the recoil neutron is emitted at small angles with respect to the direction of the virtual photon. In this region the influence of the deuteron wave function on the extracted value of G_{En}/G_{Mn} is nearly absent. A quantitative check can be accomplished by measuring the proton asymmetry at the same time, and by comparing it to the asymmetry obtained with a polarized hydrogen target (e.g. NH_3). For ^3He, nuclear corrections are not negligible and have to be carefully taken into account when extracting G_{En}.

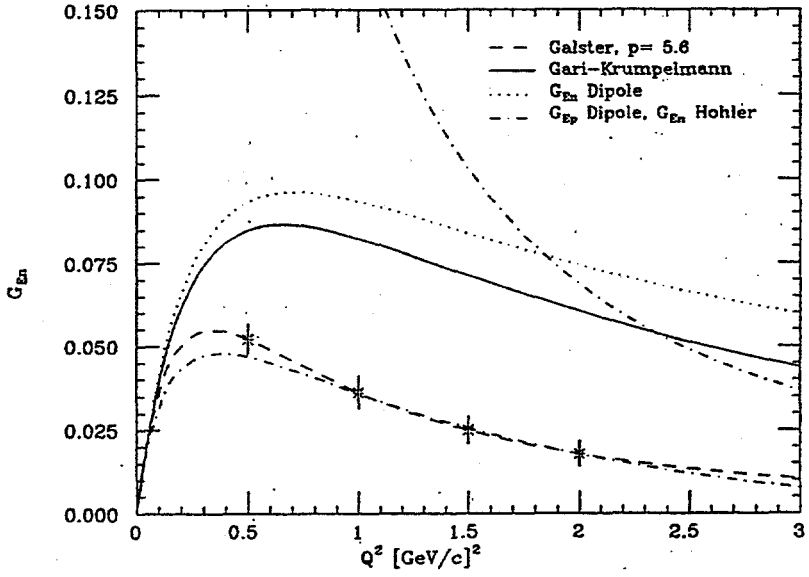

Figure 1: Projected errors for a measurement of G_{en} at CEBAF using the recoil polarization technique

Employing state of the art polarized target technology[10] it appears feasible to measure G_{En} for Q^2 up to 0.5 GeV^2 with a 1 GeV electron beam, and up to 2 or 3 GeV^2 using a 4 GeV beam. The first pilot experiments at MIT-Bates and at MAMI[11] have smaller systematic errors than elastic eD scattering experiments, but still show large statistical uncertainties. This situation should change in the near future with improved measurements under way at MAMI. Projected error bars for a measurement at CEBAF which employs the recoil polarization technique are shown in Figure 1. The polarization techniques can also be used to measure the electric formfactor G_{Ep} of the proton. Most promising in this respect is the recoil polarization techniques using an unpolarized hydrogen target.[9] With a 4 GeV beam values of Q^2 up to 5 GeV^2 can be reached using this technique.

3. Inclusive Polarized Structure Functions of the Nucleon

The spin-structure of the nucleon is usually discussed in terms of the deep-inelastic scaling structure function $g_1(x)$. In the kinematical regime of resonances and low Q^2, use of total helicity $\frac{1}{2}$ and $\frac{3}{2}$ photon-nucleon absorption cross sections is more convenient. If beam and target are longitudinally polarized, the double polarized inclusive electron scattering cross section may be written as:

$$\frac{d\sigma}{d\Omega dE'} = \Gamma_T\{\sigma_T + \epsilon\sigma_L \pm \sqrt{1-\epsilon^2}\cos\psi\sigma_T A_1 \pm \sqrt{2\epsilon(1-\epsilon)}\sin\psi\sigma_T A_2\} \qquad (4)$$

where ψ is the angle between $\vec{q}$ and the target polarization vector, σ_T and σ_L are the transverse and longitudinal total photon absorption cross section, and the sign $\pm$ is related to the sign of the product of beam and target polarization (assumed to be unity). A_1 and A_2 are the polarized asymmetries:

$$A_1 = \frac{\sigma^T_{1/2} - \sigma^T_{3/2}}{\sigma^T_{1/2} + \sigma^T_{3/2}} \qquad (5)$$

$$A_2 = \frac{\sigma^{TL}}{\sigma^T_{1/2} + \sigma^T_{3/2}} \qquad (6)$$

where $\sigma^T_{1/2}(Q^2,\nu)$ and $\sigma^T_{3/2}(Q^2,\nu)$ are the transverse total absorption cross sections for total helicity $\lambda_{\gamma N} = \frac{1}{2}$ and $\lambda_{\gamma N} = \frac{3}{2}$, respectively. A_1 is limited to:

$$-1 \leq A_1 \leq +1 \ ,$$

and A_2 is a transverse-longitudinal interference term with an upper bound of:

$$A_2 \leq \sqrt{\frac{\sigma_L}{\sigma_T}} \qquad (7)$$

At $Q^2 = 0$, the sum rule by Gerasimov,[17] and Drell and Hearn[18] (GDH) relates the difference in the total photoabsorption cross section on nucleons for $\lambda_{\gamma N} = \frac{1}{2}$ and $\lambda_{\gamma N} = \frac{3}{2}$ to the anomalous magnetic moment of the target nucleon.

$$I^{GDH} = \frac{M^2}{8\pi^2\alpha}\int_{\nu_{thr.}}^{\infty}\frac{d\nu}{\nu}(\sigma^T_{1/2}(\nu) - \sigma^T_{3/2}(\nu)) = -\frac{1}{4}\kappa^2 \qquad (8)$$

In the deep inelastic regime the first moment of the spin structure function is given by:

$$\Gamma_1(Q^2) = \int_0^1 A_1(x,Q^2)\cdot F_1(x,Q^2)dx$$

$$= \frac{Q^2}{16\pi^2\alpha}\int_{\nu_{thr.}}^{\infty}(1-x)(\sigma^T_{1/2}(\nu,Q^2)-\sigma^T_{3/2}(\nu,Q^2))\frac{d\nu}{\nu}$$

For $Q^2 \to 0$,

$$\Gamma_1(Q^2) \longrightarrow \frac{Q^2}{16\pi^2\alpha}\int_{\nu_{thr.}}^{\infty}(\sigma^T_{1/2}(\nu,Q^2)-\sigma^T_{3/2}(\nu,Q^2))\frac{d\nu}{\nu} \tag{9}$$

$$\Gamma_1(Q^2) \longrightarrow \frac{Q^2}{2M^2}I_p(Q^2)$$

The slope of $\Gamma_1(Q^2)$ at $Q^2 = 0$ is thus determined by the GDH sum rule (eqn.(8)). Since the slope is negative, and $\Gamma_1^p > 0$ in the deep inelastic regime, $\Gamma_1(Q^2)$ must have a zero crossing at finite Q^2 to satisfy the GDH sum rule. In the deep inelastic region, Γ_1^p shows no indication of approaching such a zero at $Q^2 > 2\ GeV^2$.

In order to reconcile the GDH sum rule with the EMC results, dramatic changes in the helicity structure must occur when going from $Q^2 = 0$ to finite values of Q^2. Anselmino, Ioffe and Leader[21] attempted to connect the GDH sum rule with the Ellis-Jaffe sum rule in the deep inelastic region using the vector dominance model analogy. The resulting strong Q^2 dependence was found to be in disagreement with the EMC data. An analysis of electroproduction data by Burkert and Li[19] showed that contributions of the $\Delta(1232)$ to $I_p(Q^2)$ are dominant at small Q^2, and contributions from other resonances become significant with increasing Q^2, causing $I_p(Q^2)$ to change sign at Q^2 between 0.5 to 1.0 GeV^2. Burkert and Ioffe[22,23] extended the model by Anselmino et al. to account for the resonance contributions. The following expression was used:

$$I_{p,n}(Q^2) = \sum I^{Res}_{p,n}(Q^2) + 2M_p^2\Gamma^{as}_{p,n}\left[\frac{1}{Q^2+m_\rho^2} - \frac{c_{p,n}m_\rho^2}{(Q^2+m_\rho^2)^2}\right] \tag{10}$$

The parameters $c_{p,n}$ are fixed by requiring $I_{p,n}(0) = I^{GDH}_{p,n}$. For the proton, the model is constraint to reproduce the deep inelastic data from CERN at $Q^2 = 10.7\ GeV^2$, and for the neutron the SLAC E142 data at $Q^2 = 2\ GeV^2$ are used. Resonance contributions are found to be significant at $Q^2 \leq 3\ GeV^2$ (Figure 2), and affect the interpretation of the results of the CERN and SLAC data[23] .

The GDH integral for the neutron is of special interest at low Q^2 for testing predictions of the quark model. In the $SU(3)\otimes SU(2)\otimes O(3)$ basis the GDH sum rule contains contributions from the $\gamma N\Delta(1232)$ transition only[24,25]:

$$I_n^{GDH}(Q^2) = I_n^{\Delta(1232)}(Q^2)$$

This prediction is based on the symmetry properties of the quark model; a deviation would indicate a breaking of the symmetry and demonstrate the limitations of the nonrelativistic quark model. An extensive discussion of the GDH sum rule and the quark model is given by Drechsel and Giannini.[26]

The proton-neutron difference $\Delta I_{pn}(Q^2)$ as a function of Q^2 allows study of the transition from the Bjorken sum rule, which is expected to be valid in the deep inelastic region only, to the GDH sum rule at $Q^2 = 0$. In ΔI_{pn} the dominant $\Delta(1232)$ contribution is absent. ΔI_{pn} is therefore sensitive to isospin 1/2 resonance contributions, especially to the lowest mass state $P_{11}(1440)$. The 3-quark nature of this state has been disputed recently. Calculations of transition form factors assuming it is a gluonic excitation[27] of the nucleon rather than a radial 3-quark excitation give better agreement with the experimental amplitudes. As shown in Figure 3, measurements of ΔI_{pn} are sensitive to the QCD structure of this state. The GDH value is $\Delta I_{pn}(0) = +0.114$. The analysis[28,29] of single pion photoproduction data is consistent with the analysis of electroproduction data[19,20] extrapolated to the photon point (Figure 2). Both analyses indicate a discrepancy with the GDH sum rule. A violation of the GDH sum rule would be a significant though not completely unexpected finding. In recent theoretical work on extended current algebra[30] it is suggested that the GDH sum rule needs to be extended. Interestingly enough, the discrepancy observed in the empirical analyses is qualitatively consistent with this prediction. On the other hand, it is possible that contributions from the high energy region, or contributions from sources other than the observed resonances account for the missing strength in ΔI_{pn}. Also, electroproduction data on the neutron are sparse, and the analysis relies on symmetry arguments to determine the amplitudes for many of the higher mass states.

A direct measurement of the GDH integral for $Q^2 < 2\ GeV^2$ is necessary to test the GDH sum rule and to study its Q^2 evolution and transition to the deep inelastic scaling behavior.

4. Inclusive Polarized Electron Scattering Experiments at CEBAF

Experiment 91-023[33] will use the CEBAF Large Acceptance Spectrometer[34] to measure the asymmetries $A_1^p(Q^2,\nu)$, and $A_2^p(Q^2,\nu)$ on the proton. The experimental arrangement is shown in Figure 4. The $^{15}NH_3$ target will be polarized along the beam axis. In order to separate A_1 and A_2 the experimental asymmetry

$$A \equiv \frac{\frac{d\sigma(\uparrow\downarrow)}{d\Omega dE'} - \frac{d\sigma(\uparrow\uparrow)}{d\Omega dE'}}{\frac{d\sigma(\uparrow\downarrow)}{d\Omega dE'} + \frac{d\sigma(\uparrow\uparrow)}{d\Omega dE'}} = P_e \cdot P_p \cdot D[A_1(Q^2,\nu) + \eta A_2(Q^2,\nu)] \qquad (11)$$

$$D = \frac{\sqrt{1-\epsilon^2}\cos\psi}{1+\epsilon R};\ \eta = \sqrt{\frac{2\epsilon}{1+\epsilon}}\tan\psi$$

will be measured at fixed Q^2 and W but at different beam energies, giving different values for η. ψ is the angle between the polarization axis and $\vec{q}$. The experiment will measure the angular range for about 13° to 48° over most of the azimuthal angle

range simultaneously. The solid angle covered is $\Delta\Omega = 1.2$ sr. In the asymmetry, many systematic uncertainties, e.g. due to limited knowledge of the acceptance, will

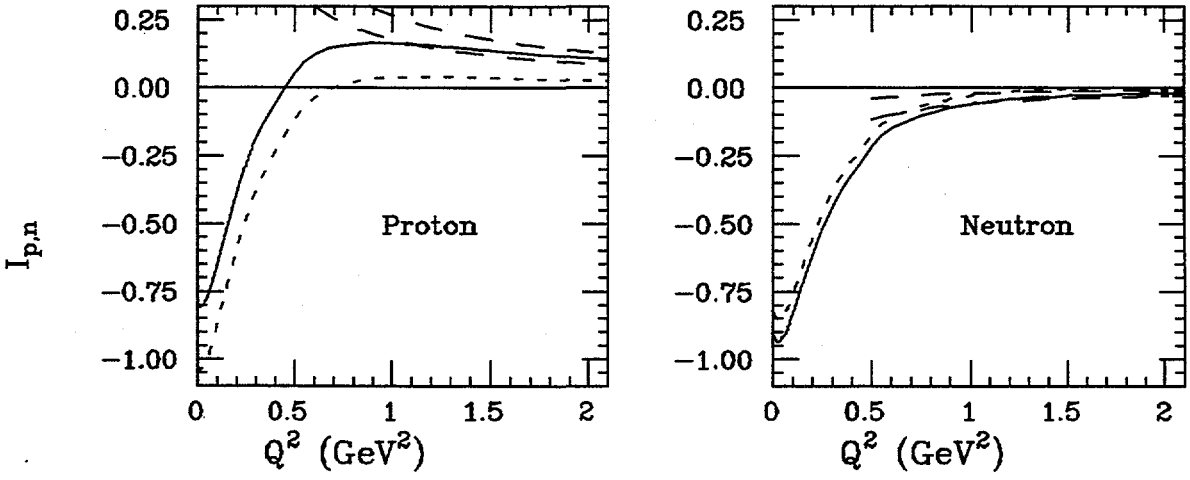

Figure 2: The integral $I_{p,n}(Q^2)$. The short dashed lines represent resonance contributions for proton (sign changing curve) and neutron, respectively. The solid lines include VDM contributions and are normalized to the GDH value at the photon point and to reproduce the EMC data on the proton, and the E142 data on the neutron, respectively. The dashed lines represent a $1/Q^2$ extrapolatation of the EMC results for protons (positive value), and of the E142 results for neutrons (negative value), respectively.

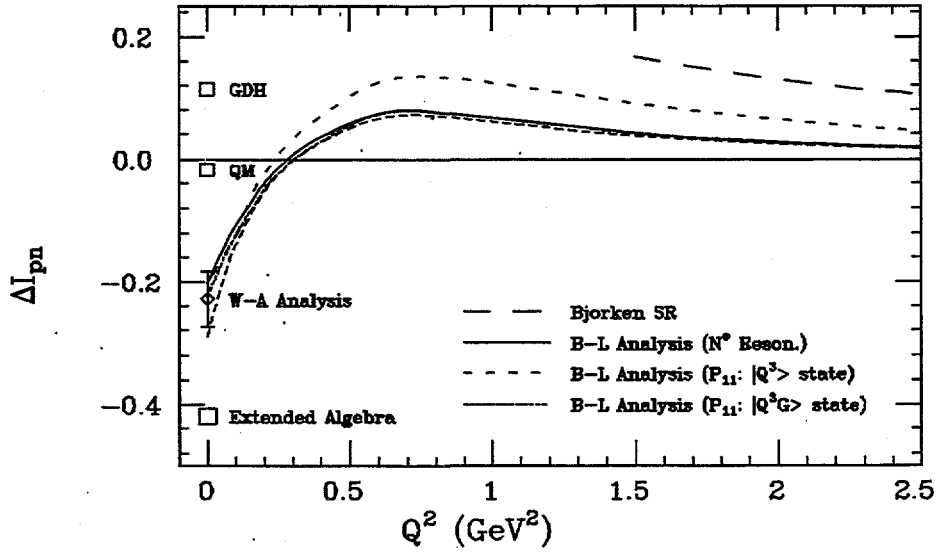

Figure 3: Result of the analysis of electroproduction of baryon resonances for the proton - neutron difference if only resonances are included.[19,20] QM denotes the quark model point, using photocoupling amplitudes of Capstick.[32] Also shown is a proposed extension of the GDH sum rule using extended current algebra.[30]

cancel. Uncertainties due to the limited knowledge of beam and target polarization will be greatly reduced by measuring the elastic asymmetry:

$$A_{ep} = P_e \cdot P_p \cdot f(G_E/G_M) \ , \tag{12}$$

simultaneously. A_{ep} is a function of the ratio of electric and magnetic form factors, and the product of beam and target polarization. Since the form factors at small Q^2 are known very accurately, $P_e \cdot P_p$ can be determined to $\delta(P_e \cdot P_p) \leq 0.01$.

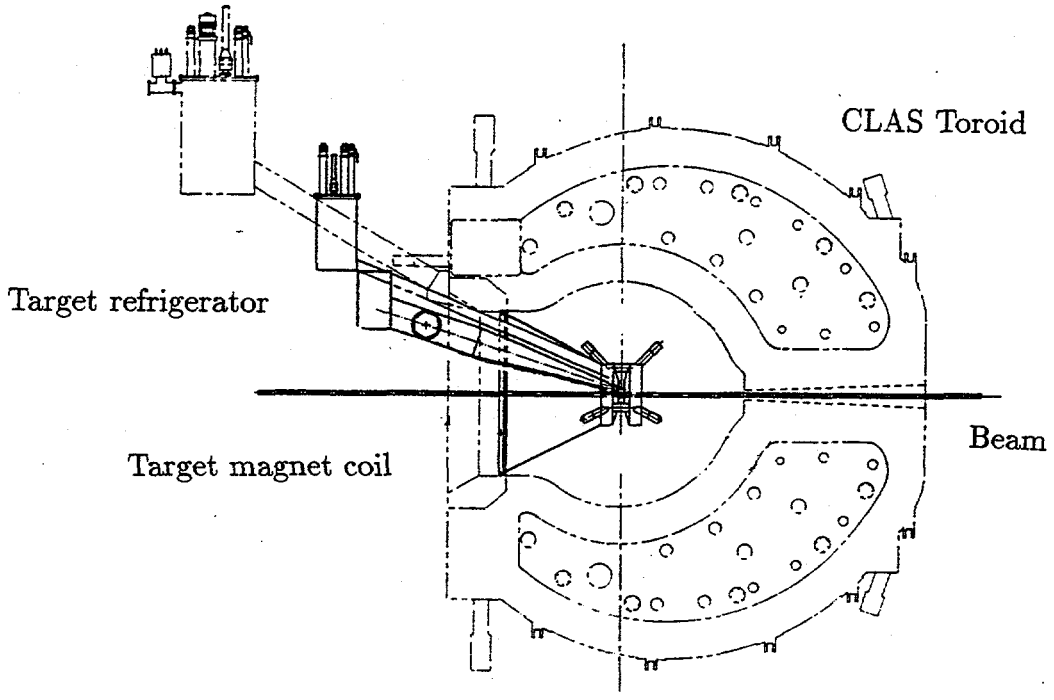

Figure 4: Arrangement of CEBAF experiment 91-023 in the CLAS toroidal magnet (detectors are not shown). The target is polarized parallel or anti-parallel to the beam axis.

Figure 5 shows expected experimental asymmetries for different beam energies. A fit of eqn(8) at fixed Q^2 and W will allow the determination of A_1 and A_2, separately. Expected error bars for the asymmetries are shown in Figure 6, where data previously measured by a SLAC/Yale experiment at $Q^2 = 0.5\ GeV^2$ are included for comparison. Asymmetries for about 10 values of Q^2 between 0.15 GeV^2 and 2 GeV^2 will be measured. In case A_2 is known from some other source, e.g. from an analysis of unpolarized pion electroproduction data, A_1 can be determined with considerably reduced error bars. The integral

$$I_p(Q^2) = \int_{\nu_{thr}}^{\nu(W \leq 2GeV)} 2\sigma_T A_1 \frac{d\nu}{\nu} \tag{13}$$

will be determined with projected errors as shown in Figure 7.

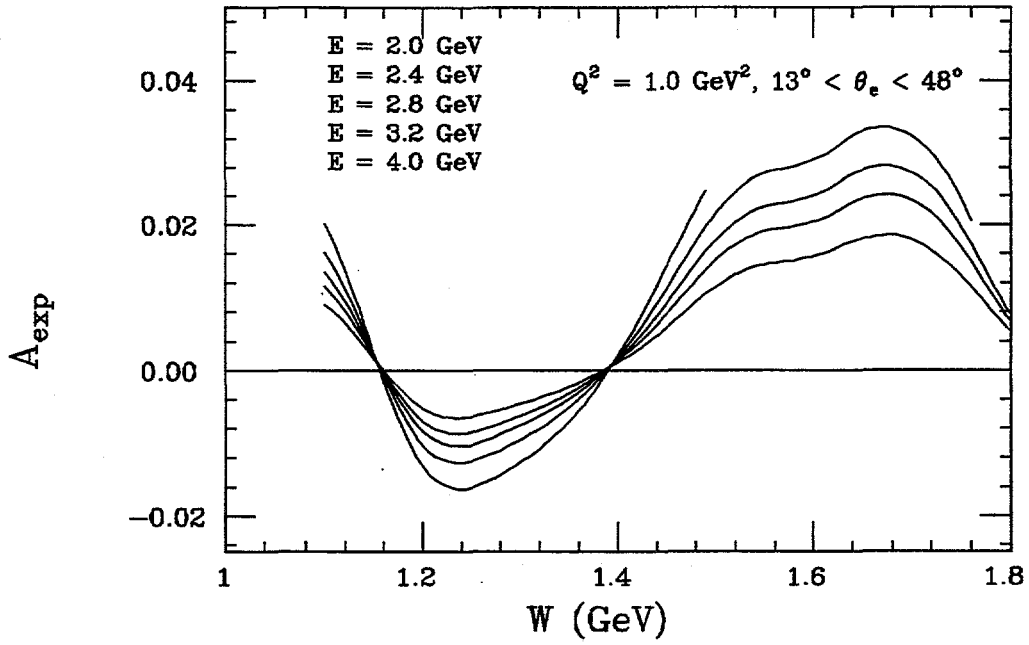

Figure 5: Expected experimental asymmetries for different beam energies but fixed Q^2 and W. A fit of eqn.(9) to A at different energies allows the separation of A_1 and A_2.

Experiment 93-009[35] will measure the low Q^2 behavior of $I_n(Q^2)$ using a $^{15}N\vec{D}_3$ target. The two experiments combined allow determination of the GDH integral for masses up to $W = 2.2\ GeV$ for the neutron, as well as for the proton-neutron difference ΔI_{pn}. Calculations show that A_2^n may be small,[39] and one may extract A_1^n from eqn. (12) assuming $A_2^n = 0$. Figure 8 shows the expected errors for the experimental asymmetry $(A/D)\sigma_T$ on the neutron. Obviously, a very significant determination of $\Delta I_{pn}(Q^2)$ will be possible (Figure 9).

4.1. Studying the GDH sum rule

A direct measurement of the GDH sum rule requires circularly polarized energy tagged photons and a longitudinally polarized target with as little solid angle obstruction as possible. Since the experiments require a measurement of the absolute total absorption cross section a near 4π coverage is important to keep corrections small. While a direct measurement of $\sigma_{1/2}$ and $\sigma_{3/2}$ is planned at MAMI and ELSA, an experiment at CEBAF[41] will measure the dominant one pion and two pion contributions in exclusive measurements. This should allow more accurate corrections for the missing strength in the exclusive channels.

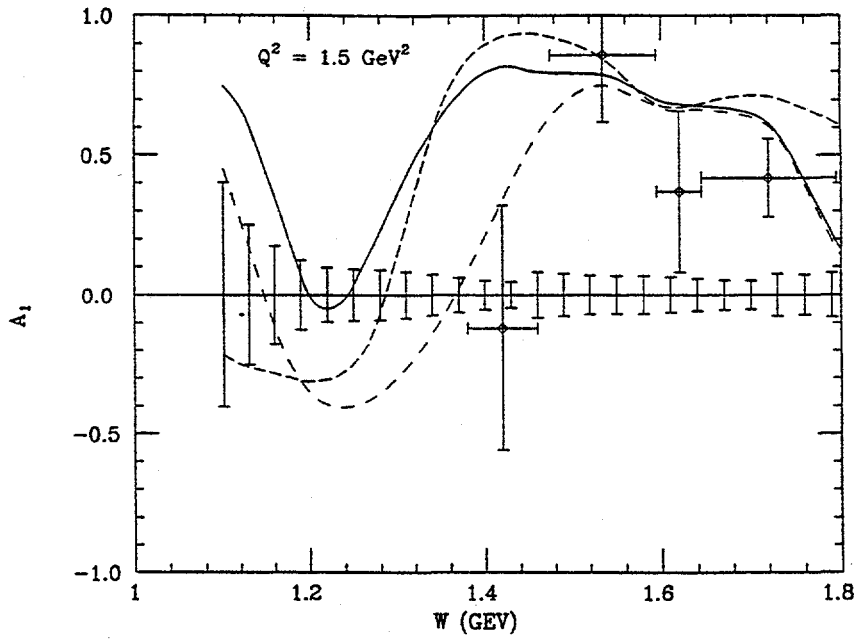

Figure 6: Expected statistical errors in experiment 91-023[33] for asymmetry $A_1(Q^2, W)$ compared with SLAC/Yale data.[36]

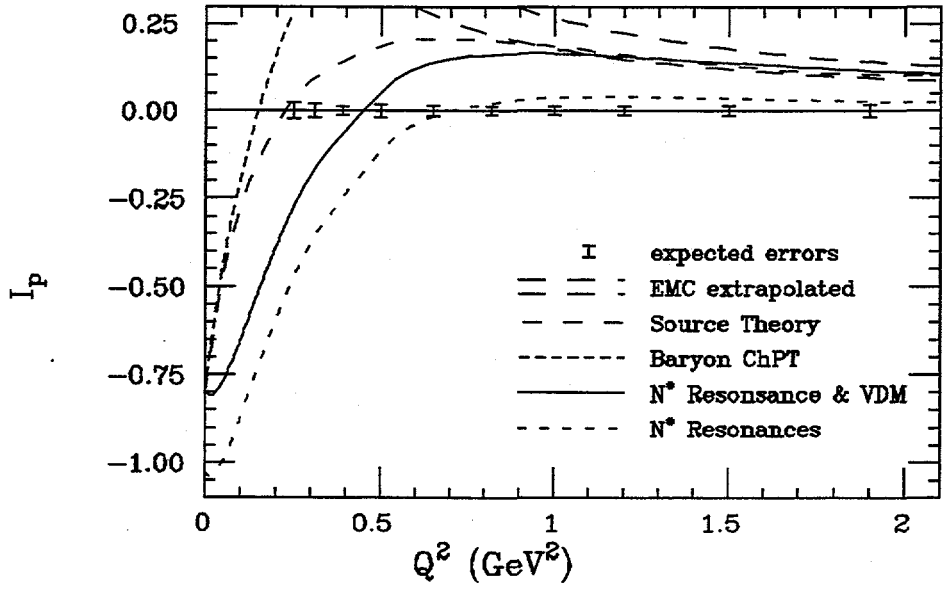

Figure 7: Expected errors for $I_p(Q^2)$ from experiment 91-023 in comparison to model calculations: short dashes - chiral perturbation theory,[38] long dashes - source theory,[37] dotted - resonance contributions,[19,20] solid - resonances + vector meson dominance model[22,23]

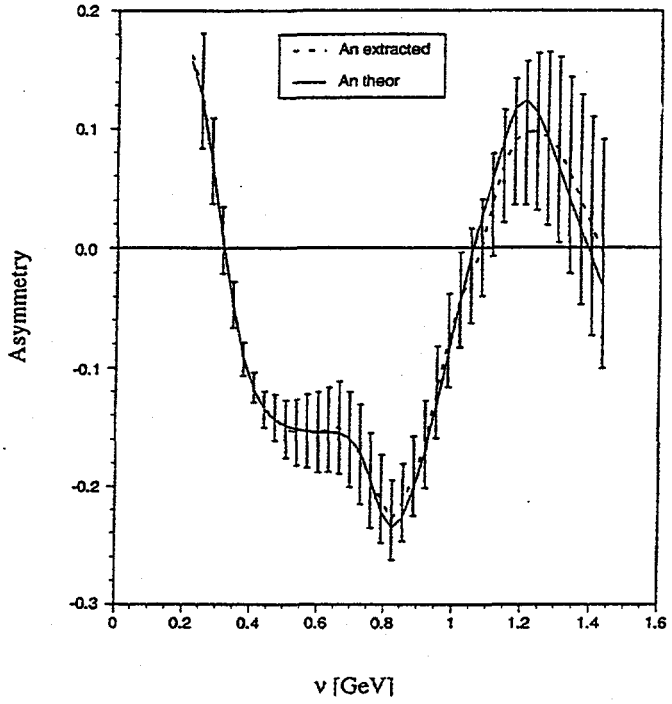

Figure 8: Expected statistical error for the asymmetry $A/D(ex) \cdot \sigma_T$. The deviations of the expected data points from the line indicate the systematic uncertainty due to the assumption $A_2^n = 0$.

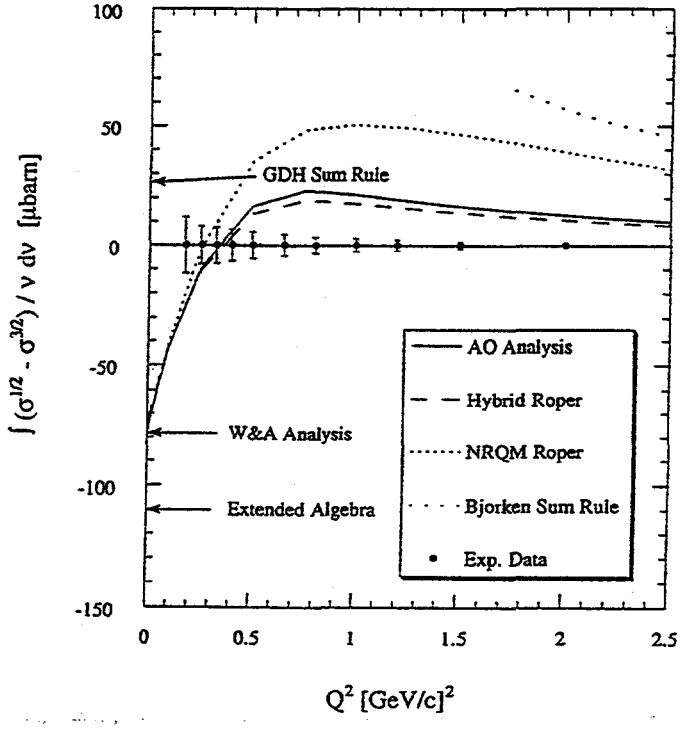

Figure 9: Expected errors for the proton - neutron difference $\Delta I_{pn}(Q^2)$.

5. Pion Electroproduction with Polarized Beam and Target.

A large number of resonances, attributed to the excitation of the nucleon have been observed in hadron scattering, the $\Delta(1232)$ being the most prominent one. Electroexcitation of resonances on the free nucleon yields information on the $\gamma_v NN^*$ vertex as a function of Q^2. The transition into a specific excited state is described by three amplitudes $A_{1/2}(Q^2)$, $A_{3/2}(Q^2)$, $S_{1/2}(Q^2)$, where A and S refer to transverse and scalar coupling, respectively, and the subscripts refer to the total helicity of the $\gamma_v N$ system (frequently, the electromagnetic multipoles $E_{l\pm}$, $M_{l\pm}$, $S_{l\pm}$ are used instead). Inclusive measurement of $\gamma N \rightarrow X$, or $eN \rightarrow eX$ reveal a few broad bumps, clearly indicating the excitation of resonances in the mass region below 2 GeV. Their broad widths and close spacing makes it impossible to separate them in inclusive production reactions. By explicit measurement of the decay products such as $\pi N, \eta N, \rho N, \pi\Delta$, and others, it is possible to identify them according to their spin and isospin assignments.

The physics issues one hopes to study are manifold, and address fundamental questions about the interaction of quarks and gluons in confined systems. Measurement of the Q^2 evolution of the transition formfactors provides information about the wave function of the excited state. The helicity asymmetry

$$A_{1/2,3/2} = \frac{A_{1/2}^2 - A_{3/2}^2}{A_{1/2}^2 + A_{3/2}^2} \tag{14}$$

for the transition into some excited states, like the $D_{13}(1520)$, or $F_{15}(1688)$, was found to be sensitive to the potential that confines the valence quarks inside the nucleon.[53] At high momentum transfer one may observe the transition from the non-perturbative to the perturbative regime, where power law rules for the helicity amplitudes are predicted to apply[7] such that:

$$A_{1/2} = \frac{c_1}{Q^3} \quad , \quad A_{3/2} = \frac{c_2}{Q^5} \quad , \quad Q^2 \rightarrow \infty \tag{15}$$

if logarithmic terms are neglected. Whether this regime can be reached at the available energies (e.g. 6 GeV at CEBAF) is an open question. Nonetheless, it will be interesting to push studies of the helicity structure of nucleon resonance excitations to the highest possible Q^2.

A complete program to study nucleon resonance transitions,e.g. in $\gamma_v N \rightarrow \pi N$, involves measurement of 6 (4 in photoproduction) complex, parity conserving amplitudes.

$$H_i := < \lambda_\pi; \lambda_N | T | \lambda_{\gamma_v}; \lambda_p > = < 0; \pm\frac{1}{2} | T | \pm 1, 0; \pm\frac{1}{2} >$$

which makes it necessary to measure at least 11 independent observables, not counting additional measurements to resolve quadratic ambiguities. Experiments involving unpolarized particles only, allow measurement of only 4 response functions σ_T, σ_L, σ_{TT}, σ_{LT}:

$$\frac{d\sigma}{d\Omega} = \sigma_T + \epsilon\sigma_L + \epsilon\sigma_{TT} cos2\phi + \sqrt{\epsilon(1+\epsilon)/2}\sigma_{LT} cos\phi \tag{16}$$

Measurement of polarization observables yield information on many response functions (table). I want to illustrate the significance of polarization measurements for this program with two examples, the $\gamma_v p\Delta^+(1232)$ and the $\gamma_v p P_{11}^+(1440)$ transitions.

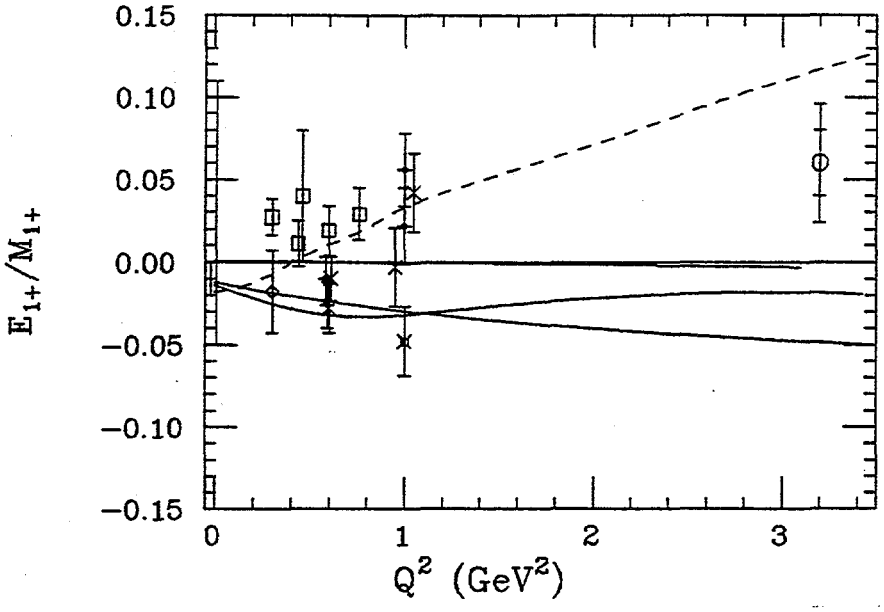

Figure 10: E_{1+}/M_{1+} ratio for the $\gamma N\Delta$ transition. The lines represent various quark model predictions. The highest Q^2 point is from a recent multipole analysis.[46]

5.1. The Transition $\gamma_v p \to \Delta^+(1232) \to N\pi$.

In SU(6) symmetric quark models this transition is explained by a simple quark spin-flip in the $L_{3Q} = 0$ ground state, corresponding to a magnetic dipole transition M_{1+}. The electric and scalar quadrupole transitions are predicted to be $E_{1+} = S_{1+} = 0$. In more elaborate QCD based models which include color magnetic interaction arising from the one-gluon exchange at small distances, the $\Delta(1232)$ acquires an $L_{3Q} = 2$ component, leading to small electric and scalar quadrupole contributions (e.g. $|E_{1+}/M_{1+}| \simeq 0.01$ at $Q^2 = 0$). The ratio $|E_{1+}/M_{1+}|$ is predicted to be weakly dependent on Q^2. At very high Q^2, helicity conservation predicts[31] $E_{1+}/M_{1+} \to 1$, and $S_{1+}/M_{1+} \to 0$. Precise measurements of these contributions from $Q^2 = 0$ to large Q^2 are obviously important for the development of realistic models of the nucleon structure. Present data on E_{1+} are shown in Figure 10, together with model predictions. The quality of the data is clearly not sufficient to discriminate against any of the models. Experiments at MIT-Bates[43] and CEBAF[42,44] are in preparation to measure the electric and scalar quadrupole transition over a large Q^2 range, using polarized electron beams and/or recoil polarimeters. In these experiments information about the terms

$$M_{1+}\ ,\ Re(E_{1+}M_{1+}^*)\ ,\ Re(S_{1+}M_{1+}^*)\ ,\ Im(E_{1+}M_{1+}^*)\ ,\ Im(S_{1+}M_{1+}^*)$$

is obtained. The imaginary parts of the bilinear terms can only be accessed using polarization degrees of freedom. They are particular sensitive to phase relations between the multipoles. If the multipoles were strictly in phase, these terms would vanish identically. Experiment E-91-011[43] at CEBAF will measure recoil polarization observables in the $\Delta(1232)$ region, which are especially sensitive to the small S_{1+} quadrupole transition (Figure 12).

5.2. The Transition $\gamma_v p \rightarrow P_{11}^{+}(1440) \rightarrow N\pi$.

The Roper resonance P_{11} has a modestly strong photocoupling at $Q^2 = 0$, but in electron scattering there is little evidence for its excitation both, in the inclusive cross section and in exclusive single pion production at $Q^2 < 1GeV^2$. Non-relativistic as well as relativized[32] quark models predict the $A_{1/2}(P_{11})$ amplitude to grow with Q^2 relative to the $\Delta(1232)$. In non-relativistic models $A_{1/2}(P_{11})/A_{1/2}(\Delta) \sim \vec{Q}^2$, so that the P_{11} would dominate at high Q^2.

The predicted dominance of the P_{11} at high Q^2 will be a crucial test of the quark model classification as a N=2 radially excited state. Measurements with polarized proton targets,[45] or proton recoil polarization measurements[47] can provide a strong signature for the excitation of this resonance in electron scattering experiments. CEBAF experiment 93-036[48] will measure polarization observables in single pion production. This experiment, in conjunction with the unpolarized experiments of the N^* program[6] will allow isolation of the helicity amplitudes $A_{1/2}$, $A_{3/2}$ for individual resonances throughout the entire resonance region. The Q^2 dependence of $A_{1/2}$, $A_{3/2}$ is sensitive to the QCD structure of resonant states. The Q^2 evolution of the transverse and longitudinal photocoupling amplitudes $A_{1/2}(Q^2)$ and $S_{1/2}(Q^2)$ are very sensitive to the internal quark-gluon structure of the $P_{11}(1440)$.[27] As an illustrative example, Figure 12 shows first moments of the polarized target asymmetries for various models of the structure of the $P_{11}(1440)$.

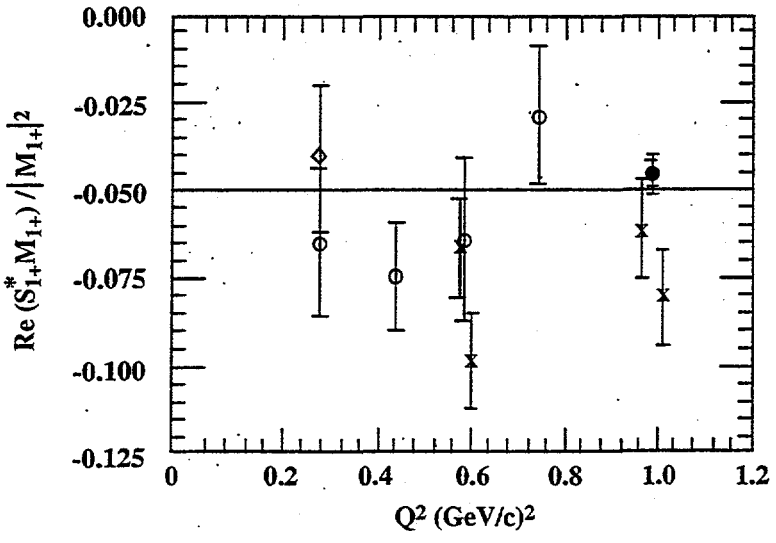

Figure 11: Projected data for CEBAF experiment 91-0[44] in $p(\vec{e}, e'\vec{p})\pi^0$ (full circle) compared to previous results.

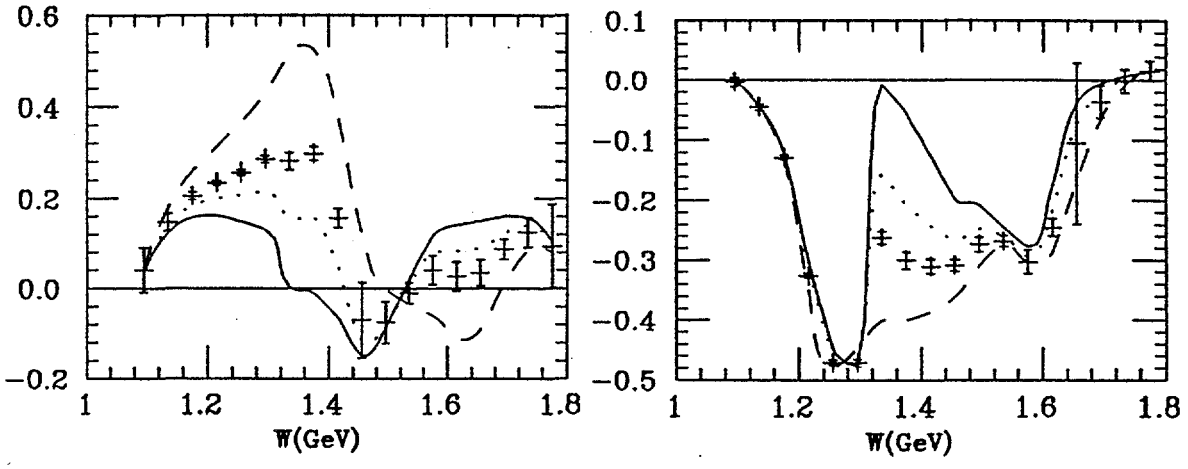

Figure 12: Moments $\int A_t(\theta,\phi)P_1(\theta)\sin\phi d\Omega$ of the polarized target asymmetry for single π^0 (left)and π^+ production. The curves represent results[19] for various models of the $P_{11}(1440)$ structure. Also shown are projected errors for the experiment.

From a measurement of $A_{1/2}$, $A_{3/2}$ for separated resonant states one can determine contributions of individual states to the GDH integral. In comparison with quark model calculations, knowledge about the QCD structure of the N^* and Δ^* resonances is obtained.

5.3. Search for Missing Quark Model States

The QCD motivated extension of the non-relativistic quark-model[51] predicts many states, in particular at higher masses, which have not been observed in πN reactions. Theoretical calculations[24] indicate that the "missing" states tend to decouple from the πN channel, which would explain why they have not been seen in elastic πN scattering. Our picture of baryon structure could drastically change if these states did not exist. Several of these states are predicted to couple strongly to photons (real or virtual) and may thus be searched for in photo- or electroproduction experiments.

One of the missing states is the $N_{5/2}(1955)$ which is in the NRQM is predicted to couple to strongly to the $N\omega$ channel. Unfortunately, this channel has also a strong diffractive contribution, such that resonance strength in the differential cross section is seen only at ω production angles greater than 90° (Figure 13). The sensitivity to intermediate resonance excitation is much enhanced even at smaller angles if the spin polarization of the ω is measured. This requires detection of at least two of the decay pions which allows measurement of the decay plane in the ω rest frame given by the angles ϕ_{decay} and θ_{decay}. Figure 14 shows the sensitivity of the decay angle distribution to the ω production mechanism. Sensitivity to resonant production is present even where the differential cross section shows little sensitivity such as near and below $\theta_\omega = 90°$. The same method can be used to study the production mechanism of other

vector mesons such as the ϕ in: $ep \rightarrow ep\phi$ $(\phi \rightarrow K^+K^-)$,[55] or the Δ polarization in $ep \rightarrow e\Delta\pi$, $\Delta \rightarrow N\pi$. Obviously, experiments of this type require use of a large acceptance spectrometer such as CLAS[34] at CEBAF.

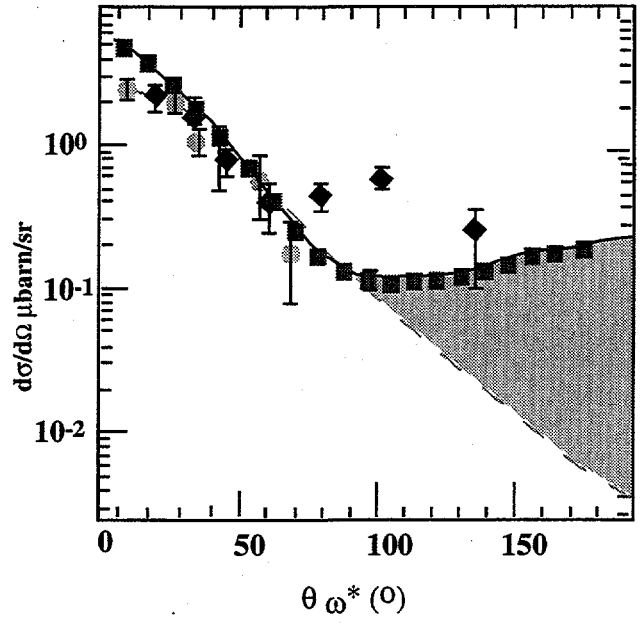

Figure 13: Differential cross section for ω electroproduction. The curves represent contribution from diffractive production and the $\gamma\pi\omega$ term (long dashes), and resonance contributions from a $N^*(1950)$ quark model state[52] (shaded area), open squares represent projected data.

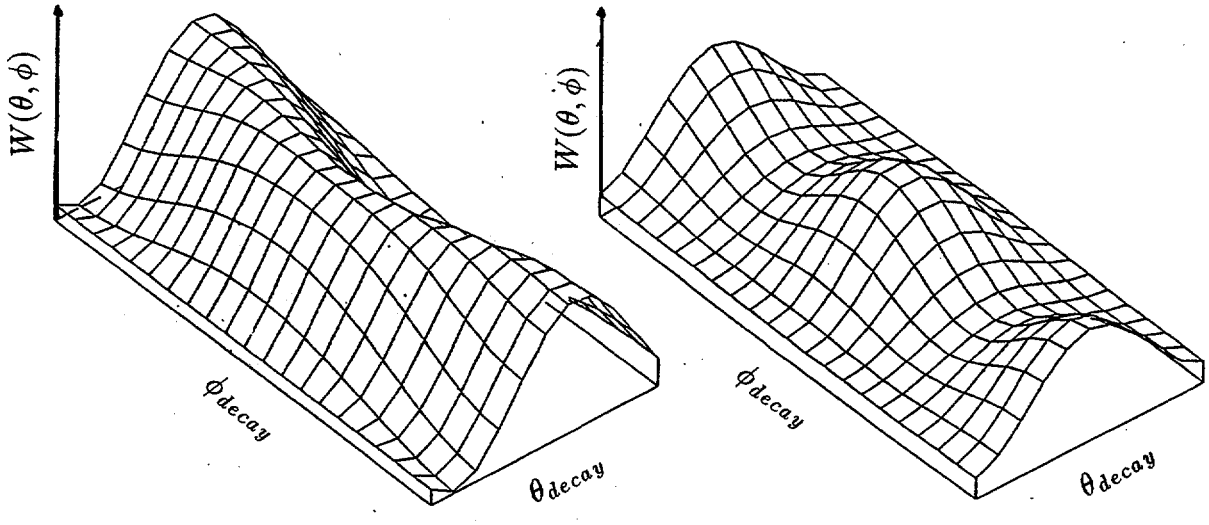

Figure 14: ω decay angular distribution in the Gottfried-Jackson frame for different ω production mechanism at $\theta_\omega = 90^o$. (diffractive and $\gamma\pi\omega$ term (left), including resonance contribtions (right).[54]

6. Summary

Measurement of polarized structure functions of the proton and neutron probe significant contributions to the spin integrals at low Q^2 and ν and are important for testing the validity of the GDH sum rule and models describing its extension to finite Q^2. Measurement of spin observables in elastic electron scattering and in meson production experiments provide detailed information about the electromagnetic formfactors of the ground states nucleon, as well as the transition formfactors into the many excited states. This information is crucial in probing the QCD structure of the nucleon.

References

1. J. Ashman et al., Phys. Lett. B206 (1988)364; Nucl. Phys.B328 (1989)1.
2. B. Adeva et al., Phys. Lett. B 302 533 (1993).; D. Adams et al., Phys. Lett. B229, 399 (1994)
3. J. Lichtenstadt, invited talk at this workshop
4. O. Rondon-Aramayo, invited talk at this workshop
5. P.L. Anthony et al., Phys. Rev. Lett. (1993).
6. CEBAF N* program; Experiments 89-037/38/39/40/42/43, 91-024, 93-06.
7. S. J. Brodsky and G. P. Lepage, Phys. Rev. D24, 2848 (1981)
8. S. Platchkov et al., Nucl.Phys. A510, 740 (1990)
9. C. Perdrisat, invited talk at this workshop.
10. D. Crabb, invited talk at this workshop.
11. F. Klein, Talk presented at the International Conference on Few Body Problems, Williamsburg, May, 1994.
12. J. Gomez and G. Petratos (spokesmen), CEBAF Experiments E-93-024; R. Madey (spokesman), E-93-038 ; W. Brooks and M. Vineyard (spokesmen), E-94-017
13. N. Dombey, Rev. Mod. Phys. 41, 236 (1969)
14. V. Burkert, Proc. Workshop on Electron and Photon Interactions at Intermediate Energies, Springer Tracts in Modern Physics 234, pg.228 (1984)
15. R. Arnold, C. Carlson, F. Gross, Phys. Rev. C23, 363 (1981)
16. H. Arenhövel, W. Leidemann, and E.L. Tomusiak, Z. Phys. A331, 123 (1988)
17. S. Gerasimov,Yad.Fiz.2, 598(1965) [Sov. J. Nucl. Phys.2 (1966)930].
18. S.D. Drell and A.C. Hearn, Phys. Rev. Lett. 16 (1966) 908.
19. V. Burkert and Zh. Li, Phys. Rev.D47, 46(1993)
20. V. Burkert and Zh. Li, in preparation.
21. M. Anselmino, B.L. Ioffe and E. Leader, Sov. J. Nucl. Phys. 49 (1989) 136.
22. V. Burkert and B.L. Ioffe, Phys. Lett.B296 (1992)223
23. V. Burkert and B.L. Ioffe, J. Exp. Theor. Phys. 78, 619(1994) (Zh. Eksp. Teor. Fiz. 105, 1153 (1994))
24. I.G. Aznauryan, Yad. Fiz. 6, 124(1966) [Sov. J. Nucl. Phys. 6, 91(1967)];
25. Z.P. Li, Phys.Rev.D47, 1854(1993)
26. D. Drechsel and M. Giannini, Preprint MKPH-T-93-12 (1993); D. Drechsel, Preprint MKPH-T-94-18 (1994)

27. Z.P. Li, V. Burkert, Zh. Li, Phys. Rev. D46, 70(1992).
28. I. Karliner, Phys.Rev. D7, 2717 (1973)
29. R. Workman and R. Arndt, Phys. Rev. D45, 1789(1992)
30. L.N. Chang, Y.G. Liang and R. Workman, Phys. Lett. B329, 514 (1994)
31. C.E. Carlson and J.L. Poor, Phys. Rev. D38, 2758 (1988)
32. S. Capstick, Phys. Rev. D46, 2864(1992)
33. V. Burkert, D. Crabb, R. Minehart (spokesmen),CEBAF Experiment E-91-023
34. V. Burkert and B. Mecking, in: 'Modern Topics in Electron Scattering', in: World Scientific, 1991; eds. B. Frois and I. Sick.
35. S. Kuhn (spokesman), CEBAF Proposal 93-009.
36. G. Baum et al., Phys.Rev. Lett. 45, 2000 (1980).
37. J. Soffer and O. Teryaev, Phys. Rev. Lett. 70, 3373 (1993)
38. V. Bernard et al., Phys. Rev. D48, 3062 (1993)
39. S. Kuhn, V. Burkert, Zh. Li, Proceedings PANIC 93, Perugia, Italy, June 1993.
40. MAMI Proposal A2/2 - 93 (1993)
41. D. Sober (spokesman), CEBAF Experiment E-91-015
42. V. Burkert and R. Minehart (spokesmen), CEBAF experiments 89-037/42
43. R. Lourie and V. Burkert (spokesmen), Bates experiment E-89-03
44. R. Lourie and S. Frullani (spokesmen), CEBAF Experiment E-91-011
45. V. Burkert, Int. J. Mod. Phys. E1, 421 (1992)
46. V. Burkert and L. Elouadrhiri, CEBAF Preprint PR-95-0xx (1995)
47. R. Lourie, Z. Phys. C50, 345 (1991)
48. H. Weller, R. Chasteler and R. Minehart (spokesmen), CEBAF proposal 93-036.
49. J.D. Björken, Phys.Rev.148, 1467(1966).
50. J. Ellis and R.L. Jaffe, Phys. Rev. D9, 1444 (1974)
51. N. Isgur and G. Karl, Phys. Lett. 72B, 109 (1977); Phys. Rev. D23, 817 (1981)
52. I. Koniuk and N. Isgur, Phys. Rev. D21, 1868 (1980)
53. W. Warns, et al., Z. Phys. C45, 613 (1990); Z. Phys. C45, 627 (1990)
54. CEBAF experiment E-91-024 (H. Funsten, V. Burkert, M. Manley, B. Mecking, spokesmen)
55. CEBAF experiment E-93-022, (H. Funsten, E. Smith, P. Rubin, spokesmen)

SOLID POLARIZED TARGETS

D.G. Crabb
Physics Department, University of Virginia
Charlottesville, VA 22901, USA

ABSTRACT

Polarized targets using the method of dynamic nuclear polarization (DNP) are in use in many laboratories. The method of DNP is reviewed briefly and the technical developments presented at recent meetings are discussed. The operation of target systems at SLAC and CERN are presented as examples. The emergence of frozen HD as a possible target is discussed.

1. Introduction

During the course of this talk I will discuss the status of dynamically polarized solid state targets and progress in various subsystems. I will refer in some detail to the targets used in experiment E143 at SLAC[1] and in experiment NA47 (SMC) at CERN.[2] They each, in different ways, represent the state of the art.

Recently, there have been two meetings which covered polarized targets and subsystems in great detail.[3,4] I am indebted to many of the people who made presentations at these meetings for use of their data. In some cases the figures in this report have been taken from transparencies.

2. Polarized Target Systems

Figure 1 shows a schematic of a generic polarized target showing the necessary subsystems.

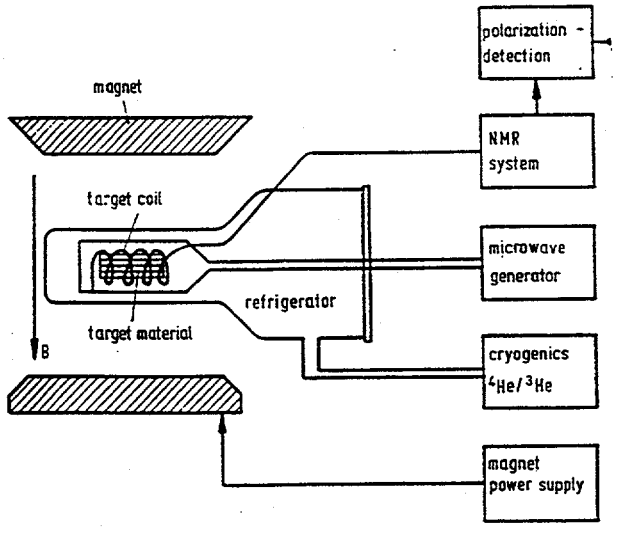

Fig. 1 Subsystems of a Polarized Target

A suitable material, containing a high content of polarizeable nucleons and lightly doped with a paramagnetic compound to provide unpaired, "free" electrons, is placed

in a high magnetic field (2T-6T) and cooled to low temperature ($\leq$ 1K). The material is irradiated with microwaves ($\sim$28 GHz/T, ie 140 GHz at 5T) to allow DNP to take place. The polarization actually achieved is measured with NMR.

To better understand the process I will discuss each step.

2.1. "Recipe" for DNP Material

a) Take 10 gm (say) of hydrogenous material (eg butanol, propanedial) and add $\sim$ 100 mgm of paramagnetic dopant (eg CrV in its synthesized form of EHBA). Mix thoroughly to form a dilute spin system and then freeze in liquid nitrogen in the form of 2mm beads.

or

b) take 10 gms of ammonia and freeze in LN_2, again in the form of 2mm beads or granules. Irradiate the ammonia with electrons (usually) to the level of $\sim 10^9$ rads. This must be done under liquid argon as liquid nitrogen can explode under these conditions of intense radiation.

The prepared material is then cooled to $\leq$ 1K and subjected to a magnetic field in the range of 2T-6T. In the case of discrete energy levels (the solid state effect) there will be Zeeman and Hyperfine splitting as shown in Fig. 2 for the spin 1/2 proton.

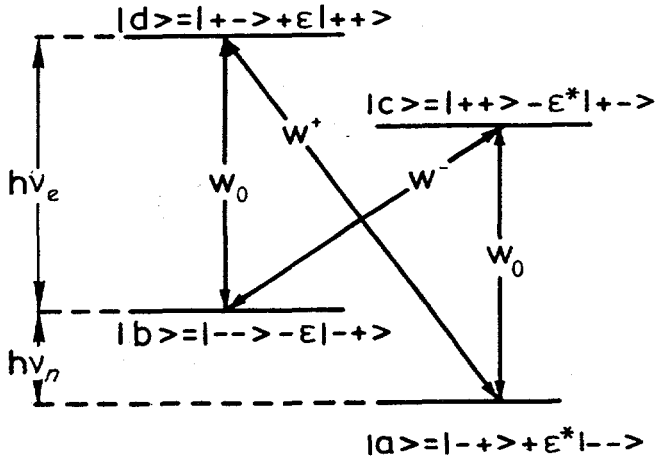

Under conditions of thermal equilibrium (TE) the polarizations (P_{TE}) of the electron and proton can be obtained from the population of the "up" and "down" states $N^{\uparrow}$ and $N^{\downarrow}$

$$P_{TE} \rightarrow \frac{N^{\uparrow} - N^{\downarrow}}{N^{\uparrow} + N^{\downarrow}} \rightarrow \tanh\left[\frac{\mu B}{kT_L}\right] \tag{1}$$

where μ is the magnetic moment, k the Boltzmann constant, B the magnetic field and T_L the lattice or bulk material temperature. For the case of B=2.5T and $T_L = 0.5$K, $P_e > 99\%$ and $P_p \approx 0.5\%$. In DNP, the polarization of the electron is "transferred"

to the proton by driving the forbidden transition b to c (a to d) with microwaves of frequency $\nu_e - \nu_p$ ($\nu_e + \nu_p$) to enhance $P_p^{\uparrow}$ ($P_p^{\downarrow}$). For these conditions, $\nu_e \sim 70GHz$ and $\nu_p = 106.5MHz$. The reason that this works is that the spin lattice relaxation times (the time for the spin to flip back to the lower energy state) for the electron and proton are very different. The electron relaxation time is, $T_1 \sim$ 1ms while the proton relaxation time is $T_1 \sim$ 10 - 100s of minutes. This means that the small number of electrons are continually being flipped while a proton once flipped stays in that state for a long time - thus the particular state is enhanced.

Another element in the process is "spin diffusion", a means by which protons far from the flipped electron are flipped into the polarization state.

The preceeding discussion is only valid for materials in which discrete energy levels can be considered. However, the polarization process in most materials used today, such as alcohols, can be understood in the related concept of thermal mixing. In this case there are energy bands rather than discrete levels. A nuclear ordering takes place, leading to an alignment of spin, to which can be assigned a spin temperature, T_S. The enhanced polarization P_{enh} can then be obtained by replacing T_L, in E_{qn} (1) by T_S so that

$$P_{enh} = \exp\left[\frac{\mu B}{kT_S}\right] \tag{2}$$

The idea of equal spin temperature (EST) says that all spin species in a material, eg residual protons in deuterated material, are at the same spin temperature and therefore the polarizations of the different species are proportional to the magnetic moment of each type. Many materials obey the EST hypothesis.

The principles of DNP have only been touched on here, but complete descriptions can be found in the book by Abragram[5] and the articles by Borghini[6] and De Boer.[7]

3. Polarized Target Subsystems

3.1. Magnets and Refrigerators

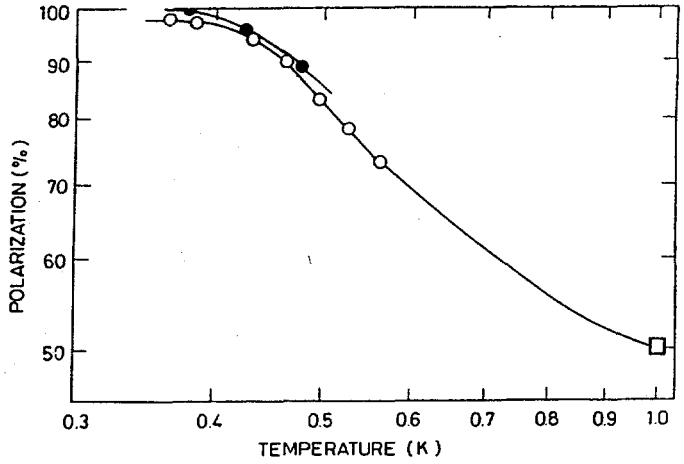

Fig. 3
Polarization in propanediol as a function of temperature

The operation of a polarized target is linked to the value of $\frac{B}{T_L}\left(\frac{Tesla}{K}\right)$, as can be seen in Fig. 3, where the polarization achieved with propanediol in a 2.5 T magnetic field is shown as a function of temperature.[8] The early targets used iron magnets with fields of $\sim$ 2T and operated at temperatures of 1 - 1.5K with ^4He evaporation refrigerators so that $\frac{B}{T_L} \sim 2$. The development of ^3He evaporation refrigerators (T $\sim$ 0.5K) together with high field superconducting magnets (fields up to $\sim$ 6T) meant that $\frac{B}{T_L} \sim$ 50 - 100. However, for various practical reasons, DNP works best when $\frac{B}{T_L}$ $\sim$ 5-10. The related idea of "frozen spin" has $\frac{B}{T} \sim 10$ for most experiments, where $B \sim$ 0.5T but T $\sim$ 0.05K.

In a ^4He evaporation refrigerator liquid ^4He is fed into a separator pot where cold vapor is pumped away by a small pump and cools radiation shields and baffles. Liquid flows through a sintered copper phase separator into a heat exchanger and then is metered into the target chamber via a needle valve assembly. The liquid in the target chamber is pumped on by large Roots pumps to reduce the temperature to $\sim$ 1K. With sufficiently large pumps, cooling powers of 2W are obtainable. The thermal properties of the super fluid ^4He allow the target to be operated with high heat input from particle beams. However, for the best polarization results, this type of refrigerator should be used with a high field magnet ($\sim$5T). Early experiments at SLAC[9] used such a system.

In a ^3He evaporation refrigerator, a ^4He refrigerator is used to cool the incoming ^3He, which then proceeds through a heat exchanger similar to that described above for ^4He. Pumping on the liquid ^3He achieves a temperature of $\sim$ 0.5K with a typical cooling power of 150-200 mW. Although much used 10 to 15 years ago with 2.5T magnets, this type has now been mostly superceded by dilution refrigerators.

The concept of a dilution refrigerator (DR) is shown in Fig. 4. The DR uses a mixture of ^3He and ^4He. Referring to Fig. 4, liquid ^3He is brought into the mixing chamber through various heat exchangers so that it is cold enough ($\leq$ 0.8K) to separate

out[10] from the mixture and float on top of the liquid ^4He. The ^3He is heated and

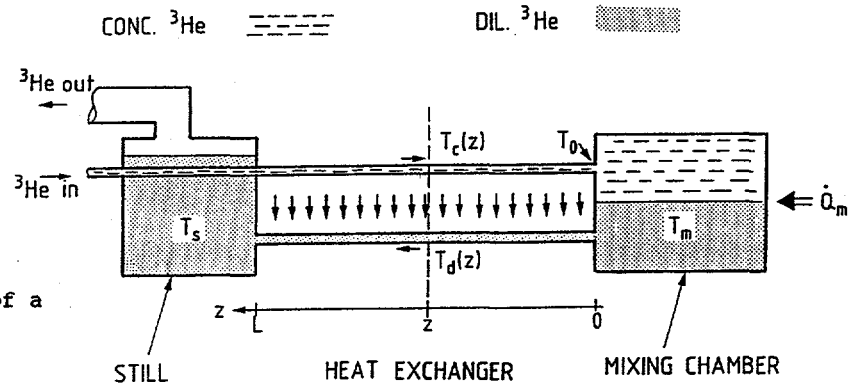

Fig. 4
Principle of operation of a dilution refrigerator.

pumped away at the still and is thus pulled from the mixing chamber through the liquid ^4He to the still. Cooling takes place at the phase boundary in the mixing chamber and temperatures of < 50mk can be achieved in most polarized target DR's. The cooling power depends on the circulation rate of ^3He and is typically $\sim$100 mW but can reach 2 or 3 W in a large enough system.[2]

With the availability of very low temperatures the frozen spin mode of operation for targets can be considered. Fig. 5 shows the proton polarization relaxation time (T_{1P}) for propanediol, at three different temperatures, as a function of magnetic field.[8] From this graph it is clear that T_{1P} is a strong function of $\frac{B}{T}$. Once the target is polarized, and at a low enough temperature, the magnetic field can be reduced to a low value and still retain a satisfactory T_{1P}. A low field configuration generally means a much larger solid angle for detecting scattered particles.

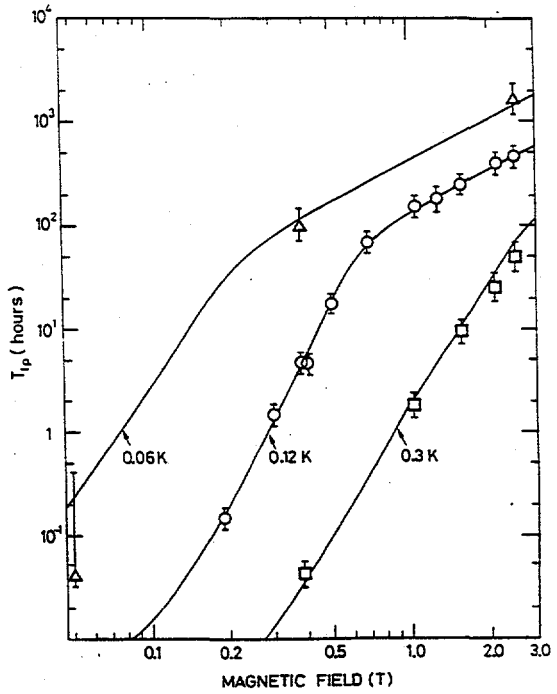

Fig. 5
Proton polarization relaxation time ($T_{1\rho}$) as a function of magnetic field, at three temperatures.

Groups from Saclay, Bonn, Triumf and PSI presented details of the operation of frozen spin targets. Various techniques for moving from polarizing to frozen mode were shown and discussed. The architecture of spectrometers now require that the DR be moved over relatively long distances, sometimes through the iron of a spectrometer magnet, to go from the high field polarizing mode, to the low field holding position. The target must always see a field of a few kG and a number of schemes are in operation. For instance, Bonn reported on a holding magnet wound inside the target DR. This is very thin (500 μm) to allow particles to escape from the target volume, but has achieved a maximum field of 0.4T and, consequently, acceptable relaxation times.

3.2. Microwaves

For DNP, the microwave frequency needed is about 28 $\frac{GHz}{T}$, ie 140 GHz at 5T. Tubes which have been or are in use include carcinotrons, klystrons, EIO's, and IMPATT diodes. These are all narrow band devices with tuning possible only over a few GHz. They are also expensive devices so the matching of magnetic field and tube frequency is very important.

Another factor is the power necessary for optimum polarization performance. Typically, this is 1-2 mW/gm at 2.5T/0.5K and 40mW/gm at 5T/1K. For these tubes, as the central frequency increases, the power available across the tuning band decreases and the matching waveguide power losses in the matching waveguide components increase. For 140 GHz microwaves we have been using EIO's from Varian Canada, which produce 10-20W, to transmit sufficient power to the target.

Another factor is that the power supply for these tubes needs to have the capability of providing frequency modulation (fm) for the tube. An fm of $\sim \pm$ 25MHz at a rate of 500Hz is necessary and usually is obtained by varying the tube cathode voltage through several hundred volts. As will be discussed later, the fm can have a significant effect on the polarization.

3.3. NMR

The calibration and measurement of the polarization is done with a series resonant LCR circuit, where the L is a coil near the polarized material that senses changes in magnetization. The coil is connected to a Q-meter by a cable of length $n\lambda_o/2$, which, at the resonant frequency $\omega_o = \frac{1}{\sqrt{LC}}$, does not contribute to the impedance of the circuit. This means that the circuit can be tuned to resonance by a capacitor C, external to the cryostat. ω_o is defined to be the NMR frequency at the external magnetic field being used.

In this arrangement the circuit is tuned to ω_0 by obtaining a symmetric Q-curve from modulating the frequency around ω_0, and by adjusting C to compensate for the fixed L. The polarized nuclei have a magnetic susceptibility which modifies the Q of the circuit (hence Q-meter). The change in Q is measured by a change in the voltage

across the coil when the tuned circuit is modulated around ω_0. Many groups now use the Liverpool style Q-meter[11] for signal detection. A typical set up[12] is shown in Fig.6.

In practice, the Q curve is tuned when slightly off resonance by shifting the magnetic field to obtain a baseline. After moving the field back to resonance and making a measurement, the baseline is substracted from the on-resonance measurement to obtain the NMR signal. The signal is then integrated to obtain the polarization. The integral is normalized by measuring the TE signal area.

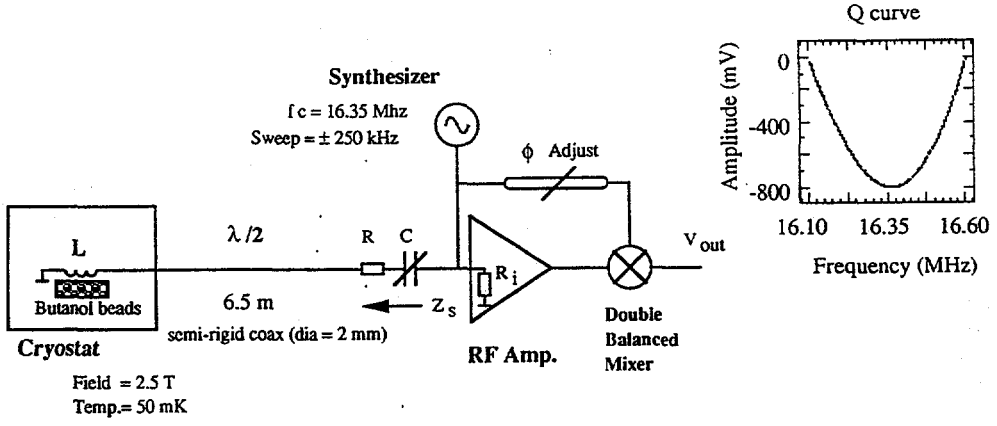

Fig. 6 Q-meter circuit

A typical procedure is to allow the sample reach TE at a temperature of $\sim$ 1.5K (5T), or $\sim$ 1K (2.5T). Then the TE polarization can be calculated from equation (1) so that

for protons

$$P_{TE} = \tanh\left[\frac{\mu B}{kT_L}\right] \sim 0.03\% \tag{3}$$

for deuterons

$$P_{TE} = \frac{4\tanh\left[\frac{\mu B}{2kT_L}\right]}{3+\tanh^2\left[\frac{\mu B}{2kT_L}\right]} \sim .07\% \tag{4}$$

The area A_{TE} of the NMR TE signal is measured and scaled against that of the enhanced signal area A_{enh} to give the enhanced polarization $P_{enh} = \left[\frac{A_{enh}}{A_{TE}}\, Gain\right] P_{TE}$. The error on the polarization is dominated by the error in measuring A_{TE}. Moreover

the proton TE signal is generally much easier to detect than that of the deuteron. Measurement errors of $\frac{\Delta p^p}{p^p} \approx 2.5\%$ have been achieved and are dominated by systematic effects over the lifetime of a target. For the deuteron, $\frac{\Delta p_d}{p^d} \sim 4\%$ and is dominated by statistical effects.

Typical deuteron TE signals from E143[1] and SMC[2] targets are shown in Fig. 7

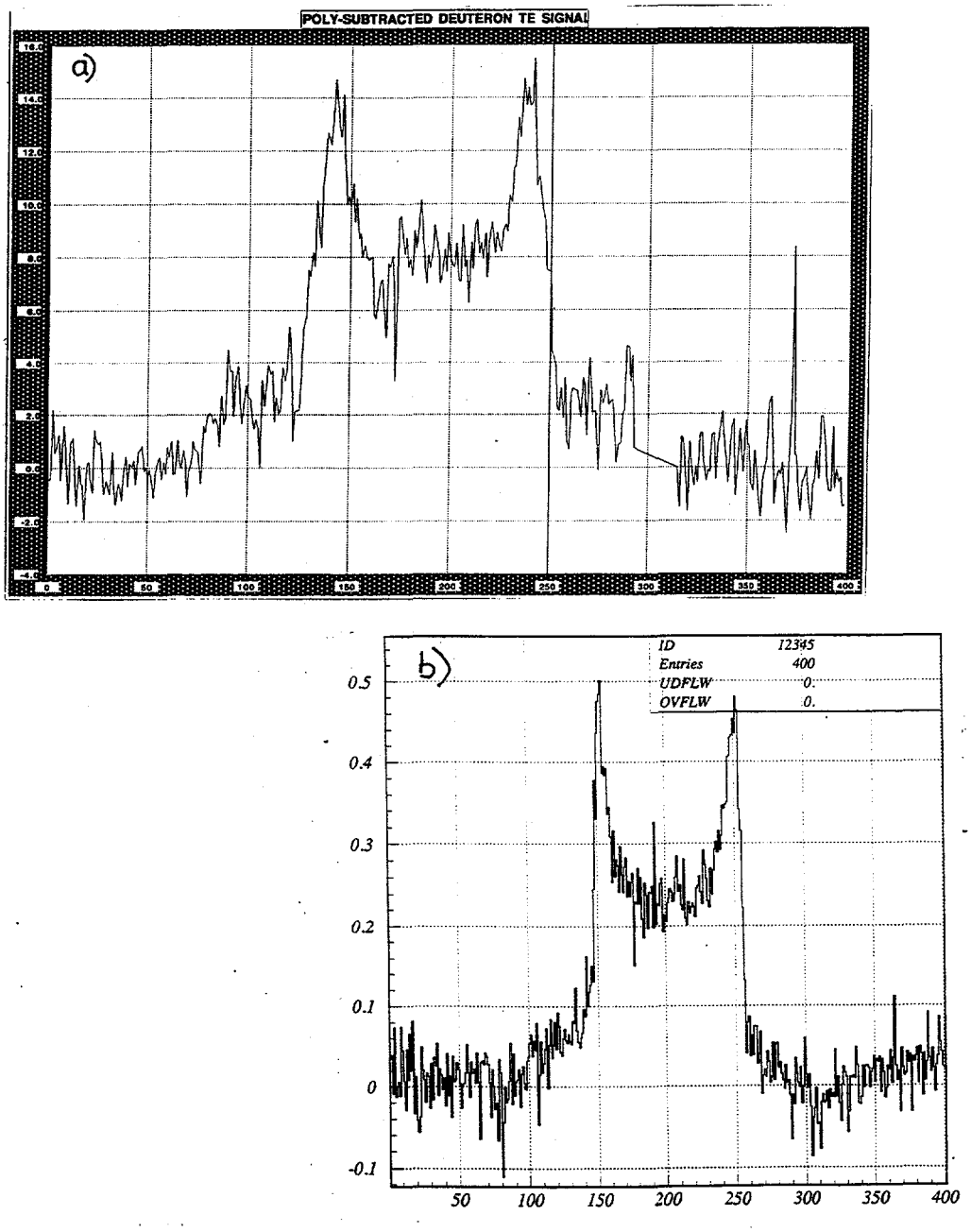

Fig. 7
Deuteron TE signals from a) ammonia used in E143 and b) butanol used in SMC.

3.4. Materials

Some properties required of polarized target materials are:

1. Large proton (deuteron) content (10-20% by weight)
2. High degree of polarization
3. Fast build up time
4. Degree of doping and type of dopant

For some experiments

5. Resistance to radiation damage
6. Presence or not of other polarizeable nuclei

Examples are:

a) Radiation doped:
Ammonia (p,d), LiH, LiD for high radiation

b) Chemically doped:
p and d forms of butanol, pentanol propanediol, ethanediol doped with synthesized CrV (EHBA)

3.5. Chemically Doped Materials

It was reported from Saclay that pentanol-2, doped with EHBA - CrV, polarized to +84% and -87% after one hour. The advantage over the more commonly used pentanol-1 is that it stays amorphous, independent of cooling rate, so that devitrification should not be a concern. With pentanol-2 in a DR, operating in frozen spin mode (B=0.33T, T=42mk) and with a beam of 10^8 protons/burst, relaxation time of > 20 days were obtained.

From Dubna and PSI[3] came results on polarizing various powdered materials with the free-radical TEMPO, where the target preparation is at room temperature rather than at cryogenic temperatures. Of particular interest was a polarization of $\sim$60% obtained with polyethylene (CH_2) in a DR. CH_2, which has about the same dilution factor as the alcohols in use, with room temperature preparation could develop as a convenient alternative material. At the moment, the targets are limited in size ($\sim$ 100 μmpowders) due to the doping procedure of "drifting" the TEMPO.

3.6. Radiation Doped Materials

Both Saclay[4] and Bonn[3] have continued studies of LiH and LiD compounds. It has been established that polarization takes place via paramagnetic F-centers and that the pre-irradiation temperature is very important, with 180K - 195K giving the best

results. The pre-irradiation dose is also an important parameter as shown in Fig. 8 from the work at SACLAY. Here the full dose (FD) = 3 x $10^{17}e^{-}/cm^{2}$ and deuteron polarizations of > 40% were achieved after several hours in a DR at 300mK. Deuteron polarization of 70% were reached after 30 hours at 5.5 T and 1.85K.

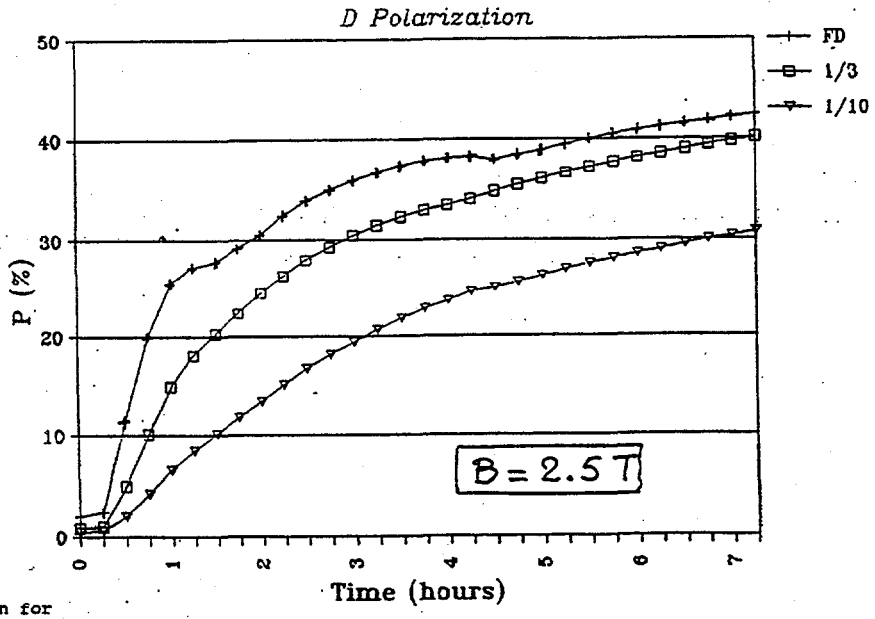

Fig. 8
Time of deuteron polarization for three samples of ^{6}LiD.

Bonn investigated the effects of additional low temperature irradiation on polarization after a pre-irridiation dose of 2 x $10^{17}e^{-}/cm^{2}$. After a dose of $\sim 10^{15}e^{-}/cm^{2}$ at low temperature, the build-up time decreased by a factor of 6 and, for the best conditions, $P^{d} > 50\%$ was obtained. Table I shows a compilation of results.

Table 1. Polarization Results for ^{6}LiD and ^{6}LiH Preirradiation Dose $2 \cdot 10^{17}$ e/cm^{2} at 180 K

	Temperature	Magn. Field	Max. Polarization	Build Up Time
^{6}LiD:	1.0 K	2.5 T	12.5%	50/23min[iii]
	1.0 K	5.0 T	22%	4.2/2.8 h[iv]
	200 mK	2.5 T	>30%	1.6 H[i]
	200 mK	5.0 T	>60%[ii]	4.4 H
^{6}LiH:	1.3 K	2.5 T	16%	20 min
	200 mK	2.5 T	>40%[i]	1.4 h

(i) reached after additional 10^{15} e/cm^{2} low temperature irradiation
(ii) preirradiation dose $8 \cdot 10^{17}$ e/cm^{2} at 180K
(iii) After 5 min at room temperature
(iv) cryostat in single shot mode, full microwave power

3.7. Adiabatic Fast Passage

Polarization reversal by adiabatic fast passage (AFP) has been studied by P. Hautle of PSI. It was first shown to work in deuterated butanol, where a greater than 90% efficient reversal was seen. The procedure was not expected to work very well with hydrogenous materials but, as can be seen from Table II, it works very well for ^{7}LiH, giving a 90% flip efficiency. This means that the polarization can be reversed in a few seconds, with only a 10% relative loss, rather than taking hours by using DNP.

Table 2. Compilation of results for AFP

Nuclei	Substance Dopant	param. centers conc. Spins/g	dP^{max}
^{1}H	1 butanol	2.0×10^{19}	-0.77
	EHBA-Cr(V)		(-0.69)
^{7}Li	^{7}LiH	low	-0.90
^{1}H	(irradiated)	$< 1.0 \times 10^{19}$	-0.90
^{19}F	8-fluoro-1-pentanol	1.0×10^{20}	-0.37
^{1}H	TEMPO		-0.40
^{2}H	1-butanol-d_{10}	2.36×10^{19}	-0.92
	EHBA-Cr(V)-d_{22}	6.35×10^{19}	-0.90
^{1}H	Polyethylen	2.0×10^{19}	-0.75
	TEMPO		
^{3}He	solid/liquid	no	> -0.70
^{19}F	PTFE (DLX 6000)	no	>-0.70

4. VIRGINIA/BASEL/SLAC TARGET

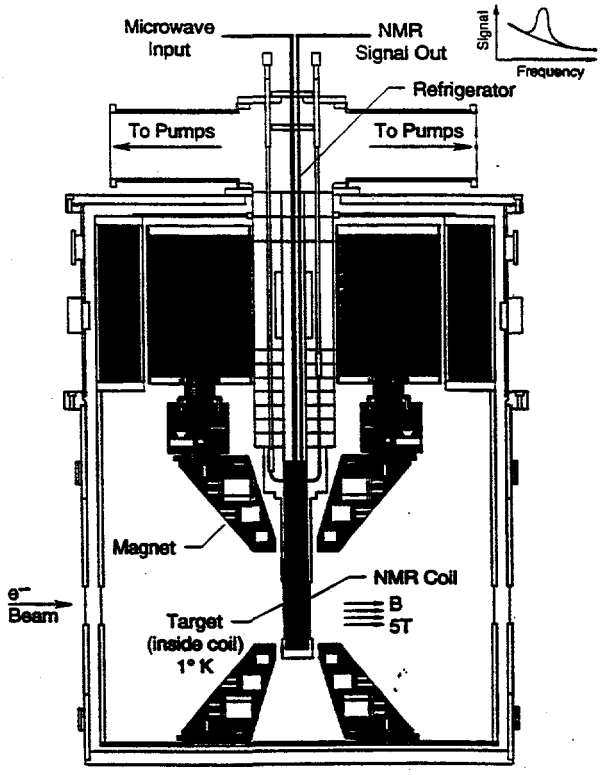

Fig. 9
Schematic of the Virginia/Basel/SLAC Polarized Target.

This target was used in the recent E143 experiment at SLAC[1] and is an example of a target which has to be operated with high beam intensity. It is shown in Fig. 9 and is a vertical ^4He evaporation refrigerator contained in an 5T superconducting magnet. An insert, which slid along the central bore of the refrigerator, carries the targets $^{15}ND_3$,$^{15}NH_3$, empty and carbon. The insert could be moved up and down and thus position any target in the beam. Fig. 10 shows the microwave layout and target NMR details.

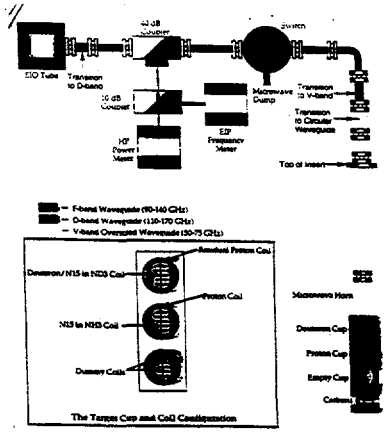

Fig. 10
Microwave and NMR schematic layout.

The performance is summarized in the following graphs. The same results were found with ^{14}N or ^{15}N ammonia. In initial tests, after irradiation under liquid Argon, it was found that the proton polarization, Fig. 11, was similar to that seen before.[13]

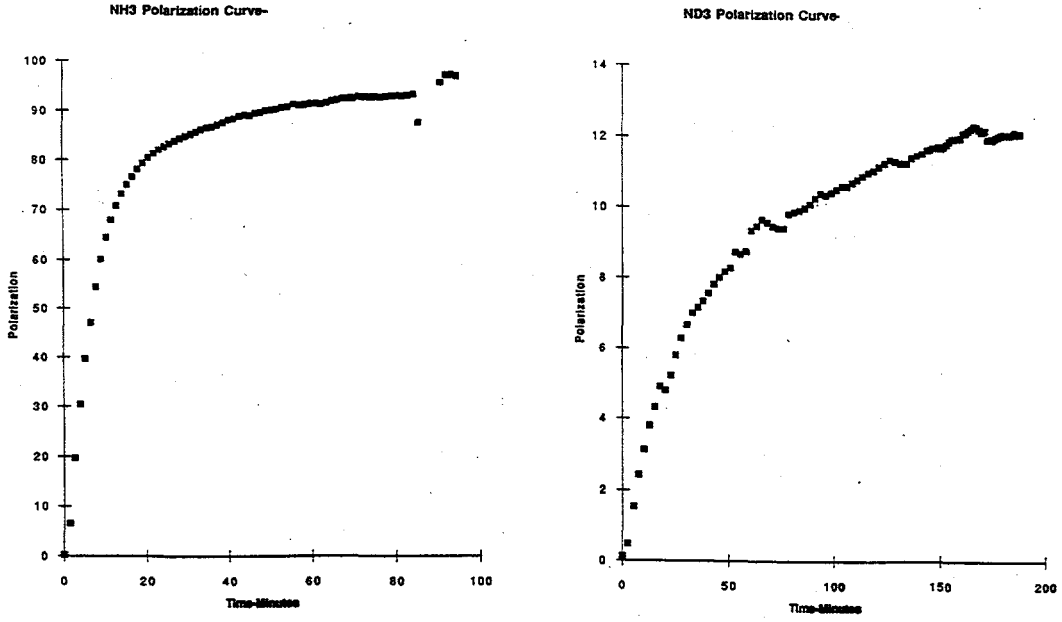

Fig. 11 Proton and deuteron polarizations vs. time in ammonia after initial irradiation.

This was the first time the deuteron had been polarized under these conditions and the performance is shown in Fig. 11., with P_d reaching 13% after about 3 hours. However, it had been noted previously[14] that ND_3 needs "in-situ" irradiation to produce the best results. Figs. 12 and 13 show results obtained with $^{15}NH_3$ and $^{15}ND_3$ in beam during the experiment. The repeated pattern is due to radiation damage followed by annealing.

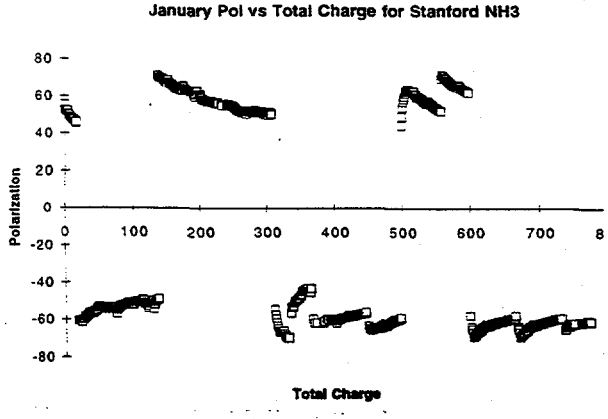

Fig. 12

Polarization history of a proton target in the E143 electron beam.

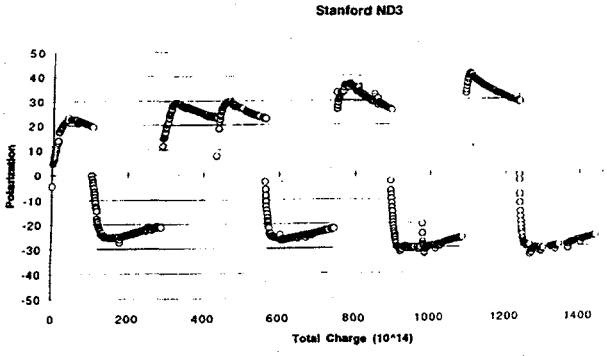

Fig. 13

Polarization history of a deuteron target in the E143 electron beam.

The proton polarization did not reach the values of > 90% seen earlier. There were two reasons for this: one is that a very high beam intensity of 5 x $10^{11} e^{-}/sec$ was going through the target; second, the NH_3 target was positioned below the ND_3 target, which absorbed enough microwaves that the NH_3 target was starved for microwave power. On the other hand, the ND_3 target improved over the course of irradiation, eventually reaching > 40% and confirming the requirement for "in-situ" irradiation. Fig. 14 shows the effects of microwave fm applied to the deutron target. No obvious effect was seen with NH_3.

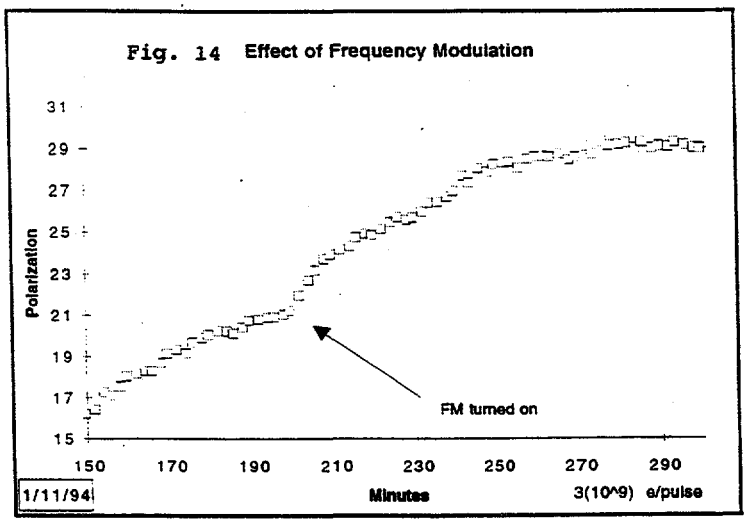

Finally, Fig. 15 shows a graph of deuteron polarization vs residual proton polarization, showing disagreement with the EST hypothesis. This had been noted previously.[15]

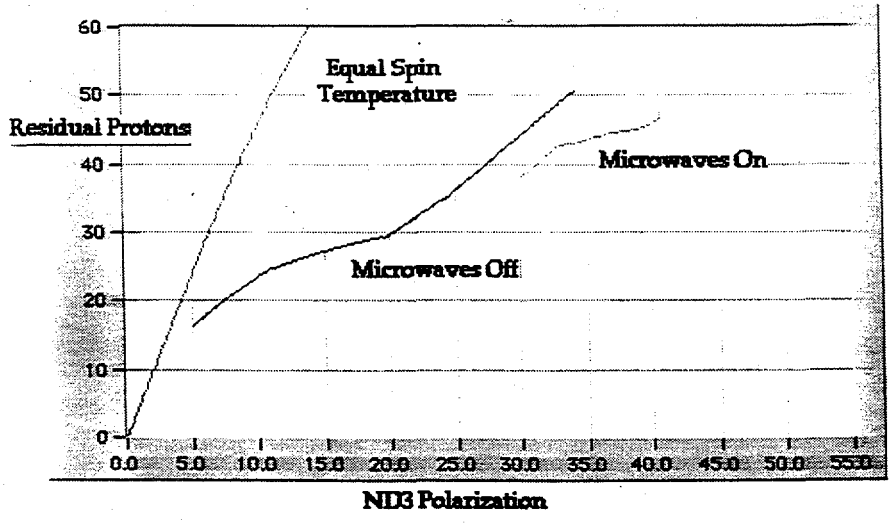

Fig 15. Comparison of deuteron and residual proton polarizations and EST with microwaves on and off.

5. SMC

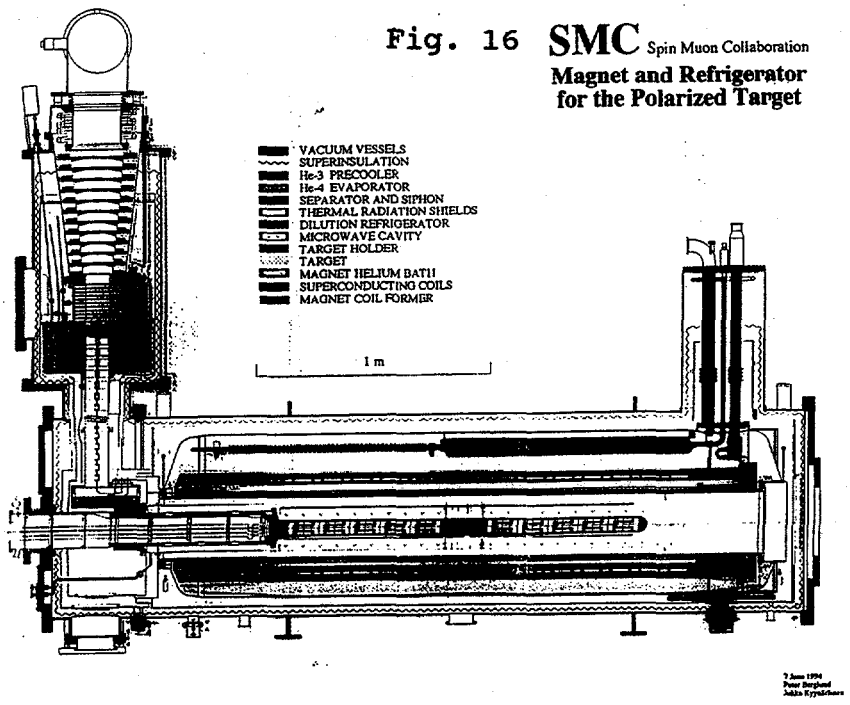

Fig. 16 **SMC** Spin Muon Collaboration
Magnet and Refrigerator for the Polarized Target

Fig. 16 shows the polarized target and superconducting solenoid being used by the SMC collaboration at CERN.[1] A very powerful DR, with a cooling power of 1W at 0.46K, allows two target cells, each 80 cm long x 5cm ϕ, to be polarized in opposite directions. Five NMR coils in each cell monitor the polarization. The magnet operates at 2.5T and the target material used is either butanol or deuterated butanol. Maximum deuteron polarizations of around 50% and proton polarizations of 94% have been achieved. Fig. 17 shows the polarization build-up times of both proton and deuteron.

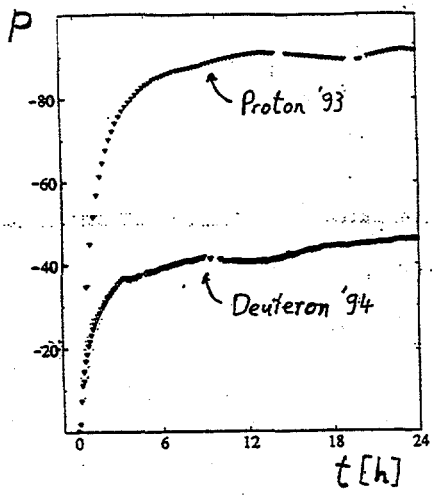

Fig. 17
Proton (1993) and deuteron (1994) polarization build-up in the SMC target.

Because of these very long build-up times, polarization reversal by DNP is not very efficient and so a method of field rotation was used. Use was made of dipole coils built into the solenoid providing a field normal to the solenoid field. The procedure was to reduce the solenoid to 0.5T and ramp the dipole field up to 0.5T. Then the solenoid could be ramped through zero to -0.5T, at which time the dipole starts ramping back to zero while the solenoid continues to full negative field. This procedure was repeated about every five hours with insignificant loss of polarization. It was found during the course of the experiment, because of a recalcitrant microwave power supply, that fm greatly improved the deuteron polarization. The maximum value is about a factor of 2 higher than obtained without fm and the rate of rise is much higher. This is shown in Fig. 18. A smaller effect ($\sim$ 20%) was seen with protons.

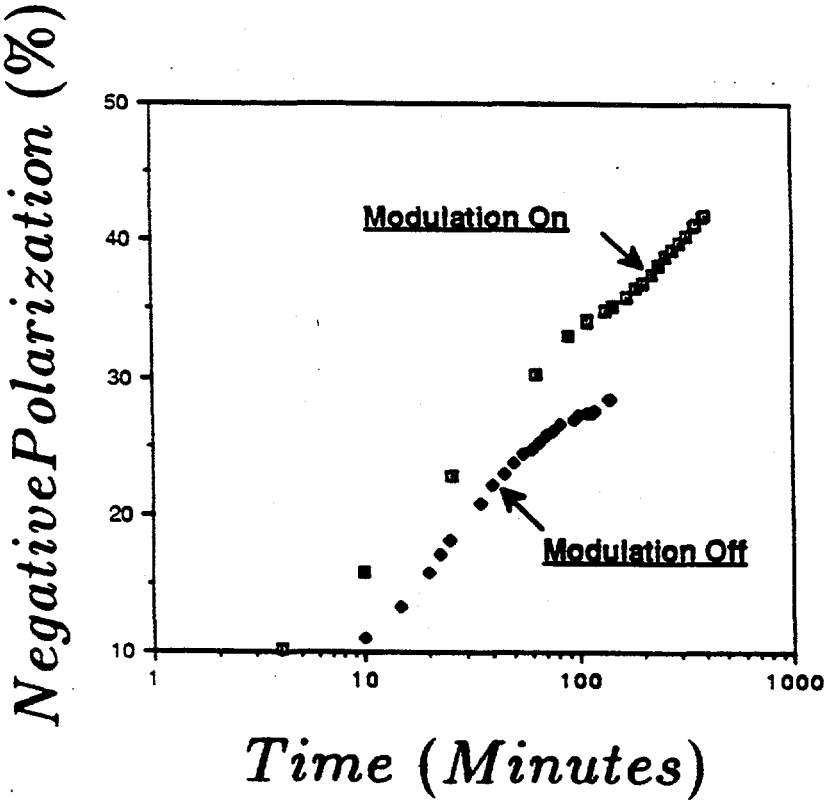

Fig. 18

6. Solid HD Targets

The idea of using frozen HD as a polarized target was first proposed by Honig in 1967.[16] Practical problems relating to relaxation times have delayed implementation until fairly recently. Now two groups are moving towards building such a target for use in low intensity photon and neutron beams.[17]

The method uses the principle of "brute force" (or equilibrium) polarization as shown in Fig. 19. This works for every polarized target material, but very high fields and very low temperatures are necessary to reach the B/T value which gives the high polarizations, (see equation (1)). However, this can take many days or weeks, as the HD

spins are weakly coupled to the lattice. Honig suggested doping with small concentrations ($\sim 10^{-4}$) of ortho-H_2 and/or para-D_2 to provide spin lattice coupling and allow a faster polarization build-up. This is similar to the situation in DNP where the doping leads to faster relaxation and allows the TE polarization to be reached quickly (1 to 2 hours) for calibration measurements. For the HD case, as the polarization builds up, the impurities decay to magnetically inert states, the relaxation times becomes long once again and thus the spins are "frozen".

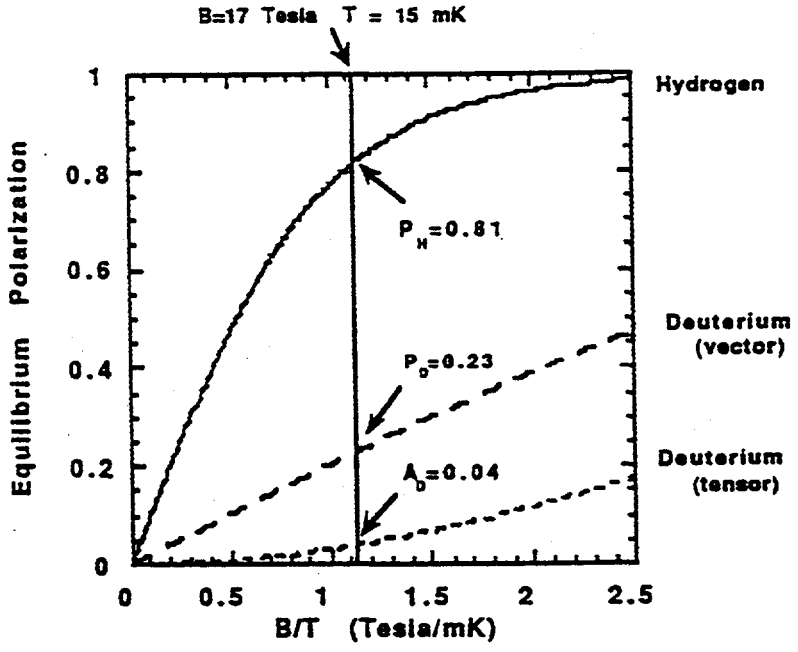

Fig. 19 Equilibrium polarizations for hydrogen and deuterium as a function of the ratio B/T. The 14 Tesla, 15mK conditions indicated correspond to that planned for the SPHICE target.

The proton polarizations obtained in this way are high, $\sim$ 80%, but the deuteron polarizations are only about 20%. Moreover, these polarizations are achieved only after waiting for several decay constants of the impurities. For $o - H_2$, with a constant of 6.25 days, holding at high field/low temperature for 3 to 4 weeks is practical, but for p-D_2, with a constant of 18.2 days, holding for months is not.

The solution is to use only $o - H_2$ to build up the proton polarization and then, by an AFP/DNP technique, transfer the proton polarization to the deuteron. This method takes advantage of the dipolar coupling of H and D nuclei in different HD molecules. This process can be repeated several times so that deuteron polarizations of 50% could be obtained. T_{1d} is still extremely long, so the targets can be extracted from the production cryostat, transported in a special holding dewar and installed in the in-beam cryostat for experiments. At this point, in-beam target lifetimes of $\sim$10 days can be expected with operation at $\sim$1T/1K, with photon beams of 10^6/sec. The

time-line for target production is shown in Fig. 20. Such targets have not yet been used in particle scattering experiments and there are a number of technical issues to be resolved before a favorable comparison can be made with DNP frozen spin targets. These problems are being pursued for experiments at LEGS (Brookhaven) and GRAAL (Grenoble).

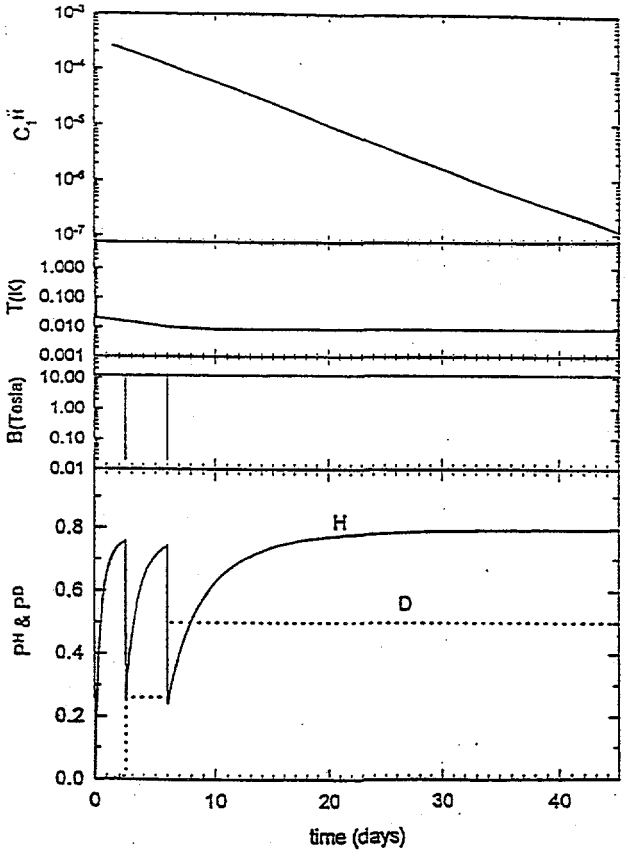

Fig. 20

Time-line of polarization process for solid HD target when both D and H polarizations are to be preserved at 1.5K and moderate supporting fields. c_1^H is the concentration of J = 1 state H_2 (ortho-H_2). c_1^D is less than 10^{-5}. At day 2.5 and day 6, polarization transfer from H to D via "forbidden" rf-induced transitions takes place.

7. Conclusions

Polarized solid targets have reached high polarizations at 1K in the presence of high beam intensities (5 x $10^{11} e^-$/sec).

High polarizations at low temperatures ($\sim$ 200 mk) and very long holding times are now routine.

7.1. Technical developments

Many dilution refrigerator with frozen spin operation. Low mass holding coils at 0.3T - 0.4T.

Microwave fm improves polarization dramatically in deuterated butanol

Adiabatic fast passage now > 90% efficient for some materials.

Development of both chemically and radiation doped materials.

There is now polarized target activity at more than a dozen institutions with at least 5 more developing programs.

References

1. K. Abe et al., to be published in *Phys. Rev. Letts.*.
2. B. Adeva et al, *Phys. Letts.*, **B302**, 533, (1993).
3. *7th Workshop on Polarized Target Materials and Techniques*, (June 20-22, 1994), Bad Honnef, Germany, Proc. to be published in *Nucl. Instr. and Meth.*
4. *11th Int. Symp. for High Energy Spin Physics*, (Sept. 15-22, 1994), Bloomington, Indiana.
5. A. Abragam, *Principles of Nuclear Magnetism*, Oxford, (1986).
6. M. Borghini, *Proton Spin Orientation*, CERN Yellow Report, (1968), **CERN 68-32**.
7. W. de Boer, *J. of Low Temp Phys.*, **22**, 185, (1976).
8. W. de Boer and T.O. Niinikoski, *Nucl. Instr. and Meth.*, **114**, 495, (1974).
9. M. Seely et al., *Nucl. Instr. and Meth.*, **201**, 303, (1982).
10. O.V. Lounasmaa, *Experimental Principles and Methods Below 1K*, *Academic Press*, (1974).
11. G. Court et al., *Nucl. Instr. and Meth.* **A324**, 433, (1993).
12. D.G. Crabb et al., *Proc. of 10th Int. Symp. on High Energy Spin Physics*, (Nagoya, Japan, 1992), *Universal Academy Press*, Eds. T. Hasegawa et al., 375.
13. D.G. Crabb et al., *Phys. Rev. Lett.* **64**, 2627, (1990).
14. B. Boden et al., *Particles and Fields* **49**, 175, (1991).
15. G.R. Court et al., *Proc. of 4th Int. Workshop on Polarized Target Materials and Techniques*, (Bad Honnef, Germany, 1984), ed. W. Meyes, **53**.
16. A. Honig, *Phys. Rev. Lett.* **19**, 1009, (1967).
17. J.P. Didelez, *Nuclear Physics News Europe*, 4, 10, (1994).

Polarized Electron Sources

C. Sinclair
CEBAF, Newport News

SUMMARY

Recent developments of strained layer and multilayer semiconductor photocathodes permit reasonably reliable delivery of low average current electron beams with beam polarization of 80 percent or greater. Work is in progress at several laboratories to improve the quantum efficiency of these photocathodes, permitting operation at higher average beam current as required by facilities such as CEBAF. Developments which so promise to improve the operational reliability and "up time" from such cathodes are also underway. The most recent operational experience with these polarized sources will be reviewed, and the improvements likely from the developmental work will be discussed.

MEASUREMENTS OF THE g_1^p SPIN STRUCTURE FUNCTION

Jechiel LICHTENSTADT*
School of Physics and Astronomy
Raymond and Beverly Sackler Faculty of Exact Sciences, Tel Aviv University
69978 Tel Aviv ISRAEL

On behalf of the Spin Muon Collaboration

ABSTRACT

The spin structure function g_1^p of the proton has been measured by deep inelastic scattering of polarized muons from polarized protons. The data were taken over the kinematic range $0.003 \leq x_{Bj} \leq 0.7$ and $1\ \mathrm{GeV}^2 \leq Q^2 \leq 60\ \mathrm{GeV}^2$. The first moment $\Gamma_1^p = \int_0^1 g_1^p(x)dx$ was evaluated and compared to the Ellis-Jaffe sum rule. The consistency of existing proton deuteron and neutron data is discussed. Combination of the data allows a test the fundamental Bjorken sum rule which is confirmed at the level of 10% of its theoretical value, when high QCD corrections are considered. The contribution of the quark spins to the nucleon spin is evaluated within the quark-parton model.

1. Introduction.

Deep inelastic scattering of longitudinally polarized leptons from polarized nucleons determine the nucleon spin dependent function g_1. These measurements allow us to test experimentally QCD sum rules. In the quark parton model the first moment of the spin dependent structure function is related to the contributions of the quark spins to the nucleon spin by:

$$\Gamma_1^{p(n)} = \int_0^1 g_1^{p(n)}(x)dx = \sum_f e_f^2 \Delta q_f \tag{1}$$

The fundamental Bjorken sum rule[1] is a rigorous prediction of QCD and relates the proton and neutron sum rules to the neutron beta decay:

$$\int_0^1 [g_1^p(x) - g_1^n(x)]dx = \frac{1}{6} g_A (1 - \frac{\alpha_s}{\pi}) \tag{2}$$

(where high order QCD corrections were omitted). Assuming SU(3) flavor symmetry and that the strange sea within the nucleon is unpolarized Ellis and Jaffe wrote individual sum rules for the proton and the neutron.[2] The Ellis-Jaffe sum rule can be

*Supported by The Israel Science Foundation of The Israeli Academy of Sciences.

written as:

$$\int_0^1 g_1^{p(n)}(x)dx = \frac{1}{12}\left[+(-)g_A + \frac{5}{3}(3F - D)\right](1 - \frac{\alpha_s}{\pi}) \quad (3)$$

where the (-) refers to the neutron sum rule,

$$g_A = F + D = \Delta u - \Delta d \quad (4)$$

and (under exact SU(3) symmetry)

$$3F - D = \Delta u + \Delta d - 2\Delta s \quad (5)$$

and F and D are determined from the hyperon weak decays. More generally the sum rules can be related to the total contribution of the quark spins to the nucleon spin,

$$\int_0^1 g_1^{p(n)}(x)dx = \frac{1}{12}\left\{\left[+(-)g_A + \frac{(3F - D)}{3}\right](1 - \frac{\alpha_s}{\pi}) + \frac{4}{3}\left[1 - \frac{33 - 8f}{33 - 2f}\frac{\alpha_s}{\pi}\right]\Delta\Sigma\right\} \quad (6)$$

Measurements of the spin dependent structure function of the proton were carried out initially at SLAC by the E80/E130 collaborations[3] using polarized electrons, covering the x region of $0.1 \leq x \leq 0.7$. Using polarized muons, the EM Collaboration[4,5] extended these measurements down to $x = 0.015$. The first moment of g_1 inferred from these measurements was $\Gamma_1^p = 0.126 \pm 0.010(\text{stat.}) \pm 0.015$ (syst.). This result implied that the contribution of the quark spins to the nucleon spin was as low as $\Delta\Sigma = 0.12 \pm 0.09 \pm 0.14$ and when exact SU(3) symmetry was assumed it further implied that the 'strange sea' is polarized with a contribution of $\Delta s = -0.19 \pm 0.032 \pm 0.046$. These conclusions were quite contrary to the naive parton model and coined the question 'What carries the nucleon spin?'

These results triggered new experiments with two major goals. The first was to repeat the measurement with better precision, by reducing both the systematic and statistical errors, and by extending the measurements to lower x values. The last point is extremely important since the evaluation of the first moment depends quite critically on the extrapolation of the measured g_1 beyond the measured region, down to $x = 0$. Thus, suggestions[6] of a diverging function at low x. which in turn would increase the value of the first moment and exhaust the sum rule, could be put to test.

The second goal was to test experimentally the fundamental (model independent) Bjorken sum rule.[1] This test would require measurements of both the proton and the neutron spin dependent structure functions. In the absence of a neutron target, the latter could be extracted from the spin dependent structure function of the deuteron using a longitudinally polarized deuteron target.

The Spin Muon Collaboration (SMC) was set up to achieve these goals. Measurements were carried out on the deuteron[7] and on the proton.[8] These measurements resulted in a better evaluation of the proton first moments, and with the deuteron measurement allowed a first test of the Bjorken sum rule. The neutron spin structure function was measured at SLAC by the E142 collaboration[9] using polarized electrons and a polarized ^{3}He target. Recently, asymmetry measurements were carried out at SLAC by the E143 collaboration on the proton[10] and the deuteron.[11]

The new measurements allowed a new evaluation of the quark spin contribution of the nucleon, which indicate that while it is significantly higher than the original results it is still well below the naive parton model prediction.

2. Experimental setup.

2.1. General.

The SMC experiment at CERN[7,8] used positive muon beams, with an average energy of 100 GeV for the deuteron measurement, and of 190 GeV for the proton measurement. The beam intensity was 4×10^7 muons/spill, with a spill time of 2.4 s, in a 14.4 s cycle.

The experiment used a large polarized target. The scattered muons were detected and analyzed by the spectrometer. The muons are naturally polarized, and their polarization was measured by a polarimeter which was set up downstream of the spectrometer and its detector assembly. The polarization was determined from the shape of the energy spectrum of the positrons from the muon decay.

2.2. The polarized target.

Protons were polarized using a new target assembly, which was built for this experiment. The target design is similar to that used in the EMC measurement of the proton[5,12,13] and used also by the SMC for the first deuteron measurements. It contains two cells (60 cm long and 5 cm in diameter) which are placed in a superconducting solenoid and a ^{3}He/^{4}He dilution refrigerator. An additional dipole can provide up to 0.5 T in the vertical direction. The two cells are polarized simultaneously in opposite directions.

The solenoid provides a 2.5 T longitudinal field with its axis along the beam direction, with an homogeneity of 2×10^{-5}. The refrigerator provides about 0.3 W of cooling power during polarization which is achieved at about 0.3 K. The target material consisted of butanol beads, (or deuterated butanol for the deuteron measurement) in which paramagnetic molecules were dissolved. Dynamic nuclear polarization was achieved by applying microwave power with a frequency near that of the resonance frequency of the paramagnetic electrons. To achieve opposite polarization in the two target cells, microwaves with slightly different frequencies were applied in each cell. Frequency modulation of the microwave speeded up the polarization time and enhanced the maximum proton polarization by about 6%. This enhancement was much more significant for the deuteron polarization, where deuteron polarizations exceeding 0.5 were achieved, and the polarization time was speeded up considerably as well. The polarization was was measured using 10 NMR coils imbedded in the target material.[14] It allowed a continuous measurement of the target polarization with an overall accuracy of less than 5%. The mean proton polarization in the target during data taking was $P_T = 0.86 \pm 0.03$.

Since the muons are naturally polarized, the target spin orientation was reversed. This was done by rotating the magnetic field direction, superimposing the solenoid and dipole fields during the rotation process. Only small polarization losses occurred during the rotation. The relatively fast rotation process, allowed frequent polarization reversals at intervals of about 5 hours. This was crucial in reducing the errors due

to possible false asymmetries caused by variations with time in the acceptance of the detection system.

2.3. The muon spectrometer.

The muon spectrometer is based on the apparatus constructed by the EM Collaboration,[5,15] but has been upgraded by adding planes of proportional chambers, and a fine segmentation hodoscope close to the beam, which allowed triggering on events with small scattering angles. The spectrometer setup is shown schematically in Fig. 1. The incident muon momentum is determined by a bending magnet and several planes of scintillator hodoscopes located upstream of the polarized target. The scattered muon is identified by hits in the 'muon tagging region' beyond the 2m hadron absorber. Particles in this region are assumed to be muons. The scattered muons are momentum analyzed by the forward spectrometer magnet (FSM). The muon trajectory is determined from hits in about 150 planes of proportional chambers, drift chambers and streamer tubes. The large number of planes increased the redundancy in the track reconstruction and minimized the effects of individual plane inefficiencies on the overall track-reconstruction efficiency. The incident and scattered muon tracks determined the interaction vertex in the target. The vertex resolution was about 30 mm in the beam direction, and 0.3 mm in the transverse direction. The muon momentum resolution was about 3×10^{-3}.

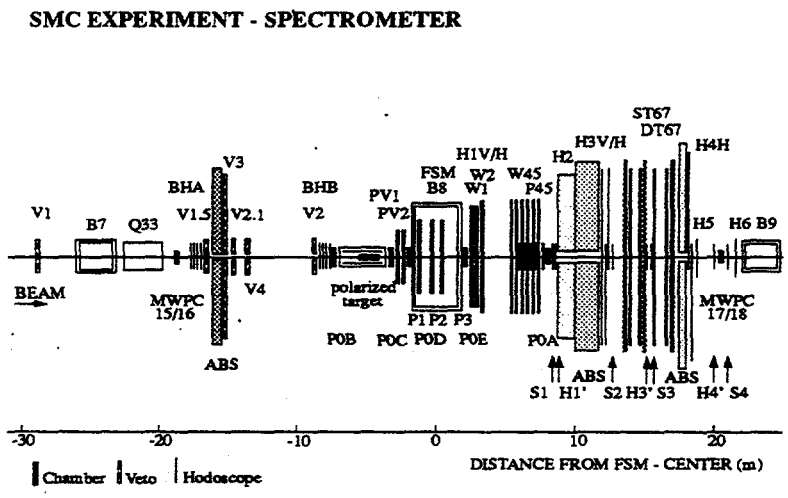

Fig. 1. The SMC muon spectrometer.

2.4. *The muon beam polarimeter.*

The muons are naturally polarized due to parity violating in the weak decay of $\pi \rightarrow \mu\nu$. The beam polarization can be determined[16] from the shape of the energy spectrum of the positrons from the decay $\mu^+ \rightarrow e^+\nu_e\bar{\nu}_\mu$. The dependence of the positron energy spectrum on the parent muon polarization is shown in Fig. 2. The spectra are plotted as a function of the ratio of the electron and muon energies $y = E_e/E_\mu$.

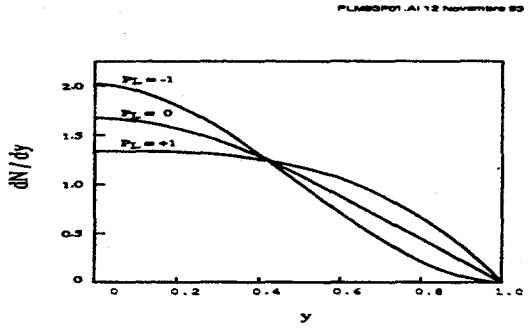

Fig. 2. Energy spectrum of positrons from muon decay for longitudinal muon polarizations of P_μ=1 , 0, and -1

A beam polarimeter was set up downstream the muon spectrometer. The polarimeter set up is shown in Fig. 3. It consists of a $30m$ long field free decay path, an

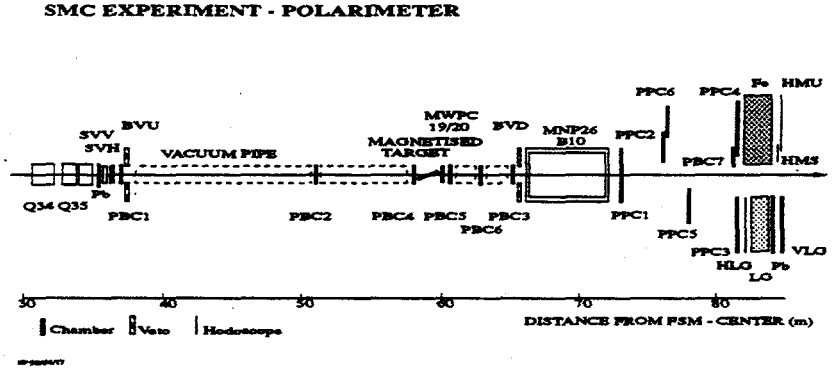

Fig. 3. The SMC polarimeter. Shown are both, electron or positron (deflected right) and muon (deflected left) detection arms. Only the positron arm was used in the 'muon decay' polarimeter.

analyzing magnet (MNP26) which determines the positron momenta, and a lead-glass

calorimeter which identifies the decay positrons (which are deflected to the right in the figure). The parent muon is identified upstream of the field-free decay path by a shower veto hodoscope, which consists of lead radiators followed by two hodoscopes. Positrons produced upstream of the decay path induce showers in the lead radiators, and can be separated from muons by their high pulses in the scintillators. Particle trajectories are defined by 2 telescopes, upstream and downstream the analyzing magnet. Each telescope is made of three modules of proportional chambers. The decay positron is identified by its energy deposition in an electromagnetic calorimeter, which provides an efficient discrimination against muons.

The parent muon momentum is measured by the beam momentum station, upstream the SMC experiment. The positron momentum is determined by the bend in the analyzing spectrometer, thus $y = E_e/E_\mu$ is determined with a relatively small error. The y distribution which is sensitive to the parent muon polarization, and the spectrum is fitted with a polynomial in y. A detailed description of the the polarimeter is given in Ref.17.

The polarization was measured as $P_\mu = -0.803 \pm 0.029 \pm 0.020$ for the 190 GeV beam used to measure the proton spin structure function, and $P_\mu = -0.82 \pm 0.06$ for the 100 GeV beam used in the deuteron experiment. These values are in good agreement with Monte Carlo simulations of the beam transport system.[18]

The beam polarization was determined also by measuring the asymmetry in polarized $\vec{\mu} - \vec{e}$ scattering. The set up of the polarimeter for this mode is also shown in Fig. 3. In this mode the muons are scattered off polarized electrons in a polarized iron target. An additional telescope and muon detector were placed downstream the analyzing magnet, and both, the scattered muon (which is deflected to the left) and the scattered electron (deflected right) are detected in coincidence. Results from this measurement will provide an additional measurement of the beam polarization with different systematic errors.

3. Results.

3.1. Analysis.

The virtual-photon proton asymmetry A_1^p is related to the measured asymmetry A^p

$$A_1^p = \frac{\sigma_{1/2} - \sigma_{3/2}}{\sigma_{1/2} + \sigma_{3/2}} = \frac{A^p}{D} - \eta A_2^p \tag{7}$$

where D is the depolarization factor and η is a kinematical factor, which is very small in the kinematic region of the muon experiment. The A_2 asymmetry is due to the helicity spin flip amplitude in forward photon nucleon Compton scattering. This asymmetry is constrained by the positivity limit $| A_2 | \leq \sqrt{R}$. However, this asymmetry was measured by us in a dedicated experiment where the longitudinally polarized muons were scattered off transversely polarized protons.[19] The measured asymmetries A_2^p, shown in Fig. 4, are compatible with zero. Thus corrections due to the second term ηA_2 were neglected, and possible effects were accounted for in the systematic error.

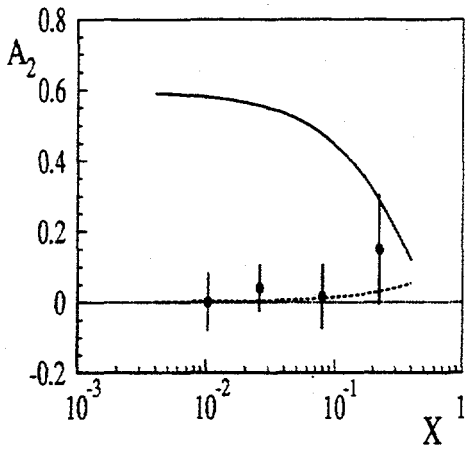

Fig. 4. The asymmetry A_2 as a function of x. The solid line is $\sqrt{R}$. The dashed line is the result for g_2 obtained from g_1, with no twist-3 contributions.

The A_1 asymmetries were extracted from combinations of data sets with different target-beam polarization orientations. Each set consists of data from the upstream and downstream targets which are polarized in opposite directions and are exposed to the same beam flux. The events are weighted by corresponding values of R and the dilution factor f. Since data are taken simultaneously from both target cells which are polarized in opposite directions and are exposed to the same incident muon beam, the asymmetry does not depend on the incident beam flux, target material or absolute values of the spectrometer acceptances. The only assumption in obtaining A_1 is that the ratio of the spectrometer acceptances to the upstream and downstream target cells, $r = a_u/a_d$, remains constant within the measurement period between polarization reversals.

The data sample of the proton consists of 4.4×10^6 events, and covers the kinematic region of $0.003 \leq x \leq 0.7$ and $1 \leq Q^2 \leq 60$ GeV^2. Kinematic cuts were applied on the data sample to eliminate events which required large radiative corrections and to minimize smearing effects. Other cuts ensured the same beam flux on both target cells, good separation between events from the two target halves and rejection of muons which are not 'beam-muons' (but originate from π decays, of pions which were produced in the target).

3.2. g_1^p.

The spin dependent structure function g_1 is obtained from the A_1 asymmetries by:

$$g_1^p(x,Q^2) = \frac{A_1^p(x,Q^2)F_2^p(x,Q^2)}{2x[1+R(x,Q^2)]} \tag{8}$$

The unpolarized structure function $F_2(x,Q^2)$ was taken from the NMC parametrization[20] and R from a global fit of SLAC data.[21] The measured spin structure function of the proton $g_1^p(x)$ is shown in Fig. 5. Since the QCD sum rules are evaluated at a fixed

Q^2, g_1 was also calculated at Q_0^2=10 GeV^2 which represents the average momentum transfer of the data set. This procedure assumes that $A_1(Q^2, x)$ is independent of Q^2 which is consistent with our data as well as with the data measured in other experiments. The comparison of the A_1 asymmetries with those of EMC[4,5] and of the $E143$ collaboration[10] are shown in Fig. 6.

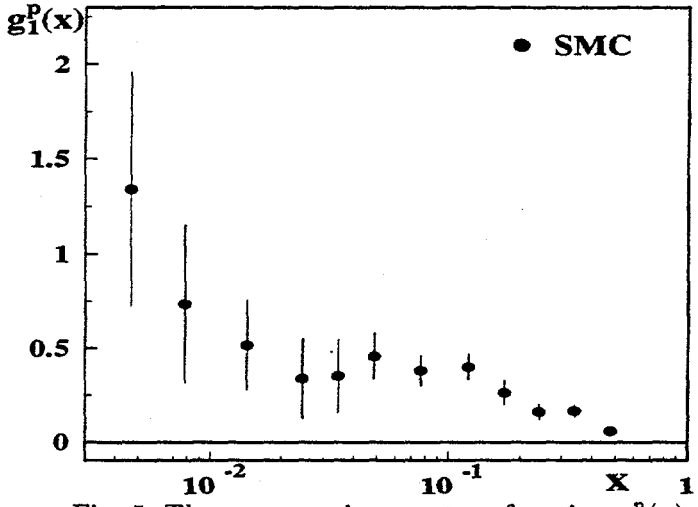

Fig. 5. The proton spin structure function $g_1^p(x)$.

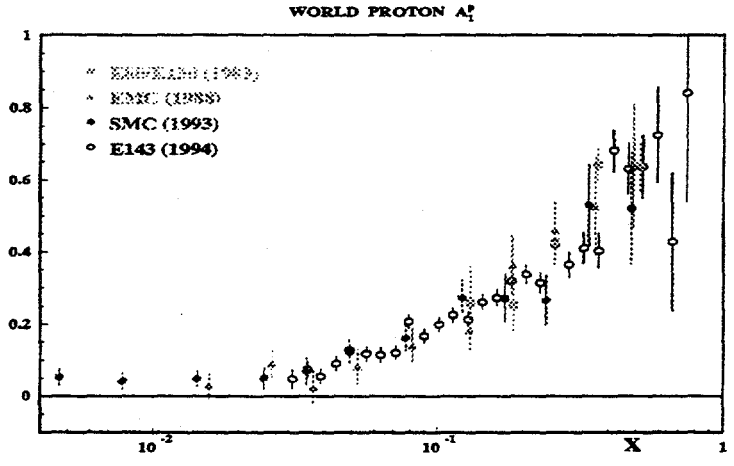

Fig. 6. Proton asymmetries A_1^p from the measurements of SMC, SLAC-E80/E130, EMC and SLAC-E143

The spin structure function of the proton at fixed Q_0^2=10 GeV^2 is shown in Fig. 7. Also shown is the dependence of the evaluated first moment on the low x limit of the integral.

The integral $\int g_1(x)dx$ was evaluated at Q_0^2 =10 GeV^2. The integral over the measured range is

$$\int_{0.03}^{0.7} g_1^p(x)dx = 0.131 \pm 0.011(stat.) \pm 0.011(syst.) \qquad (9)$$

The contributions to the integral from the *unmeasured* region of $x > 0.7$ was estimated assuming a constant value of $A_1^p = 0.7 \pm 0.3$. It is consistent with the bound $A_1 < 1$. and with QCD predictions[22] of the behavior of A_1 at large x: $A_1 \to 1$ with $x \to 1$. For the low x region $x < 0.003$ a Regge type dependence $g_1(x) = constant$ was assumed and the constant was fixed by a fit to the two measured lowest x data points. These contributions amount to

$$\int_{0.7}^{1} g_1(x)dx = 0.0015 \pm 0.0007 \tag{10}$$

$$\int_{0}^{0.003} g_1(x)dx = 0.004 \pm 0.002 \tag{11}$$

With these extrapolations the results for the first moment of g_1 is

$$\Gamma_1^p(Q_0^2 = 10\ GeV^2) = \int_0^1 g_1(x)dx = 0.136 \pm 0.011 \pm 0.011 \tag{12}$$

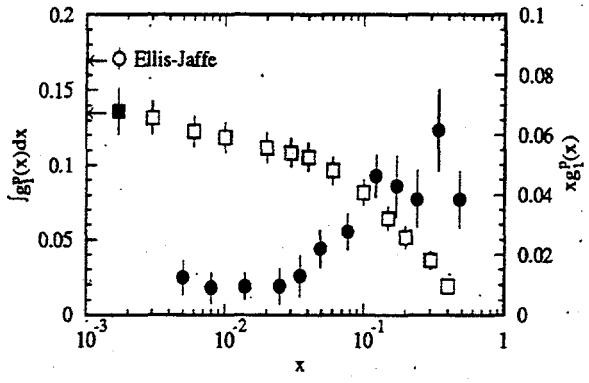

Fig. 7. The proton spin structure function $g_1^p(x)$ at fixed Q_0^2=10GeV^2. Also shown (open squares) is the dependence of the first moment of g_1 on the low x limit of the integral.

3.3. Comparison with other experiments.

The measured asymmetries are in excellent agreement with those obtained in previous measurements, as well as with the E143 results as was shown in Fig. 6. The spin structure function, calculated at 5 GeV^2 with all available data is shown in Fig. 8, demonstrating the good agreement of the evaluated spin structure functions by the various experiments, measured at different Q_0^2. This further supports the assumption of negligible Q^2 dependence in the measured A_1^p asymmetries. Similarly the neutron A_n^1 asymmetries measured by E142 at SLAC were shown[23] to be compatible with those of the deuteron[7] when they were combined with the proton asymmetries A_1^p and compared to the deuteron asymmetries.

It is thus appropriate to comment that the different conclusions on the evaluated first moment Γ_1^p as well as on the contribution of the quarks to the nucleon spin extracted from the first moment, do not arise from the actual measurements. Rather, these differences may stem from different parametrizations used for F_2 or R used to obtain the spin dependent function, and from the new measurements in the low x region which affect the extrapolation and thus the value of the first moment. New experimental values for F and D also affect the evaluated quark spin contributions to the nucleon spin extracted from the measured first moment.[24,25]

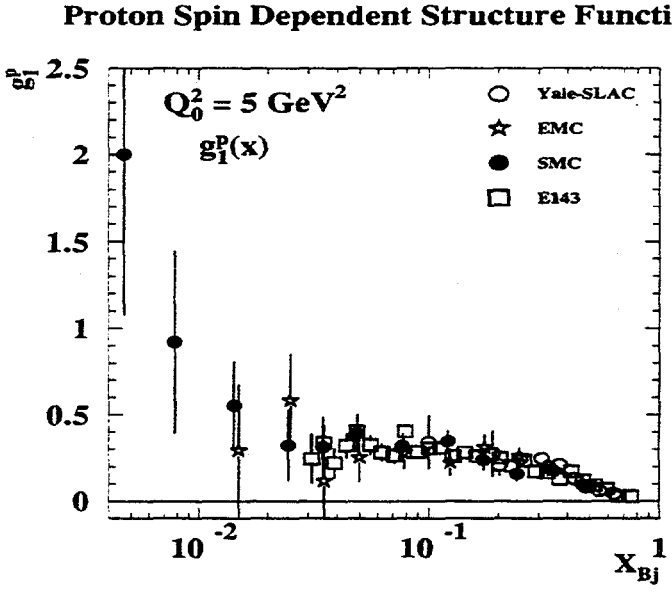

Fig. 8. Compilation of $g_1^p(x)$ measurements evaluated at 5 GeV^2.

4. QCD Sum Rules and the Spin Content of the Nucleon.

4.1. QCD high order corrections.

Perturbative QCD corrections were calculated for the Bjorken sum rule as well as for the Ellis-Jaffe sum rules. Following Larin,[26,27] the Ellis-Jaffe sum rule is modified by the high order QCD corrections and reads:

$$\Gamma_1^{p(n)} = \frac{1}{12} C_{ns}(\frac{\alpha_s}{\pi}) \left[+(-) g_A + \frac{(3F - D)}{3} \right] + C_s(\frac{\alpha_s}{\pi}) \frac{1}{9} \Delta\Sigma \qquad (13)$$

where C_{ns} and C_s are polynomials with coefficients which depend on the number of flavors, and include the high order QCD corrections.

Ellis and Karliner[28,29] have shown the importance of including the next to leading order corrections in evaluating the sum rules at different Q_0^2, and their effect on extracting the contribution of the quark spins to the nucleon spin $\Delta\Sigma$. While the values of $\Delta\Sigma$ obtained from different experiments was at variance when Eq. 6 (which assumed

only first order corrections) was used, these discrepancies disappeared when the high order corrections were introduced.

We use these equations to evaluate the QCD sum rules, and to extract the quark contribution to the nucleon spin, $\Delta\Sigma$ from the experimental values of the first moments.

4.2. The Ellis-Jaffe sum rule.

The result for the first moment of the proton spin structure function at $Q_0^2 = 10GeV^2$ obtained by the SMC measurement is $\Gamma_1^p(Q_0^2 = 10GeV^2) = 0.136 \pm 0.011 \pm 0.011$. Using[30] $\alpha_s(M_z^2) = 0.117$ and four quark flavors (which corresponds to $\alpha_s(10GeV^2) = 0.24 \pm 0.02$, the Ellis-Jaffe sum rule was evaluated at Q_0^2=10 GeV^2, using Eq. 13. It yields

$$\Gamma_1^p(Q_0^2 = 10GeV^2) = 0.172 \pm 0.003 \qquad (Theory) \tag{14}$$

which is more than 2 standard deviations above the experimental value.

The first moment of the proton spin structure function was evaluated also using all available proton measurements. These include the first E80/E130 measurement, the EMC results, and the recent measurement by SLAC-E143. As mentioned above, no Q^2 dependence was observed in the measured asymmetries within the experimental errors, and g_1 was evaluated using Eq. 8. To avoid large Q^2 evolution the first moment of the combined data was evaluated at 5 GeV^2. The $A_1^p(x)$ were combined and the systematic errors were treated taking into account that some of them are correlated between the different experiments. The overall error in each bin was estimated using Monte Carlo techniques.[31]

The E143 data, which were taken in narrower x bins than those of the SMC data, were combined after integrating g_1 over the larger SMC bins, and combining these values with those obtained from the other experiments (at the same Q_0^2). The data were weighted by their respective uncorrelated errors to obtain the combined value for each bin. Obviously, the low x behavior is determined by the SMC data, which in turn determines the contribution to the integral from the unmeasured region $x \leq 0.003$.

The result for the proton first moment is

$$\Gamma_1^p(Q_0^2 = 5GeV^2) = 0.137 \pm 0.010 \qquad (All\ proton\ data). \tag{15}$$

4.3. The Bjorken sum rule.

The new measurements enable us to test experimentally the bjorken sum rule. The first measurements of the deuteron[7] g_1^d were combined with the E80/E130/EMC proton data to obtain the neutron spin dependent structure function and provided the first test of the Bjorken sum rule[7]:

$$\Gamma_1^p - \Gamma_1^n = \int_0^1 [g_1^p(x) - g_1^n(x)]dx = 0.20 \pm 0.05 \pm 0.04 \quad (Q_0^2 = 4.6\ GeV^2) \tag{16}$$

Consequent measurement of g_1^n by E142 at SLAC seemed initially to be at variance with the sum rule. However, when combined with the deuteron data to obtain a better evaluation of the low x behavior, the experimental value for the Bjorken sum

rule was evaluated[23] and was shown to be in agreement with the theoretical prediction for the sum rule:

$$\Gamma_1^p - \Gamma_1^n = 0.183 \pm 0.004 \quad (Theory\ at\ Q_0^2 = 5\ GeV^2) \tag{17}$$

The recent measurements of the proton spin structure function by SMC and by SLAC E142, improved the statistical uncertainty of the measurements and extended the measured x region of g_1^p. Using the value for the proton first moment obtained from all available data (Eq. 15), and the preliminary value for first moment of the deuteron spin structure function of E143[11] reevaluated at Q_0^2=5 GeV^2, Γ_1^d=0.041 $\pm$ 0.005 we can obtain an improved value for the Bjorken sum rule. Correcting for the probability of the deuteron to be in a D-state

$$\Gamma_1^d = (\Gamma_1^p + \Gamma_1^n)(\frac{1 - 1.5\omega_D}{2}) \tag{18}$$

with ω_D=0.058[32] we obtain for the Bjorken sum rule:

$$\Gamma_1^p - \Gamma_1^n = 0.184 \pm 0.022 \quad (Q_0^2 = 5\ GeV^2) \tag{19}$$

in excellent agreement with the theoretical value.

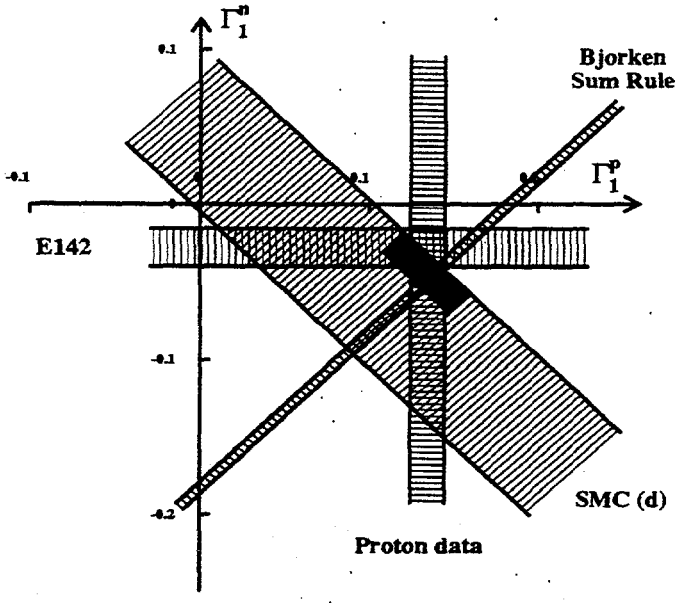

Fig. 9. The moments Γ_1^p, Γ_1^n and Γ_1^d. evaluated at Q_0^2=5 GeV^2. Γ_1^p is from the compilation of all proton data, Γ_1^n from SLAC-E142.

We show in Fig. 9 a comparison of the bjorken sum rule with the first moments Γ_1^d, Γ_1^p and Γ_1^n. Also shown is the preliminary results for Γ_1^d by E143, evaluated at 5

GeV^2. These results, and in particular the proton and deuteron first moments show excellent agreement with the Bjorken sum rule.

The recent measurements of g_1^d by the SMC will extend the kinematic range of g_1^d to lower x values, which will further reduce the error on the deuteron first moment and consequently on the sum rule.

4.4. The quark contribution to the nucleon spin.

In the quark parton model, and with the assumption of exact SU(3), the first moments are related to the contribution of the quark spins to the nucleon spin.

Using Eq. 13 with the high order QCD corrections we obtain $\Delta\Sigma$ from the various measured first moments. For the proton we use the values obtained by SMC (at $Q^2 = 10GeV^2$), by E143 (Q_0^2=3 GeV^2) and the value obtained from a compilation of all available proton data (Eq. 15), We also use the preliminary result for Γ_1^d of E143, and Γ_1^n of E142.

With

$$\Delta s = \frac{\Delta\Sigma - (3F - D)}{3} \tag{20}$$

we obtain the contribution of the 'strange sea' to the nucleon spin. We show in Fig. 10 the values of Δs versus $\Delta\Sigma$ obtained from the various measurements.

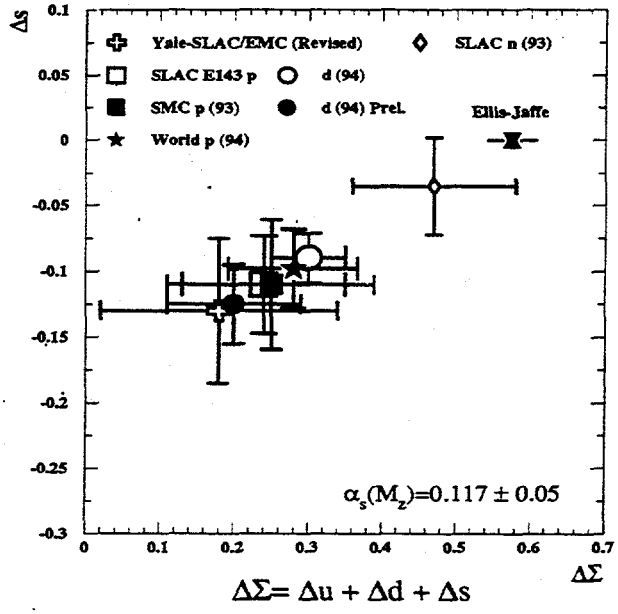

Fig. 10. Strange sea polarization versus total spin contribution

The values indicate that the total contribution of the quark spins to the nucleon spin is about $\Delta\Sigma \approx 0.3 \pm 0.1$ and implies that strange sea is polarized and contributes $\Delta s \approx -0.10 \pm 0.03$. It will be interesting to examine the effect of SU(3) symmetry breaking[33] on these conclusions.

5. Conclusions.

New experiments of polarized deep inelastic lepton scattering provided us with high quality data of the spin dependent structure functions of the proton and the neutron. They allow meaningful tests of the Bjorken sum rule, and the individual Ellis-Jaffe sum rules for the proton and the neutron. High order QCD corrections were calculated for the sum rules.

The asymmetries measured by the different experiments are in excellent agreement with each other.

The Bjorken sum rule is confirmed to within one standard deviation from its theoretical value at the level of 10%. The evaluated first moments of the spin structure functions are about 2 standard deviations below the theoretical predictions for the Ellis-Jaffe sum rules.

The contribution of the quark spins to the nucleon spin, inferred from these data is around 0.3 ± 0.1. When exact SU(3) symmetry is assumed, the contribution of the strange sea can be extracted, which is about -0.1 ± 0.03. It would be interesting to study the effect of SU(3) symmetry breaking on these conclusions.

6. Outlook

Additional experiments are presently underway, which will provide us with more data. The SMC measured the deuteron structure function in 1994, down to x=0.003, and also reduced significantly the statistical errors. These data, together with the results of E143 at SLAC are very important to get a good evaluation of the deuteron first moment, from which the neutron structure function can be obtained. Future experimental runs by SMC, by the E154 and E155 at SLAC and by the HERMES collaboration[34] at HERA will more than double the existing data. These results will improve significantly the experimental value for the Bjorken sum rule, and will give us a better handle to study the Q^2 dependence of the asymmetries and hence of the spin structure functions.

The low x region, beyond x=0.003 is not accessible presently by any of these experiments. The behavior of the spin structure function in this region is very interesting and has been subject to theoretical works[35,36] on the behavior of the spin structure functions at low x. Investigation of this x region would be possible at HERA, if the protons are polarized for polarized electron-proton experiments. These, will be the challenge of the next generation of spin asymmetry measurements.

References

1. J.D. Bjorken, Phys. Rev. 148 (1966) 1467; Phys. Rev. D1 (1970) 1376.
2. J. Ellis and R.L. Jaffe, Phys. Rev. D9 (1974) 1444; D10 (1974) 1669.
3. SLAC E-80, M.J. Alguard et al., Phys. Rev. Lett. 37 (1976) 1261; ibid. 41 (1978) 70; SLAC E-130, G. Baum et al., Phys. Rev. Lett. 51 (1983) 1135.
4. EMC, J. Ashman et al., Phys. Lett. B206, (1988) 364;
5. EMC, J. Ashman et al., Nucl. Phys. B328 (1989) 1.
6. F. E. Close and R. G. Roberts, Phys. Rev. Lett. 60 (1988) 1471.
7. SMC, B. Adeva et al., Phys. Lett. B302 (1993) 533.
8. SMC, D. Adams et al., Phys. Lett. B329 (1994) 399.

9. E-142, P.L. Anthony et al., Phys. Rev. Lett. 71 (1993) 959.
10. E-143, K. Abe et al., Phys. Rev. Lett. 74 (1995) 346.
11. E-143, K. Abe et al., SLAC-Pub 6734 (1995).
12. T.O. Niinikoski, Nucl. Instrum Methods, 192 (1982) 151
13. S.C. Brown et al., Proc. 4th Int. Workshop on Polarized Target Materials and techniques (Bad Honnef, 1984), Ed. W. Meyer, p. 102.
14. SMC, B. Adeva et al., Nucl. Instrum. Meth. A349 (1994) 334.
15. EMC, O.C. Allkofer et al., Nucl. Instrum Methods, 179 (1981) 445
16. T. D. Lee and C. S. Wu, Ann. Rev. Nucl. Sci. 15 (1965).
17. SMC, B. Adeva et al., Nucl. Instrum. Methods A343 (1994) 363.
18. N. Doble, L. Gatignon, G. van Holtey and F. Novoskoltsev Nucl. Instrum. Methods A343 (1994) 351.
19. SMC, D. Adams et al., Phys. Lett. B336 (1994) 125.
20. NMC, P.Amaudruz et al., Phys. Lett. B 295 (1992) 159 and CERN-PPE/91-124 (July 1992).
21. L. W. Whitlow et al., Phys. Lett B250 (1990) 193
22. S. J. Brodsky, M. Burkardt and I. Schmidt SLAC-PUB-6087 (1994), Submitted to Nucl. Phys. B.
23. SMC, B. Adeva et al., Phys. Lett. B320 (1994) 400.
24. F. E. Close and R. G. Roberts, Phys. Lett. B 316 (1993) 165.
25. S. Y. Hsueh, et al., Phys. Rev. D 38 (1988) 2056.
26. S.A. Larin and J.A.M. Vermaseren, Phys. Lett. B259 (1991) 345.
27. S.A. Larin, Phys. Lett. B 334 (1994) 192.
28. J. Ellis and M. Karliner Phys. Lett. B 313 (1993) 131.
29. J. Ellis and M. Karliner Phys. Lett. B 341 (1995) 397.
30. Particle Data Group, Phys. Rev. D45 (1994) 1173.
31. The SM Collaboration, to be published.
32. M. Lancombe et al., Phys. Lett B 101 (1981) 139.
33. H. J. Lipkin, Phys. Lett. B 337 (1994) 157.
34. HERMES Collaboration, HERMES Proposal, DESY 1990; Technical Design Report, DESY, July 1993.
35. F. E. Close and R. G. Roberts, Phys. Lett. B 336 (1994) 257.
36. S.D. Bass and P.V. Landshoff Phys. Lett. B 336 (1994) 537.

MEASUREMENTS OF THE PROTON AND NEUTRON SPIN STRUCTURE AT SLAC *

OSCAR A. RONDON†
Institute of Nuclear and Particle Physics, University of Virginia
Charlottesville, VA 22901

ABSTRACT

The deep inelastic polarized structure functions $g_1^{p,d}$ and $g_2^{p,d}$ have been recently measured at the Stanford Linear Accelerator Center (SLAC) End Station A facility by the E143 Collaboration using 29.1 GeV, 16.2 and 9.7 GeV longitudinally polarized electrons incident on longitudinally and transversally polarized ammonia (NH_3) and deuterated ammonia (ND_3) targets. Polarized electrons were produced by photemission from a strained GaAs cathode that produced beam polarizations of 85%, measured using a Møller spectrometer with coincidence and single arm detectors. The polarized target operated in a 5 T magnetic field at 1 K. Average dynamic nuclear target polarizations (at 80 nA average beam current) of 60% for protons and 30% for deuterons have been attained. The scattered electrons were detected in two spectrometers placed at 4.5 ° and -7° with respect to the incident beam.The range of the kinematic scaling variables $x_{Bjorken}$ and momentum transfer Q^2 covered at 29.1 GeV is 0.03 to 0.76 for x_B and 1.25 GeV^2 to 9.7 GeV^2 for Q^2, for invariant masses W $>$ 2 GeV/c^2 in the deep inelastic region. The 29.1 GeV longitudinal data has been analyzed for protons and deuterons, and combined to extract the neutron structure. The results indicate that the extrapolated integrals of the structure functions Γ_1^p and Γ_1^d evaluated at the fixed $Q^2 = 3$ GeV^2 are not in agreement with the theoretical predictions by Ellis and Jaffe. The combined integral $\Gamma_1^p - \Gamma_1^n$ agrees with the Bjorken Sum Rule prediction when 3rd. order QCD corrections are included. The methods used to evaluate the structure functions at a common Q^2 are being further investigated.

*Supported in part by the Department of Energy, contract DE-FG0586ER40261
†Representing the E143 Collaboration: The American University, Institut für Physik der Universität Basel, 3LPC IN2P3/CNRS, University Blaise Pascal, CEBAF, DAPNIA-Service de Physique Nucleaire Centre d'Etudes de Saclay, Lawrence Livermore National Laboratory, University of Massachusetts, University of Michigan, Naval Postgraduate School, Old Dominion University, University of Pennsylvania, Stanford Linear Accelerator Center, Stanford University, Temple University, Tohoku University, University of Virginia, University of Wisconsin– R. Arnold and O. Rondon, spokesmen

1. Motivation

The so called "Proton Spin Crisis" began in 1988 with the publication of the measurements of the asymmetries observed in polarized muon-polarized nucleus scattering by the European Muon Collaboration at CERN.[7] This group found that the integral $\int_0^1 g_1^p(x)dx = 0.123 \pm 0.013 \pm 0.019$ of the experimental data fell short of the prediction $\int g_1^p(x)dx = 0.198 \pm 0.005$ for this sum rule formulated by Ellis and Jaffe[2] by more than four standard deviations. At the time this program of studies was proposed (December 1991), only the measurements of the spin asymmetries $A_1^p + \eta A_2^{p*}$ of the proton carried out at SLAC,[56] and the measurement of g_1 at CERN were available. While a variety of models of A_1 for the proton seemed to agree with all the experimental results in the range of the scaling variable $0.1 \leq x \leq 0.7$, the experimental uncertainties were large and the comparison with the theoretical predictions was inconclusive. On the other hand, in the range $0.01 \leq x \leq 0.1$, the EMC results lay below the predictions of all the models. These data, extrapolated to $x = 0$ led to the discrepancy with the sum rule: this was interpreted to mean that the strange sea and/or the gluons may be significantly polarized, and that the total fraction of spin carried by quarks may be small.

A related prediction for $\int_0^1 g_1^n(x, Q^2)dx$ for the neutron was also made by the same authors, under the same assumptions of SU(3) flavor symmetry and an unpolarized strange sea that were used for the proton. The importance of determining the true value of the proton integral and of the combined proton-minus-neutron integrals, also known as the Bjorken sum rule[1]

$$\int (g_1^p - g_1^n)dx = \frac{1}{6}\left|\frac{g_A}{g_V}\right|_{n\to pe^-\bar{\nu}}\left(1 - \frac{\alpha_s(Q^2)}{\pi}\right) \tag{1}$$

(shown with first order QCD corrections for finite Q^2) where g_A and g_V are the nucleon axial-vector and vector coupling constants, has been often asserted in the very extensive literature on this discrepancy that was generated in the years before experiment E143 was proposed at SLAC.

2. Review of cross sections and structure functions.

Before we proceed, a brief review of the foundations of the spin structure functions is useful. When longitudinally polarized leptons are incident on polarized nuclei one can compute the sum and the difference of the cross sections for two opposing orientations θ_N and $\theta_N + \pi$ of the nucleon spin. The results are that the sum is just twice the unpolarized cross section, while the difference,[34] is sensitive to the nucleon polarization. For $\theta_N = 0$ (i.e. longitudinally polarized leptons and nucleons) we get

$$\frac{d^2\sigma(0)}{d\Omega dE'} - \frac{d^2\sigma(\pi)}{d\Omega dE'} = \sigma^{\uparrow\uparrow} - \sigma^{\uparrow\downarrow} = \frac{4\alpha^2 E'}{Q^4 E}\Big((E + E'\cos\theta)MG_1 - Q^2 G_2\Big) \tag{2}$$

and for $\theta_N = \pi/2$ (longitudinal leptons and transverse nucleons) the result is

$$\frac{d^2\sigma(\pi/2)}{d\Omega dE'} - \frac{d^2\sigma(3\pi/2)}{d\Omega dE'} = \sigma^{\uparrow\rightarrow} - \sigma^{\uparrow\leftarrow} = \frac{4\alpha^2 E'}{Q^4 E}E'\sin\theta(MG_1 + 2EG_2) \tag{3}$$

*$\eta = 2QE'/(E - E')/(3E - E')$, E and E' are the initial and final lepton energies, Q^2 is the four-momentum transfer

where θ is the lepton scattering angle, Ω is the lepton detector solid angle, M is the nucleon mass, and $\nu = E - E'$ is the energy transfer. $G_1(Q^2,\nu)$ and $G_2(Q^2,\nu)$ are the spin structure functions. They can be related in the asymptotic limit to helicity distributions of the partons in the nucleon:

$$\lim_{Q^2,\nu\to\infty}(M\nu)MG_1(Q^2,\nu) = g_1(x), \qquad \lim_{Q^2,\nu\to\infty}(M\nu)\nu G_2(Q^2,\nu) = g_2(x). \tag{4}$$

In terms of the scaling structure functions, the cross section differences are:

$$g_1 - kg_2 \;=\; K(\sigma_A - \sigma_P) \;= K\Delta\sigma \tag{5}$$

for the longitudinal target spin orientation and

$$g_1 \;+\; k'g_2 \;=\; K'(\sigma'_A - \sigma'_P) \;=\; K'\Delta\sigma' \tag{6}$$

for the transversal one. k, k', K and$K'(E,E',\theta)$ are kinematic coefficients given in detail in the proposal.[9] The subscripts A AND P refer to the two opposite target configurations. The unprimed and primed symbols refer to the longitudinal and transversal configurations, respectively. These expressions can be solved for g_1, g_2. The result, which only involves quantities that are determined in the same experiment is:

$$g_1 = 2CE\big(\Delta\sigma + \tan(\theta/2)\Delta\sigma'\big) \tag{7}$$

$$g_2 = 2C(E-E')\Big(\frac{(E+E'\cos\theta)}{E'\sin\theta}\Delta\sigma' - \Delta\sigma\Big) \tag{8}$$

where C:

$$C = \frac{ME(E-E')\sin^2(\theta/2)}{2(E+E')\alpha^2}. \tag{9}$$

An Equivalent approach can be followed starting from the virtual photon absorption cross section for photon helicities $0, \pm 1$: $\sigma^T_{1/2}, \sigma^T_{3/2}, \sigma^{TL}_{1/2}$, from which the spin asymmetries A_1, A_2 are constructed:

$$A_1 = \frac{\sigma^T_{1/2} - \sigma^T_{3/2}}{\sigma^T_{1/2} + \sigma^T_{3/2}} = \frac{g_1 - (Q^2/\nu)g_2}{F_1} \tag{10}$$

$$A_2 = \frac{\sigma^{TL}}{\sigma^T} = \frac{(Q^2/\nu)(g_1+g_2)}{F_1} \tag{11}$$

This approach to g_1 involves the unpolarized structure function $F_1(x,Q^2)$.

The spin asymmetries are related to the measured asymmetries for the longitudinal and transversal configurations of the beam and target spins (known as $A||$ and $A_\perp$, $A = (\sigma^{\uparrow\uparrow} - \sigma^{\uparrow\downarrow})/(2\sigma)$) by expressions that involve kinematical factors, as well as the second unpolarized structure function $R(x,Q^2) = \sigma_L/\sigma_T$.

$$A_1 = \frac{c}{D}\big(A_{||} - dA_\perp\big) \tag{12}$$

$$A_2 = \frac{c}{D}\big(fA_{||} + d'A_\perp\big) \tag{13}$$

c, d, d' and f are kinematic coefficients, D is the virtual photon depolarization factor which is a function of R and the scaling variable $y = (E-E')/E$.

polarization/field direction combinations, and the measured asymmetries were consistent for the four data samples.

The scattered electrons were detected by a pair of non-focusing magnetic spectrometers, with their axes aligned at 4.5° and −7° with respect to the beam line, allowing a coverage in momentum transfer $1.3 < Q^2 < 10$ (GeV/c)^2 and a range $0.029 < x < 0.8$ for the scaling variable. These spectrometers are an improved version of the ones first used in the recent experiment E142.[19] Electrons were distinguished from a background of pions in each spectrometer using two threshold gas Čerenkov counters and a 24–radiation–length shower–counter array composed of 200 lead–glass blocks. Seven planes of plastic scintillator hodoscopes were used to measure particle momenta and scattering angles.

4. Data analysis and preliminary results.

4.1. The 29 GeV longitudinal data

A very large amount of data was accumulated during the long (November 1993 to February 6, 1994) data run. From this sample, we plan to extract the longitudinal spin structure functions for the proton, neutron and deuteron, in six different kinematic regions: 3 energies, two angles at each energy. The range of Q^2 covered in the experiment – for values of the invariant mass well above the nucleon resonances region – will allow studying the momentum transfer dependence of the structure functions over a decade of Q^2 change: ∼0.5 to ∼5 GeV^2, in the central region $0.07 \leq x \leq 0.2$. The 9.7 GeV data will allow the extraction of the structure function in the resonances region, at higher x. The transversal structure function will be extracted at one energy (29.1 GeV) for both nucleons.

At the time of writing this report, the proton longitudinal structure function has been extracted and the results are available in SLAC-Pub-6508. Deuteron results are also available but still in a provisional form. Both sets will be presented here. It must be mentioned that to obtain preliminary physics results in the shortest possible time, the analysis of the data has been carried out so far based only on the quick computation of cross section asymmetries instead of using the more reliable but lengthier cross section differences method.

The experimental asymmetries $A_{||}$ and $A_{\perp}$ are determined from

$$A_{(||\text{or}\perp)} = \left(\frac{L-R}{L+R}\right)\frac{C_N}{fP_bP_t} + C_R, \tag{14}$$

where the target polarization is parallel (transverse) to the beam direction for $A_{||}$ ($A_{\perp}$); L and R are the number of scattered electrons per incident charge for negative and positive beam helicity, respectively, normalized by charge and corrected for dead time and e^+-e^- pairs contamination; C_N is a correction factor for the polarized nitrogen nuclei; f is the dilution factor representing the fraction of measured events originating from polarizable nucleons within the target; P_b and P_t are the beam and target polarizations respectively; C_R is the radiative correction. The expression for the neutron asymmetry is

$$A_n = (1 + \frac{\sigma_p}{\sigma_n})\frac{A_d}{\gamma} - (\frac{\sigma_p}{\sigma_n})A_p \tag{15}$$

where σ_p/σ_n is extracted from deep inelastic scattering data. $\gamma \simeq 0.92$ is the effective polarization of the nucleons in the deuteron, correcting for those in the D-state.

The measured values of $A_{\|}$ and $A_{\perp}$ can be used in our previous equations for g_1 and g_2 with the substitution $\Delta\sigma = 2\sigma A$

$$g_1 = 2\sigma C E\Big(A_{\|} + (1 - \tan(\theta/2)A_{\perp}\Big) \tag{16}$$

$$g_2 = 2\sigma C(E - E')\left(\frac{(E + E'\cos\theta)}{E'\sin\theta}A_{\perp} - A_{\|}\right) \tag{17}$$

where σ is the usual unpolarized inclusive D.I.S. cross section, and C has been defined earlier. The values of A_1^p from this experiment[28] at $E = 29.1$ GeV are displayed in Fig. 1 along with results of previous experiments. Data from the two spectrometers are consistent in the overlap region $0.07 < x < 0.55$, and therefore have been averaged together.

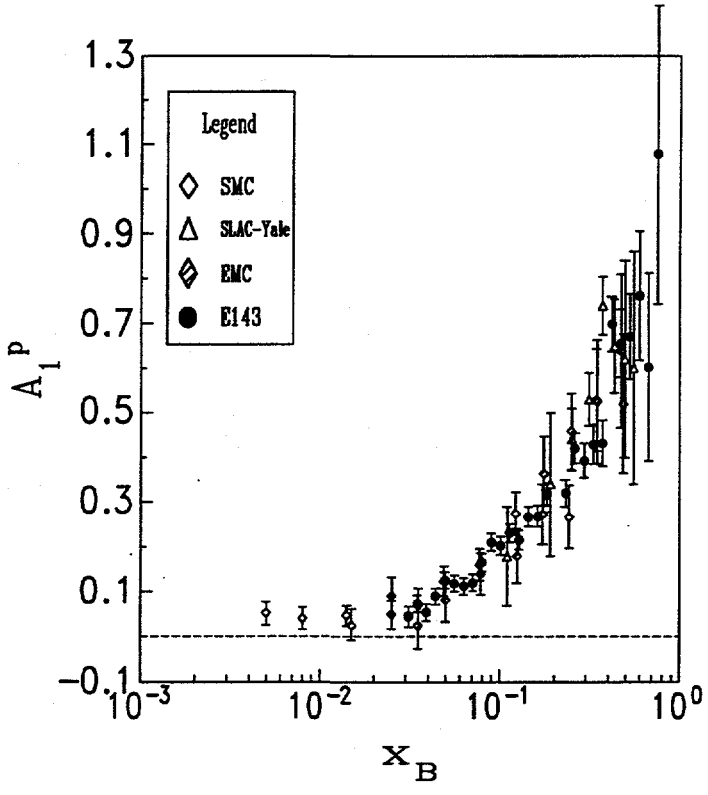

Fig. 1. The spin asymmetry A_1^p from all experiments, ploted at the measured x, Q^2

3. Experimental method.

A whole new generation of experiments designed to solve these problems has been developed, based on the availability of highly polarized electron beams at SLAC, and high polarization targets at SLAC and CERN. In the recent past the E142 collaboration at SLAC has measured the neutron spin structure function using a ^{3}He target[19] and the Spin Muon collaboration (SMC)[8] at CERN has measured g_1^p and g_1^d using butanol targets. The present experiment, E143, used the SLAC polarized electron beam with energies E of 9.7, 16.2, and 29.1 GeV scattering from polarized solid ammonia $^{15}NH_3$ and deuterated ammonia $^{15}ND_3$ targets in SLAC's End Station A (ESA) to measure g_1^p, g_2^p, g_1^d, and g_2^d.

The longitudinally polarized electron beam was produced by photoemission from a strained-lattice GaAs crystal illuminated by a flash-lamp-pumped Ti-sapphire laser operated at 850 nm.[21] Beam pulses were typically 2 μsec long, contained 2–4$\times 10^9$ electrons, and were delivered at a rate of 120 Hz. The helicity was selected randomly on a pulse-to-pulse basis to minimize instrumental asymmetries. The longitudinal beam polarization P_b was measured in the End Station A using Møller scattering. Two independent detector systems were used, one to detect just one of the final-state electrons, the other to detect both of them in coincidence. The average beam polarization was 0.85 ± 0.02. A clear dependence of the polarization on the quantum efficiency of the photocathode was observed.

Due to target operation considerations, the beam currrent was limited to < 100 nA, and the beam was rastered over the front surface of the target to spread the heating and radiation damage as uniformly as possible. The beam current was measured for each beam pulse by two independent toroid systems with an uncertainty of $< 1\%$. Asymmetries induced by changes in beam parameters correlated with helicity were found to be negligible.

The polarized target assembly contained two 3–cm–long target cells that could be selected individually by remote control. The permeable target cells were immersed in a vessel filled with liquid He and maintained at 1 K by use of a high power evaporation refrigerator. The first (top) cell was filled with granules of $^{15}ND_3$ (98% isotopic purity), and the second cell contained $^{15}NH_3$ (99.7% isotopic purity). A superconducting Helmholtz coil provided a uniform field of 4.8 T in the active target volume.

The ammonia granules during the experiment were exposed to 138 GHz microwaves to drive the hyperfine transition which aligns the nucleon spins. This technique of dynamic nuclear polarization produced proton polarizations of 65 to 80% in the NH_3 target and deuteron polarizations of 30%. The heating of the target by the beam caused a drop of a few percent in the polarization. The polarization then slowly decreased due to radiation damage. Most of the radiation damage was repaired by annealing the target at about 80 K, until the accumulated dose reached $> 2 \times 10^{17}$ electrons. The luminosity of the polarized material in the uniform field region was 80×10^{33} cm^{-2} Hz.

As part of the program to minimize the sources of systematic errors, the target polarization direction was usually reversed after each anneal by adjusting the microwave frequency. Also, the direction of the magnetic field was reversed several times during the experiment. Approximately equal amounts of data were taken in each of the four

It can be seen in Fig. 1 that both the previous SLAC data[6] and the higher Q^2 EMC and SMC data[8] ($< Q^2 >= 10$ (GeV/c)^2) are in agreement with this experiment, indicating that to a good approximation, A_1 is independent of Q^2 over the (x, Q^2) range where this ratio has been measured.

In Fig. 2, on the other hand, we show the preliminary results for the deuteron structure function measured in E143, plotted alongside the SMC 1992 results.

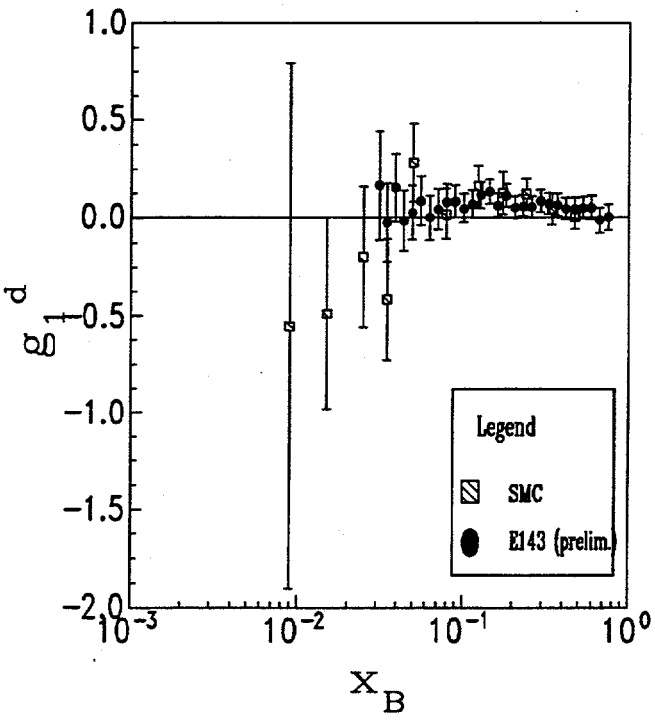

Fig. 2. The spin structure function g_1^d for SLAC's E143 and CERN's SMC, plotted at the measured x, Q^2

Figure 3, displays the preliminary results for the neutron structure function measured in E143, plotted alongside the SLAC E142 published results.

There are two options to convert the structure functions from x, Q^2 dependent quantitites to functions of x only:

• Use the data in the full range of kinematics measured in E143 to interpolate or extrapolate to a common Q^2. This is the plan for the remainder of the data analysis, including those taken at 16 and 9.7 GeV.

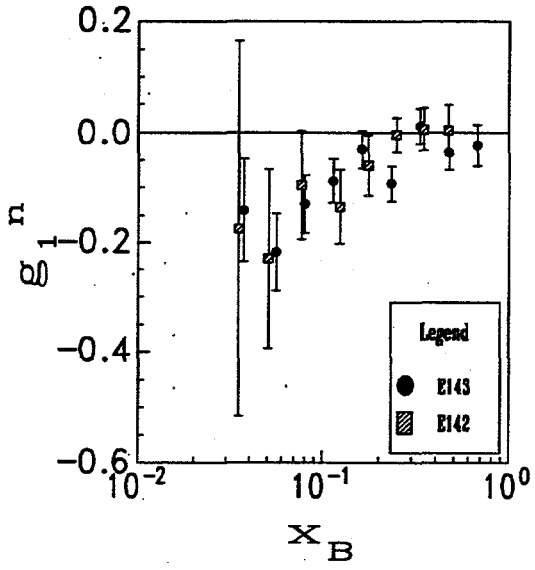

Fig. 3. The spin structure function g_1^n for SLAC's E143 and E142, plotted at the measured x, Q^2

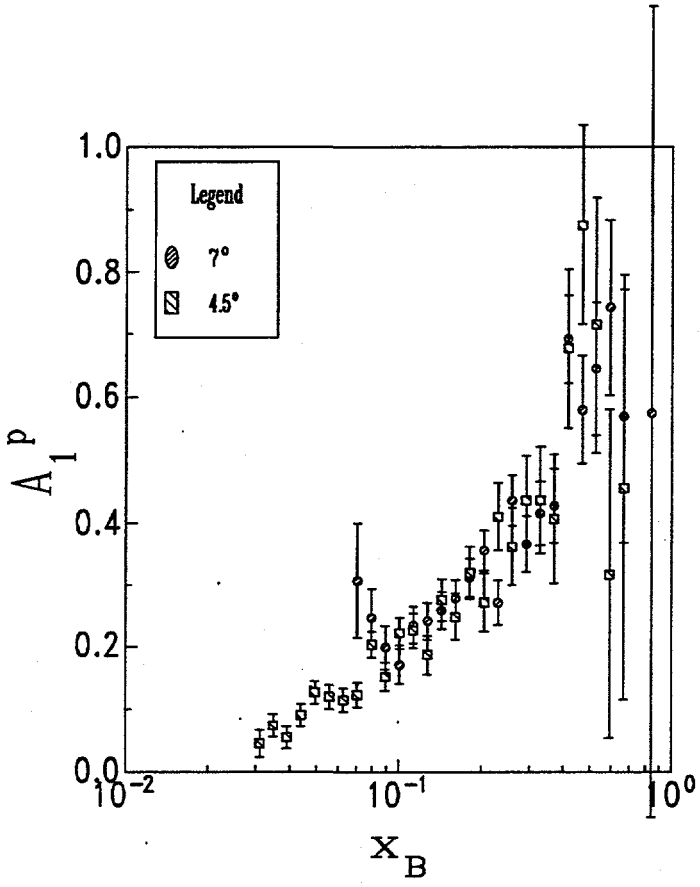

Fig. 4. The spin asymmetry A_1^p for the 4.5° and 7° spectrometers for the 29.1 GeV data of E143 plotted at the measured x, Q^2, displaying Q^2independence.

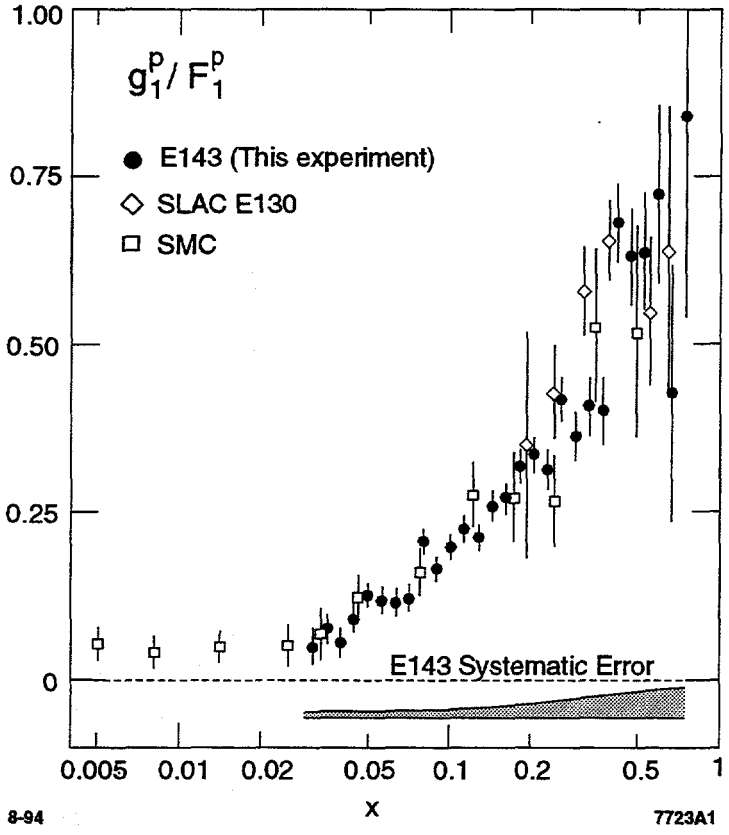

Fig. 1

Fig. 5. The g_1/F_1 ratio from E143, SMC and SLAC's E130, covering a range of Q^2that changes by a factor of > 5 at any given x. The errors are statistical only. Systematic errors are indicated by the lower band.

• Make some assumptions from the observed Q^2 dependence of the 29.1 GeV g_1 data for the two spectrometer angles, combined with preliminary values for the 16.1 GeV data. This is the current choice.

Two different assumptions have been used to try to interpolate (or extrapolate) the spin structure functions from the (x, Q^2) kinematic points at which they have been measured to a common set of kinematics (x, $Q_0{}^2 = 3$ GeV^2). The first method starts with the expression for g_1 :

$$g_1 = F_1 \frac{A_1 + \gamma A_2}{(1+\gamma^2)} \tag{18}$$

where the factor $\gamma = Q/\nu$ is a kinematic coefficient. It has been observed that for the Q^2 range of the 29 GeV data A_1, A_2 are independent of Q^2 so that if one computes F_1 (x, Q_0^2=3GeV^2) and uses γ evaluated at the same momentum transfer, one would obtain $g_1(x,Q_0^2$=3GeV^2), which in turn can be used to compute sum rules at constant Q^2. Since the F_1 structure function is not readily available, it is replaced by the non-perturbative version of the Callan-Gross relation

$$F_1 = F_2 \frac{(1+\gamma^2)}{2x(1+R)} \tag{19}$$

The $(1+\gamma^2)$ factor cancels in the substitution, so in the end we have

$$g_1 = F_2 \frac{A_1 + \gamma A_2}{2x(1+R)} \tag{20}$$

with all quantities either constant or evaluated at a fixed Q^2.

An alternative method g_1 has been proposed by Peter Bosted, which starting from expressions 16 and 17, in an additional step, the unpolarized cross section for D.I.S. is expressed in terms of the unpolarized structure functions F_1 and R:

$$g_1' = F_1 \frac{A_{\|} + A_{\perp} \tan(\theta/2)}{D'} \tag{21}$$

where D' is a factor akin to the depolarization factor D, that depends on kinematics and R. This is equivalent to substituting for the spin asymmetries A_1 and A_2 their original forms in terms of $A\|$ and $A_\perp$ and doing the algebra. The 29 and 16 GeV data when analyzed in terms of the g_1/F_1 ratio obtained from the preceding equation displays independence of the momentum transfer: g_1' at constant Q^2 could be computed by multiplying this ratio by F_1 (x, Q^2=3GeV^2), as in the first method.
The two g_1 and g_1' are related by a kinematical transformation

$$\frac{g_1}{g_1'} = \left[\frac{A_1 + \gamma(Q_0^2)A_2}{A_1 + \gamma(Q^2)A_2}\right]\left[\frac{1+\gamma^2(Q^2)}{1+\gamma^2(Q_0^2)}\right] \tag{22}$$

Figures 4 and 5 show that indeed both A_1 and g_1/F_1 appear to be independent of Q^2. A_2 adds a very small contribution, further suppressed by γ. In Fig. 4, we plot the 29.1 GeV data from E143 separately for each spectrometer. Figure 5 shows the E143 data

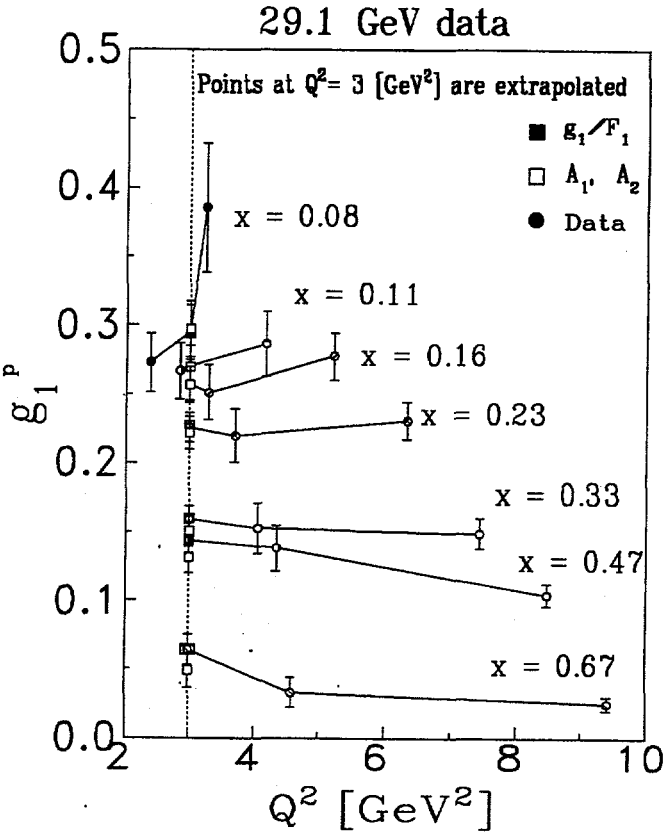

Fig. 6. The 29.1 g_1^p data for E143 plotted together with the extrapolations based on the two assumptions discussed in the text.

alongside the SMC data and the older SLAC E130 data which are plotted assuming $A_\perp = 0$ (that experiment measured $A_\parallel$ only). The SMC data are plotted assuming $g_1/F_1 \approx A_1$, which is a good approximation at their beam energy of 190 GeV. For $F_1^p = (1+\gamma^2)F_2^p/[2x(1+R)]$ we used the NMC fit[30] to F_2^p and the SLAC fit[27] to R. Using the SLAC global fit[31] to F_2^p gives similar results. In Fig. 5 we also show systematic errors, that include contributions from P_b, P_t, f and C_R, as well as 3 to 5% in D' arising from the uncertainty in R and an x-dependent error on the ratio F_1^p/F_1^d which varies from 2.5% in the mid-x range to 4% at the low x and 10% at high x.

Figure 6. displays the relation between the two assumptions and the data: the points plotted at Q^2= 3 GeV^2 are the result of the extrapolations, which mostly agree with the data within the limits of the errors. For this plot the data have been grouped in wider x bins, to improve the statistical uncertainty. The lines are ploted to guide the eye. It is clear that a better understanding of the Q^2dependence will be obtained from the analysis in terms of absolute cross sections, which is planned for the next stage.

4.2. Extrapolations to $x = 0$ and $x = 1$

The extrapolation from $x = 0.8$ to $x = 1$ was done assuming g_1 is proportional to $(1-x)^3$ at high x[36]; this yields $\int_{0.8}^1 g_1^p(x)dx = 0.001 \pm 0.001$. The extrapolation to $x = 0$ is more model dependent, and could be large if g_1^p were to increase strongly at low x. We studied the x-dependence of g_1^p using our data combined with SMC and EMC data. We observe that, consistent with Regge theory,[12] all data for $x < x_{max} = 0.1$ are fitted well (χ^2/d.f.=0.9) by a constant value of $g_1^p = 0.29 \pm 0.02$ at $Q^2 = 3$ (GeV/c)^2 (see curve on Fig. 7). We use this value to estimate $\int_0^{0.029} g_1^p(x)dx = 0.006 \pm 0.006$. A related fit $g_1 \propto 1/log(x)$ was also tried, agreeing with the Regge fit within 1 standard deviation.

Values of xg_1^p at the average $Q^2 = 3$ (GeV/c)^2 of this experiment are shown in Fig. 7.

4.3. Integrals and sum rules

The integral of g_1^p over the measured range $0.029 < x < 0.8$ is proportional to the area under the data points in Fig. 7, yielding $\int_{0.029}^{0.8} g_1^p(x)dx = 0.120 \pm 0.004 \pm 0.008$, where the first error is statistical, and the second is systematic. Given the two assumptions that g_1/F_1 depends only on x and that g_1^p is constant at low x, we obtain the total integral $\Gamma_1^p = \int_0^1 g_1^p(x)dx = 0.127 \pm 0.004 \pm 0.010$. This is in good agreement with the value from SMC,[8] $\Gamma_1^p = 0.122 \pm 0.011 \pm 0.011$, obtained at $Q^2 = 3$ (GeV/c)^2 assuming $g_1/F_1 \approx A_1$ is independent of Q^2. Our result is more than two standard deviations below the Ellis-Jaffe sum rule prediction of 0.160 ± 0.006, evaluated using the QCD corrections of Ref.[33] with $\alpha_s = 0.35 \pm 0.05$[34] $Q^2 = 3$ (GeV/c)^2.

The spin structure functions in the parton model are interpreted as helicity densities of the different quark flavors:

$$g_1 = \frac{1}{2}\sum_i e_i^2[q_i^\uparrow(x) - q_i^\downarrow(x)], \qquad i = u, \bar{u}, d, \bar{d}, s, \bar{s}, ... \tag{23}$$

Then, the integral of the structure function is

$$\Gamma_1^p = \frac{1}{2}\sum_i e_i^2 \int_0^1 [q_i^\uparrow(x) + q_i^\downarrow(x)]dx = \frac{1}{2}\sum_i e_i^2 \Delta q_i \tag{24}$$

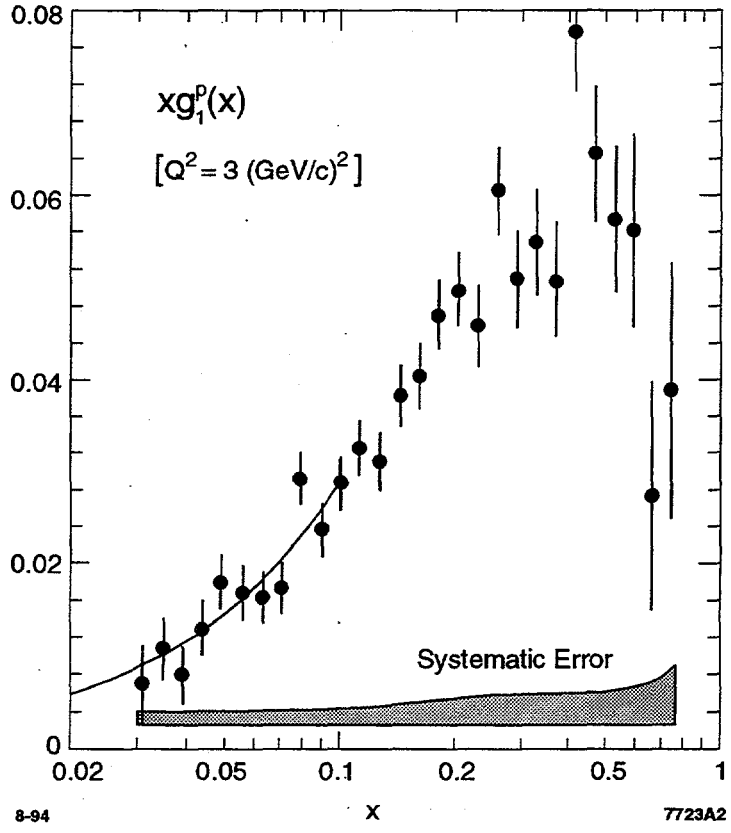

Fig. 2

Fig. 7. The structure function g_1^p (scaled by x) from this experiment evaluated at fixed Q^2=3 $(GeV/c)^2$. The systematic errors are indicated by the lower band. The curve is given by g_1 =0.29, the value used for the low–x extrapolation.

For the proton one has

$$\Gamma_1^p = \frac{1}{2}\left(\frac{4}{9}\Delta u + \frac{1}{9}\Delta d + \frac{1}{9}\Delta s\right) \tag{25}$$

for three quark flavors. For the neutron one has:

$$\Gamma_1^n = \frac{1}{2}\left(\frac{4}{9}\Delta d + \frac{1}{9}\Delta u + \frac{1}{9}\Delta s\right) \tag{26}$$

These relations hold true in the asymptotic limit, where the structure functions depend only on x. At finite Q^2, the expressions are modified by QCD corrections, as mentioned above.

We can use the quark-parton model, the ratio of axial-vector to vector coupling constants and the SU(3) coupling constants $F = 0.459 \pm 0.008$ and $D = 0.798 \pm 0.008$[35] to extract the total quark helicity contribution $\Delta\Sigma = \Delta u + \Delta d + \Delta s = 0.29 \pm 0.10$, which is small compared to the Ellis-Jaffe prediction $3F - D \approx 0.58$ for $\Delta s = 0$. We can use our value of $\Delta\Sigma$ along with the definition $3F - D = \Delta\Sigma - 3\Delta s$ to extract the strange quark contribution $\Delta s = -0.10 \pm 0.04$, which is negative and inconsistent with zero.

A more accurate determination of $\Delta\Sigma$ can be obtained from the deuteron integral (still a preliminary value) $\Gamma_1^d = \int_0^1 g_1^d(x)dx = 0.043 \pm 0.004 \pm 0.004$, since only the combination $3F - D$ is needed as external input. The input to the deuteron integral is the spin structure function g_1^d, which has been extracted in a very similar fashion as the proton's. The integral in the measured range is $\int_{0.029}^{0.8} g_1^d(x)dx = 0.041 \pm 0.004 \pm 0.004$. The extrapolations to $x = 1$ and to $x = 0$ have been estimated in the same way as for the proton. Their contributions are small, 0.002 ± 0.001 for the low x end, and 0.000 ± 0.001 for high x. The resulting QCD corrected total quark helicity, including the uncertainties in α_s and F and D, is $\Delta\Sigma = 0.331 \pm 0.052$, which is the world's best value for this quantity. The neutron integral is

$$\Gamma_1^n = \frac{2}{1 - 1.5w_D}\Gamma_1^d - \Gamma_1^p = -0.33 \pm 0.010 \pm 0.011 \tag{27}$$

where the w_D factor takes into account the D-state of the deuteron.

For $Q^2 = 3$ (GeV/c)^2 and for three flavors, the Bjorken sum rule prediction with third order QCD corrections[32] is $\Gamma_1^{p-n} = \Gamma_1^p - \Gamma_1^n = \frac{1}{6}(g_A/g_V)(1 - \alpha_s(Q^2)/\pi - 3.58(\alpha_s(Q^2)/\pi)^2 - 20.22(\alpha_s(Q^2)/\pi)^3) = 0.171 \pm 0.008$, Using our deuteron data and the extrapolation based on the Q^2 independence of g_1/F_1 we obtain $\Gamma_1^{p-n} = 0.160 \pm 0.011 \pm 0.017$, which is consistent with the prediction within errors. Using the extrapolation based on the Q^2 independence of A_1 and A_2 we obtain $\Gamma_1^{p-n} = 0.154 \pm 0.011 \pm 0.017$, again compatible with the theory.

Finally, combining our results for Γ_1^p with the SLAC E142[19] determination of Γ_1^n we obtain $\Gamma_1^{p-n} = 0.149 \pm 0.014$.

APPENDIX

The virtual photon depolarization factor is (exactly)

$$D = \frac{y(2-y)(1+Q^2y/(2\nu^2)}{(1+(Q/\nu)^2)[y^2+2(1-y-(yQ/2/\nu)^2)(1+R)/(1+(Q/\nu)^2)]} \cdot \qquad (28)$$

where $y = E - E'/E$ and R is the ratio σ_L/σ_T.

References

1. J. D. Bjorken, Phys. Rev. **148**, 1467 (1966); Phys. Rev. D **1**, 1376 (1970).
2. J. Ellis and R. Jaffe, Phys. Rev. D **9**, 1444 (1974); D **10**, 1669 (1974).
3. C. E. Carlson and Wu-Ki Tung, Phys. Rev. **D5** (1972)721
4. A. J. G. Hey and J. E. Mandula, Phys. Rev. **D5** (1972)2610
5. SLAC E80, M. J. Alguard *et al.,* Phys. Rev. Lett. **37**, 1261 (1976); **41**, 70 (1978).
6. SLAC E130, G. Baum *et al.,* Phys. Rev. Lett. **51**, 1135 (1983).
7. EMC, J. Ashman *et al.,* Phys. Lett. **B206**, 364 (1988); Nucl. Phys. **B328**, 1 (1989).
8. SMC, D. Adams *et al.,*, Phys. Lett. **B329**, 399 (1994).
9. E143 Collaboration (R.G. Arnold *et al.*), *Measurement of the Nucleon Spin Structure at SLAC in End Station A*, SLAC-Proposal-E-143, SLAC, December 1991.
10. E. Leader and M. Anselmino, Z. Phys. **C41**(1988)239
11. W. Wandzura and F. Wilczek, Phys. Lett. **B172** (1977)195
12. R. L. Heimann, Nucl. Phys. **B64** (1973)429
13. R. L. Jaffe and Xiangdong Ji, Phys. Rev. **D43** (1991)726
14. V. M. Belyaev and B. L. Ioffe, Int. J. Mod. Phys. **A6** (1991)1533
15. K. Hidaka, E. Monsay and D. Sivers, Phys. Rev. **D19** (1979)1503
16. E. Richter-Was, Acta Phys. Pol. **B16** (1985)739
17. R. P. Feynman, *Photon-Hadron Interactions* (Benjamin, New York, 1972)
18. H. Burkhardt and W. N. Cottingham, Ann. Phys. (N.Y.) **56** (1970)453
19. SLAC E142, P. L. Anthony *et al.,* Phys. Rev. Lett. **71**, 959 (1993).
20. SMC, B. Adeva *et al.,* Phys. Lett. **B302**, 533 (1993).
21. T. Maruyama, E. L. Garwin, R. Prepost, G. H. Zapalac, Phys. Rev. B **46**, 4261 (1992); R. Alley *et al.,* Report No. SLAC–PUB–6489 (1994).
22. D. G. Crabb *et al.,* Phys. Rev. Lett. **64**, 2627 (1990); W. Meyer *et al.,* Nucl. Instrum. Meth. **215**, 65 (1983).
23. G. R. Court *et al.,* Nucl. Instrum. Meth. **A324**, 433 (1993).
24. G. G. Petratos *et al.,* Report No. SLAC–PUB–5678 (1991).
25. T. V. Kukhto and N. M. Shumeiko, Nucl. Phys. **B219**, 412 (1983); I. V. Akusevich and N. M. Shumeiko, J. Phys. G **20**, 513 (1994).
26. Y. S. Tsai, Report No. SLAC–PUB–848, 1971; Y. S. Tsai, Rev. Mod. Phys. **46**, 815 (1974).
27. L. W. Whitlow *et al.,* Phys. Lett. **B250**, 193 (1990).
28. Tables corresponding to Fig. 1 and Fig. 2 available in SLAC E143, K. Abe *et al.,* Report No. SLAC–PUB–6508 (1994).
29. G. Altarelli, P. Nason, and G. Ridolfi, Phys. Lett. **B320**, 152 (1994).
30. NMC, P. Amaudruz *et al.,* Phys. Lett. **B295**, 159 (1992).
31. L. W. Whitlow *et al.,* Phys. Lett. **B282**, 475 (1992).
32. S. A. Larin and J. A. M. Vermaseren, Phys. Lett. **B259**, 345 (1991) and references therein.
33. S. A. Larin, Report No. CERN–TH.7208/94.

34. M. Schmelling and R. D. St.Denis, Report No. CERN/PPE93–193; S. Nerison, Report No. CERN–TH.7188/94.
35. for example F. E. Close and R. G. Roberts, Phys. Lett. **B316**, 165 (1993); J. Ellis and M. Karliner, Phys. Lett. **B313**, 131 (1993).
36. S.J. Brodsky, M. Burkardt and I. Schmidt, report No. SLAC-PUB-6087 (1994)

Spin Dependent Scattering and the Quark Content of Nucleons

A. Manohar
University of California, San Diego

SUMMARY

Recent experiments have begun to probe the detailed spin and flavor structure of hadrons. The status of the g_1 structure function and its implications for the polarized strange quark sea will be discussed, as well as what we hope to learn about hadronic structure from spin dependent measurements that will be carried out over the next few years.

PHYSICS OF Q^2-DEPENDENCE IN THE NUCLEON'S $G_1(x,Q^2)$ STRUCTURE FUNCTION SUM RULE

Xiangdong Ji*†

Center for Theoretical Physics
Laboratory for Nuclear Science
and Department of Physics
Massachusetts Institute of Technology
Cambridge, Massachusetts 02139 U.S.A.

ABSTRACT

I discuss in this talk the physics of the Q^2 dependence of the $G_1(x,Q^2)$ structure function sum rule. For $Q^2 > 3$ GeV^2, the Q^2 variation is controlled by pure QCD radiative corrections. For $0.5 < Q^2 < 3$ GeV^2, the twist-four contribution becomes significant, but stays perturbative. For Q^2 below ~ 0.05, the sum rule is determined by low-energy theorems. The rapid change of the sum rule between 0.05 and 0.5 GeV^2 signals the transition between parton and hadron degrees of freedom.

In polarized electron or muon scattering on a polarized nucleon target, one measures the nucleon tensor,

$$W_{\mu\nu} = \frac{1}{2}\sum_n (2\pi)^3 \delta^4(P+q-P_n) \times \langle PS|J_\mu(0)|n\rangle\langle n|J_\nu(0)|PS\rangle \ , \quad (1)$$

where $|PS\rangle$ is the ground state of the nucleon with momentum P^μ and polarization S^μ, $|n\rangle$ are the excited states of the nucleon after absorbing the virtual photon of momentum q^μ, and J_μ is the usual electromagnetic current of the nucleon, which are composed of quark fields. The spin-dependent part of the tensor is known to depend on two Lorentz scalar structure functions $G_1(Q^2,\nu)$ and $G_2(Q^2,\nu)$,

$$W_{\mu\nu}|_{\text{spin-depen.}} = -i\epsilon_{\mu\nu\alpha\beta}q^\alpha \left(\frac{G_1}{M^2}S^\beta + \frac{G_2}{M^4}\left(S^\beta \nu M - P^\beta (S\cdot q)\right)\right) \quad (2)$$

where $Q^2 = -q^2$ and $\nu M = P\cdot q$.

*This work is supported in part by funds provided by the U.S. Department of Energy (D.O.E.) under cooperative agreement #DF-FC02-94ER40818.

†Talk presented at the Workshop on Spin Degrees of Freedom in Electromagnetic Nuclear Physics APS/DNP fall meeting, Williamsburg, Virginia, 1994.

Although we shall not always work in the Bjorken limit, it turns out convenient to replace variable ν by x: $x = Q^2/2M\nu$. The drawback of doing this is that the whole photo-production region shrinks to a point $x = 0$ and $Q^2 = 0$. However, for our purpose it is not a problem. I assume from now on that $G_1(Q^2, x)$ is measured to a good precision in low and intermediate Q^2 regions. This may turn out to be the biggest assumption of my talk. I certainly hope this can be done in the future at CEBAF and other places.

Two interesting sum rules exist for G_1 at large and small Q^2, respectively. The deep-inelastic sum rule is defined at $Q^2 \to \infty$ limit,

$$\begin{aligned} \Gamma &= \lim_{Q^2\to\infty} \int_0^1 g_1(x, Q^2)dx \ , \\ &= \frac{1}{2}\sum_i e_i^2 \Delta q_i \ , \end{aligned} \tag{3}$$

where $g_1(x, Q^2) = (\nu/M)G_1(\nu, Q^2)$ is the scaling function and Δq_i is the axial charge for quark flavor i, which is defined by,

$$\langle PS|\bar{\psi}_i \gamma_\mu \gamma_5 \psi_i|PS\rangle = 2\Delta q_i S_\mu \ . \tag{4}$$

The Bjorken sum rule relates $\Gamma^p - \Gamma^n$ to the neutron β-decay constant g_A[1] and Ellis-Jaffe sum rules refer to a model prediction for Γ^p and Γ^n made by Ellis and Jaffe.[2]

The Drell-Hearn-Gerasimov (DHG) sum rule is a sum rule for $G_1(\nu, Q^2)$ at the real photon point $Q^2 = 0$.[3] For simplicity of discussion, I view the sum rule as the limit of $Q^2 \to 0$,

$$\lim_{Q^2\to 0} \int_{\nu_{\rm in}}^\infty \frac{d\nu}{\nu} G_1(\nu, Q^2) = -\frac{1}{4}\kappa^2 \ , \tag{5}$$

where $\nu_{\rm in}$ is the inelastic threshold and κ is the anomalous magnetic moment of the nucleon. Using the scaling function, I can write,

$$\int_0^1 dx g_1(x, Q^2)^{\rm inelastic} = -\frac{\kappa^2}{8}\frac{Q^2}{M^2} + \mathcal{O}\left(\left(\frac{Q^2}{M^2}\right)^2\right) , \tag{6}$$

for small Q^2. The question I want to address below is what physics controls the variation of the sum rule between the large and small Q^2 limits.

First let me consider deep-inelastic sum rules at large but finite Q^2. There are two types of QCD corrections to the $Q^2 \to \infty$ limit. The first is the QCD radiative corrections shown in Fig. 1(a), which take into account the effects of hard gluons in the hard process. The second is the higher-twist corrections shown in Fig. 1(b), which are basically initial and final state interactions between the active quark and the remnants of the target. For example, the Bjorken sum rule with these corrections reads,

$$\int_0^1 g_1^{p-n}(x, Q^2)dx = \frac{g_A}{6}\left(1 - \frac{\alpha_s(Q^2)}{\pi} - \cdots\right) + \frac{\mu_4^{p-n}(Q^2)}{Q^2} + \cdots \tag{7}$$

where the terms in the bracket represent radiative effects and μ_4^{p-n} is the nucleon matrix elements of some twist-two, three, and four operators.[4]

A number of comments can be made about the sum rule in Eq. (7):

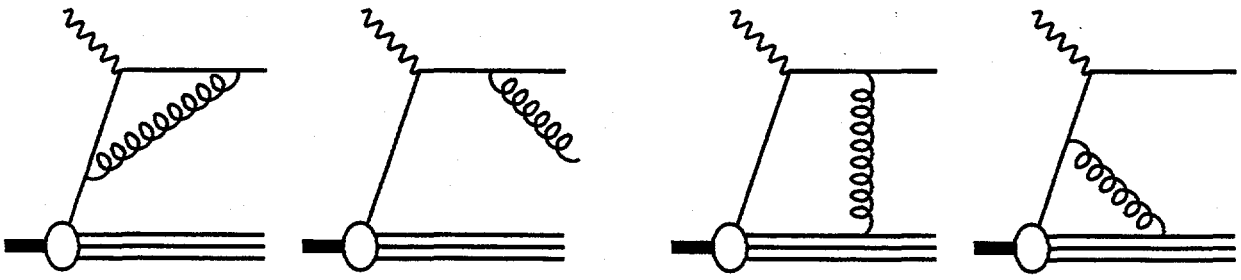

Fig. 1. a). QCD radiative corrections to deep-inelastic scattering. b). Higher-twist corrections to deep-inelastic scattering.

- Theoretically there is an ambiguity in separating out contributions of different twists. This was first recognized by A. Mueller.[5] The problem is that the perturbative series for radiative corrections is not convergent. It is a non-Borel-summable series. Thus the result obtained by Ellis and Karliner by comparing the data with the four-loop prediction should be taken with a grain of salt, particularly at low Q^2.[6] I have recently outlined a solution to the problem,[7] but I cannot talk about it here due to time limitation.

- The sum rule *must* include the elastic contribution as it becomes important below $Q^2 = 2$ GeV^2. The reason is obvious: the sum rule is derived from operator product expansion and one gets an operator product only when all intermediate states are summed over. If one is still not convinced, consider the nucleon is a point-like particle, then the only contribution to the sum rule is elastic scattering.[8] For the nucleon, the elastic contribution to Γ is,

$$\Gamma^{\text{elastic}} = \frac{1}{2}F_1(F_1+F_2) - \frac{1}{8M^2}F_2^2Q^2 \ . \tag{8}$$

  where F_1 and F_2 are the usual Dirac and Pauli form factors.

- Higher-twist contributions have been estimated in the MIT bag model[4] and in QCD sum rule approach,[9]

$$\begin{aligned} \mu_4^{p-n} &= 0.031M^2 \ , \qquad \text{(Bag)} \\ \mu_4^{p-n} &= -0.023M^2 \ . \qquad \text{(QSR)} \end{aligned} \tag{9}$$

  Here the infrared renormalon problem has been ignored. The two estimates differ in sign. This shows that we are not yet confident in calculating higher-twist matrix elements. However, it is quite clear that the size of the higher-twist contribution is small. It contributes at 10% level at $Q^2 = 2$ GeV^2, and becomes negligible at $Q^2 = 10$ GeV^2.

The above discussion shows that $\Gamma(Q^2)$ *changes very little from* $Q^2 = \infty$ *down to* $Q^2 = 0.5\ GeV^2$. Radiative effects are on the order of 10% to 20% in the entire region. The twist-four effects are important only in the range $Q^2 \sim 0.5 - 3$ GeV^2. Again, their contribution is not overwhelming.

Now let me turn to the sum rule at $Q^2 \sim 0$. The DHG sum rule certainly needs to be tested. Its validity tells us whether there is a subtraction constant in the dispersion relation, whether the sum rule is convergent, and whether there are fixed pole contributions, etc. The detailed mechanism for sum rule saturation is also interesting. In particular, there are indications that the Δ excitation exhausts major part of the sum rule.

One can generalizes the DHG sum rule to small Q^2 by writing a low energy expansion,

$$\int_0^1 dx g_1(x,Q^2)^{\text{inelastic}} = -\frac{\kappa^2}{8}\frac{Q^2}{M^2} + \alpha\left(\frac{Q^2}{M^2}\right)^2 + \cdots \tag{10}$$

where α is a parameter which can be calculated for instance in chiral perturbation theory. It is also interesting to test this type of generalized sum rule.

One interesting question is how to connect the DHG sum rule to the deep-inelastic sum rule. This question is first studied by Anselmino, Ioffe, and Leader,[10] and the result has been quoted by many authors. Unfortunately, their study is wrong. They neglected the elastic contribution when interpolating high and low Q^2 sum rules and thus got the incorrect conclusion that Γ_p/Q^2 has to change sign at some intermediate Q^2. The sign change was considered as mysterious. As I said before, as Q^2 decreases, the high Q^2 side physics is controlled by twist expansion which, by definition, contains the elastic contribution.

Once the elastic contribution is included, we have at low Q^2,

$$\begin{aligned}\Gamma_p(Q^2) &= \Gamma_p(Q^2)^{\text{elastic}} + \Gamma_p(Q^2)^{\text{inelastic}} \\ &= 1.396 - 8.631Q^2 + \alpha Q^4 + \cdots \end{aligned} \tag{11}$$

According to the above, $\Gamma_p(Q^2 \to 0) \to 1.396$, which is much larger than $\Gamma_p(Q^2 = 10\ \text{GeV}^2) = 0.136$. Clearly, $\Gamma_p(Q^2)$ drops very quickly as Q^2 increases due to the large coefficient of the Q^2 term. In fact, if one neglects the higher order terms, $\Gamma_p(Q^2)$ drops to the level at $Q^2 = 10\ \text{GeV}^2$ when $Q^2 = 0.15\ \text{GeV}^2$. This behavior is certainly consistent with the small higher-twist effects at moderate Q^2. However, beyond that, the $Q^2 \sim 0$ behavior says nothing about the size of higher twist effects, contrary to many claims in the literature.

Certainly, the change between $Q^2 \sim 0.05$ and $Q^2 = 0.5$ is interesting. We do not have reliable theoretical prediction in the region. However, we believe that the transition between hadronic and partonic description of scattering occurs in this region. Since the transition is likely smooth, I think nothing drastic happens for $\Gamma_p(Q^2)$ other than a smooth connection between low and high Q^2 limits.

To summarize the above discussion, the physics of Q^2 variation of $\Gamma_p(Q^2)$ can be roughly divided into four regions. For $Q^2 > 3\ \text{GeV}^2$, the Q^2 variation is controlled by QCD radiative corrections. In $0.5 < Q^2 < 3\ \text{GeV}^2$, the twist-four contribution is important. Below $\sim 0.05\ \text{GeV}^2$, the Q^2 variation is determined by low energy theorems. In $0.05 < Q^2 < 0.5\ \text{GeV}^2$, parton-hadron transition happens. A rough sketch for the sum rule variation (the solid line) is shown in Fig. 2. The dotted line represents an extrapolation from high energy and the dash-dotted line an extrapolation from low energy.

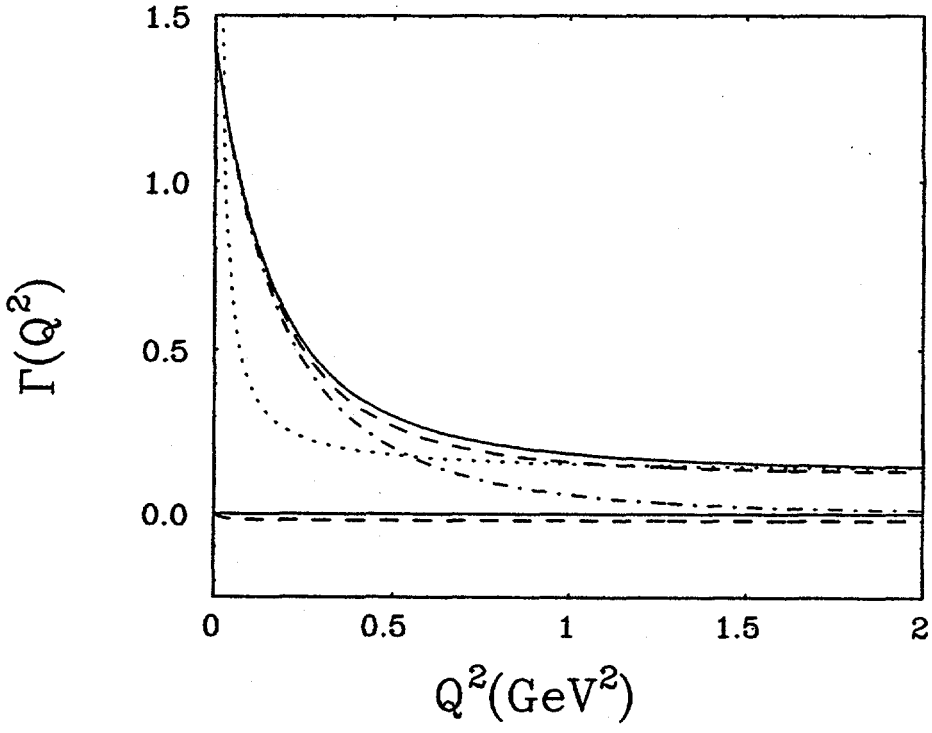

Fig. 2. Schematic Q^2-dependent of the first moment of G_1 structure function.

Let me emphasize the importance of getting data in the region $0.5 < Q^2 < 3$ GeV^2. The sum rule here can be constructed with future resonance data from CEBAF and low x data from SLAC or HERMES. It allows one to extract the matrix element f,

$$\langle PS|g\bar{\psi}\tilde{F}^{\mu\nu}\gamma_\nu\psi|PS\rangle = 2fS^\mu \ . \tag{12}$$

f is very interesting from the nucleon's structure point of view. In fact, the sign of f determines roughly whether the color magnetic field **B** in the polarized nucleon is pointing to the direction of the spin or opposite.

Thus one can learn a lot of physics by measuring the first moment of the G_1 structure function at low and intermediate Q^2. I urge experimenters go ahead to take some good data on G_1.

References

1. J. Bjorken, *Phys. Rev.* **148** (1966) 1467.
2. J. Ellis and R. L. Jaffe, *Phys. Rev.* **D9** (1974) 1444.
3. S. D. Drell and A. C. Hearn, *Phys. Rev. Lett.* **16** (1966) 908; S. B. Gerasimov, *Sov. J. Nucl. Phys.* **2** (1966) 430.
4. X. Ji and P. Unrau, *Phys. Letts.* **B333** (1994) 228.
5. A. H. Mueller, *Phys. Letts.* **B308** (1993) 355.
6. J. Ellis and M. Karliner, CERN-TH 7324/94.
7. X. Ji, MIT CTP-preprint No. 2381 (1994).

8. X. Ji, *Phys. Lett.* **B309** (1993) 187.
9. I. I. Balitsky, V. M. Braun, and A. V. Kolesnichenko, *Phys. Letts.* **B242** (1990) 245; **B318** (1993) 648.
10. M. Anselmino, B. L. Ioffe and E. Leader, *Sov. J. Nucl. Phys.* **49** (1989) 136.

ELECTROMAGNETIC SPIN STRUCTURE RESPONSE OF NUCLEONS IN NUCLEI

JOHN MICHAEL FINN
Department of Physics
The College of William and Mary in Virginia
Williamsburg, VA 23187

ABSTRACT

Complete characterization of the electromagnetic nuclear current in $(\vec{e}, e'\vec{N})$ reactions require a decomposition of the virtual photon spin-density-matrix coupled with measurements of initial- and final-state spin polarizations. Theoretical analysis reveals a wealth of information with different amplitudes demonstrating quite different sensitivities to the various ingredients of the reaction mechanism. Recent technological advances including development of polarized targets and recoil-polarimeters have made a first generation of experiments possible. Much of the initial effort has been directed at extracting G_{En} from *(e,e'n)* experiments on deuterium and ^{3}He targets. The quasifree assumption underlying these experiments can itself be put to a rigorous test by performing the analogous *(e,e'p)* experiments. Beyond these measurements, a complete study of these elementary systems is expected to greatly enhance our understanding of two- and three-body currents which is vital for the construction of the short-range nuclear force. Scattering from single-particle orbits in complex nuclear systems provides a convenient spin-isospin filter. This can be used to study selected components of the effective interaction, providing complimentary information to on-going hadron scattering experiments. At the higher Q^2 of the CEBAF laboratory, one can expect that complex systems will also be used as a laboratory to study the composition and propagation of nucleons in nuclear matter. For example, polarization transfer in quasifree knockout of protons from the nuclear interior can be examined to determine if the effective G_E/G_M ratio varies from that of the free proton. One can also examine those amplitudes that vanish in the impulse approximation to see if there is a systematic weakening of the FSI at high Q^2, which might be a precursor for the onset of color transparency. The maturing of these spin physics methods promises an exciting decade for electromagnetic nuclear physics.

1. Introduction

The advent of high duty-factor electron accelerators makes coincidence electron scattering experiments a practical vehicle for probing nuclear structure. The virtues of the electromagnetic probe have been well documented. The interaction is weak enough that the one-photon-exchange (OPE) approximation is generally valid, but not so weak as to prevent precision measurements. Furthermore the electron propagator and vertex can be described accurately in the framework of quantum electrodynamics (QED). The nuclear response is given in terms of its electromagnetic transition current, a well-defined quantity from a fundamental theoretical perspective. In the context of quantum chromodynamics or QCD, this coupling is directly to the system's quark degrees of freedom (the gluonic

degrees of freedom are electromagnetically neutral). Therefore, electron scattering provides a direct measure of the quark substructure of the nucleus. From a more conventional viewpoint this coupling can be described in terms of a multi-particle scattering series involving effective nucleon and meson degrees of freedom. By suitable choice of kinematics, one can couple directly to the nucleonic degrees of freedom present in the initial state. Quasifree knockout, for example, predominantly probes the single-particle orbitals that comprise the nuclear ground state in the shell model picture. As kinematics are varied one can enhance other aspects of the reaction process, allowing one to explore two-body and many-body contributions to the nuclear current. Of particular interest to present day theory is exploring the connection between the quark-gluon and nucleon-meson pictures. One hopes to understand how hadrons are formed and propagate in the nuclear medium and how they interact at short distances.

In preparing for a new generation of electromagnetic nuclear physics experiments, it is also clear that measurements of spin degrees of freedom will play an increasingly vital role in understanding this fascinating and complex state of matter. The techniques to effectively carry a program of coincidence (e,e'N) spin physics experiments have only recently been developed. Only a handful of measurements are underway or completed. Most have focused on the extraction of the neutron's electric form factor, with the remainder dealing primarily with resonance excitations. These elementary systems will be subject of other talks in this conference; I will concentrate on presenting a description of the more general physics issues involving polarization measurements of nucleons in nuclei.

Present techniques involve the use of polarized targets and/or recoil polarization measurements. In some cases the two techniques compete. For example either the $\vec{d}(\vec{e},e'n)p$ or the $d(\vec{e},e'\vec{n})p$ reaction can be used to measure the neutron's electric form factor and both are actively being pursued at CEBAF.[1] In the more general case, however, the two methodologies are complimentary. Both are required to completely separate the electromagnetic spin current of nuclear systems. For example, the reactions $^3\vec{H}e(\vec{e},e'p)$ and $^3He(\vec{e},e'\vec{p})$ are very different. The recoil polarization reaction can easily be calculated in the impulse approximation and leads to sizable polarizations. The target polarization asymmetry, on the other hand, vanishes if

Figure 1: Expected asymmetries in the $^3\vec{H}e(\vec{e},e'p)T$ reaction using the BLAST detector in the Bates SHR at $\vec{q}$ = 0.4·GeV.[2] The solid (dashed) line is for parallel (perpendicular) target spin. Projected errors for 1000·hr of beam time are shown.

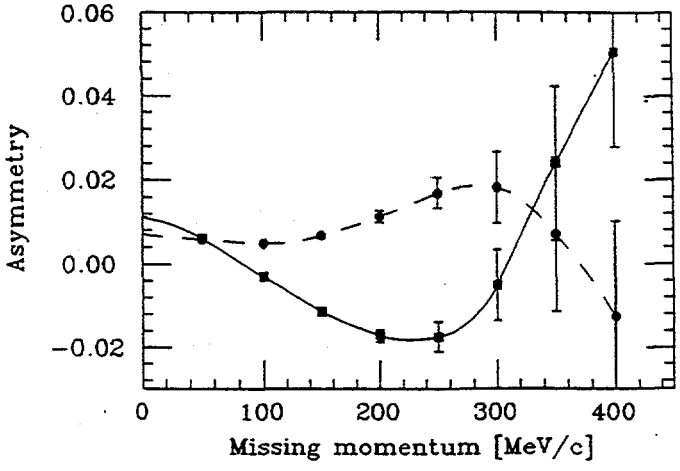

one ignores the small components of the nuclear wave function. This is because the spin of ^{3}He is carried primarily by the neutron. Two protons in a relative s-state couple to spin zero.

The BLAST collaboration has suggested using an internal polarized ^{3}He gas jet target in the storage ring at Bates as one means of measuring these small d-state components of the wave function.[2] Figure 1 shows that the expected asymmetries are small and that it will take about 1000·hours to carry out such measurements at Bates given an expected luminosity of $\approx 10^{-32} \cdot cm^2 \cdot s^{-1}$. Low luminosity is the primary problem with current polarized target technology and only a few nuclear isotopes have been successfully polarized. Recoil polarimetry is the more generally applicable technology. It's primary limit is the low figure-of-merit of focal plane polarimeters, typically about 10^{-2}. In this talk I will primarily describe the methodology of recoil polarimetry, bringing in target polarimetry as appropriate for comparative purposes.

2. Some General Considerations

Figure 2: (e,e'p) scattering kinematics.

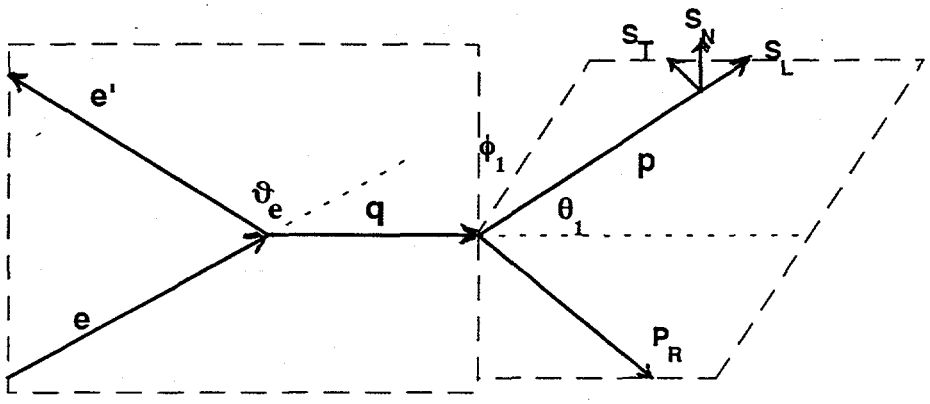

Figure 2 shows the generic kinematics for coincidence *(e,e'p)* scattering experiments. The 3-momentum transfer to the hadronic system, ***q=(e-e')*** lies in the *(e,e')* scattering plane. The reaction pane is defined by the vectors ***p*** and ***q***. The missing momentum $\boldsymbol{P_R}$ also lies in this pane. A spherical basis is used to define the proton direction, where θ_1 is the polar angle between ***p*** and ***q***, while ϕ_1 is the asymuthal angle between the two planes. The proton's spin vector is referenced to the hadronic reaction plane, with longitudinal spin typically defined to lay along the proton's velocity axis, transverse spin is in the reaction plane and perpendicular to longitudinal spin, and normal spin is perpendicular to the reaction plane. Because the proton's spin vector is defined in a coordinate frame that is rotating with respect to the laboratory, there are implicit dependencies on ϕ_1 in addition to those explicitly shown in the standard formalisms. Therefore caution must be used when determining the spin symmetry rules in the laboratory frame.

One-Photon Exchange Approximation

In the OPE approximation, the 4-momentum transfer q is also the virtual photon's 4-momentum. The virtual photon is a spin-1 particle in a mixed spin state. The relative weights of transverse and longitudinal spin depends on the electron's scattering angle ϑ_e The reaction is self-analyzing with respect to the ϕ_1 dependence of the coincidence reaction. One measure of the photon spin state is given by the longitudinal polarization ε_L

$$\varepsilon_L = \frac{1}{1+2\frac{\vec{q}^2}{Q^2}\tan^2\frac{\vartheta_e}{2}} \leq 1 \,. \tag{2.1}$$

(letting $Q^2 = -q^2$). The invariant cross section for coincidence (e,e'p) reactions to a continuum final state is given by

$$d\sigma = \frac{m_e M_A}{\sqrt{(k_e \cdot P_A)^2 - (m_e M_A)^2}} \cdot \|M\|^2_{continuum} \cdot \frac{m_e d\vec{e}'}{e'_0} \cdot \frac{m_p d\vec{p}}{p_0} \,, \tag{2.2}$$

where $\|M\|^2$ is the invariant transition matrix element. For scattering to a discrete final state the following replacement is made:

$$\|M\|^2_{continuum} \rightarrow \|M\|^2_{discrete} \cdot 2M_R \delta\left((P_A + q - p)^2 - {M_R}^2\right). \tag{2.3}$$

In the OPE approximation the electron and hadron tensors factorize:

$$\|M\|^2_{OPE} = \frac{4\alpha^2}{q^4} \eta_{\mu\nu} \cdot W^{\mu\nu} \,, \tag{2.4}$$

where η is the electron's electromagnetic transition tensor, which completely describes the virtual photon's polarization state. In the extreme relativistic limit, for longitudinally polarized electrons with helicity h, it is given by

$$\eta_{\mu\nu} = \frac{1}{2m_e^2}\left\{e_\mu e'_\nu + e'_\mu e_\nu + \frac{q^2}{2}\delta_{\mu\nu} + ih\varepsilon_{\mu\nu\alpha\beta} e^\alpha e'^\beta\right\}. \tag{2.5}$$

W is the hadronic transition tensor given by the bilinear form:

$$W^{\mu\nu} = J^{\mu^*} J^\nu \,, \tag{2.6}$$

where J is the nuclear electromagnetic transition current.

Spin formalism

The formalism for scattering by a longitudinally polarized electron beam and detecting the knockout-proton polarization is given by

$$\|M\|^2 = \|M_0\|^2 \cdot \left(1 + hA + \vec{P}\cdot\hat{S} + hD^{Li}\hat{S}_i\right) \,, \tag{2.7}$$

where $\|M_0\|^2$ is the spin-averaged matrix element, A is the scattering asymmetry, P is the induced-polarization vector and D is the polarization-transfer matrix. The nuclear response can be further reduced in the laboratory frame by decomposition in terms of various photon polarization weights v_i and nuclear response functions $R\,i$. Using the notation of Picklesimer and Van Orden,[3] the cross section can be written as

$$\frac{d^3\sigma}{d\omega\, d\Omega_e d\Omega_p} = \frac{m_p|\vec{p}|}{2(2\pi)^3}\left[\frac{d\sigma}{d\Omega}\right]_{mott} \times \Big\{ v_L\left(R_L + R_L^N S_N\right) + v_T\left(R_T + R_T^N S_N\right)$$
$$+ v_{TT}\left[\left(R_{TT} + R_{TT}^N S_N\right)\cos 2\varphi + \left(R_{TT}^L S_L + R_{TT}^T S_T\right)\sin 2\varphi\right]$$
$$+ v_{LT}\left[\left(R_{LT} + R_{LT}^N S_N\right)\cos\varphi + \left(R_{LT}^L S_L + R_{LT}^T S_T\right)\sin\varphi\right] \qquad (2.8)$$
$$+ h v_{LT'}\left[\left(R_{LT'} + R_{LT'}^N S_N\right)\sin\varphi + \left(R_{LT'}^L S_L + R_{LT'}^T S_T\right)\cos\varphi\right]$$
$$+ h v_{TT'}\left[R_{TT'}^L S_L + R_{TT'}^T S_T\right]\Big\}$$

where $\varphi=\phi_1$, and

$$v_L = \frac{Q^4}{\vec{q}^4} \qquad v_T = \frac{Q^2}{2\vec{q}^2} + \tan^2\frac{\vartheta_e}{2}$$
$$v_{TT} = \frac{Q^2}{2\vec{q}^2} \qquad v_{LT} = \frac{Q^2}{\vec{q}^2}\sqrt{\frac{Q^2}{\vec{q}^2} + \tan^2\frac{\vartheta_e}{2}} \qquad (2.9)$$
$$v_{LT'} = \frac{Q^2}{\vec{q}^2}\tan\frac{\vartheta_e}{2} \qquad v_{TT'} = \tan\tfrac{\vartheta_e}{2}\sqrt{\frac{Q^2}{\vec{q}^2} + \tan^2\frac{\vartheta_e}{2}}$$

Careful examination reveals that the helicity-dependent asymmetry A vanishes in co-planar kinematics ($\varphi=0,\pi$). Only the components $D_{LT'}$, D_{LL} and P_N survive. They can be written as

$$P^N(\varphi = 0,\pi) = I_0^{-1}\left[v_L R_L^N + v_T R_T^N + v_{TT} R_{TT}^N \cos 2\varphi + v_{LT} R_{LT}^N \cos\varphi\right]$$
$$D^{LL}(\varphi = 0,\pi) = I_0^{-1}\left[v_{TT'} R_{TT'}^L + v_{LT'} R_{LT'}^L \cos\varphi\right] \qquad (2.10)$$
$$D^{LT}(\varphi = 0,\pi) = I_0^{-1}\left[v_{TT'} R_{TT'}^T + v_{LT'} R_{LT'}^T \cos\varphi\right]$$
$$I_0(\varphi = 0,\pi) = \left[v_L R_L + v_T R_T + v_{TT} R_{TT} \cos 2\varphi + v_{LT} R_{LT} \cos\varphi\right]$$

By using spin precesion of the protons in a the magnetic spectrometer and by flipping the electron's helicity, all three components can be simultaneously measured in a recoil polarimeter. By also making measurements for both values of $\varphi=(0,\pi)$, 7 of the 9 in-plane polarization response functions can be completely separated.

In elastic proton scattering only the D_{LL} and D_{LT} terms survive. The experimental results depend only on a single ratio g_p of the two Sach's form factors, $G_{E,M}$:

$$D_{LL} = \frac{e_0 + e_0'}{m_p}\sqrt{\tau(1+\tau)}\tan^2\left(\tfrac{\theta_e}{2}\right) \Big/ \left[g_p{}^2 + \tau(1 + 2(1+\tau)\tan^2\left(\tfrac{\theta_e}{2}\right)\right] \qquad (2.11)$$
$$D_{LT} = -2g_p\sqrt{\tau(1+\tau)}\tan\left(\tfrac{\theta_e}{2}\right) \Big/ \left[g_p{}^2 + \tau(1 + 2(1+\tau)\tan^2\left(\tfrac{\theta_e}{2}\right)\right] \quad ,$$

where $\tau = Q^2/4m_p^2$ and $g_p=G_E/G_M$:.

3. Experimental Considerations

Figure 3 shows a typical *(e,e'p)* scattering arrangement. For illustrative purposes, the two 4·GeV HRS[2] spectrometers in CEBAF's Hall A are shown.

Figure 3: Plan view of the high resolution Hall A spectrometer pair.

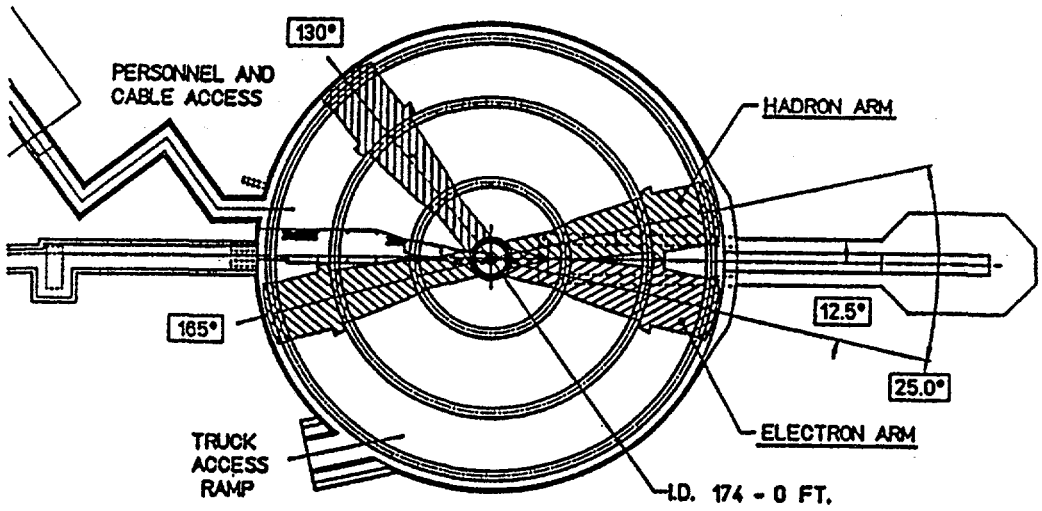

Figure 4: The focal plane instrumentation package for the HRS hadron spectrometer.

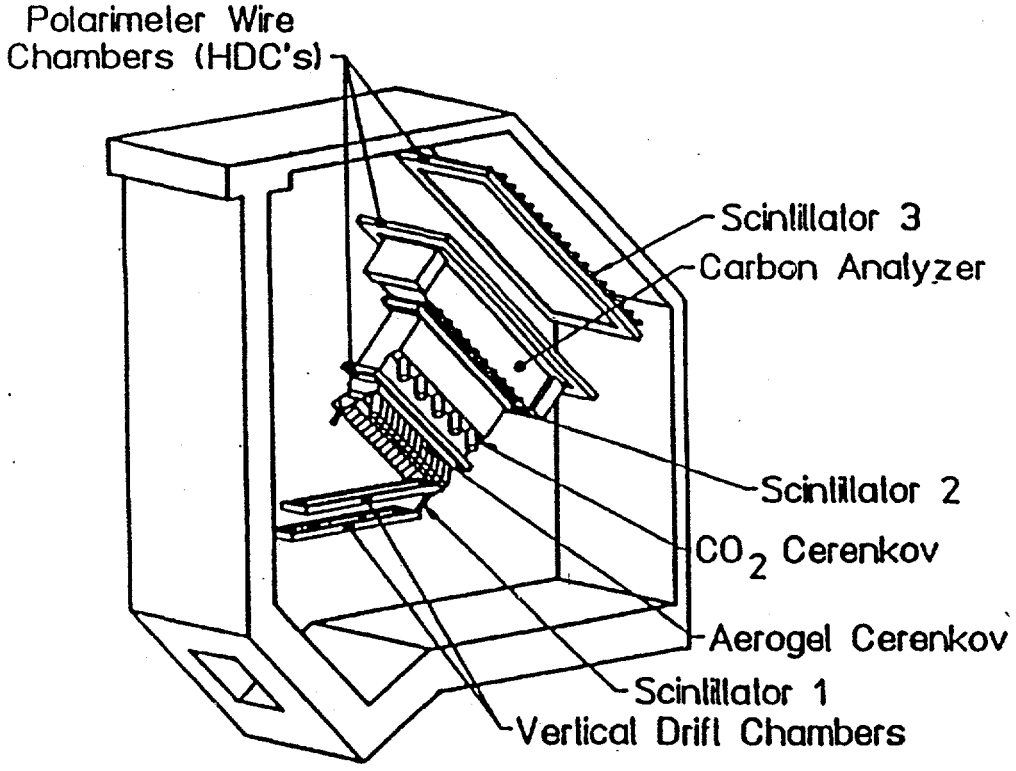

These spectrometers have a 10·mstr solid angle, a 45° bend angle and a 25·M flight path to the focal plane. For polarized target experiments, the scattering chamber can be adapted to meet the special requirements of the target. The hadron spectrometer in Hall A has a recoil proton Focal Plane Polarimeter (FPP) installed as part of its standard instrumentation package. This is illustrated in Figure 4.

Recoil Polarization Measurements

Proton spin precession in the magnetic spectrometer rotates the proton's spin orientation by an angle χ, given by

$$\chi = \gamma\left(\frac{g_s - 2}{2}\right)\Omega_B, \tag{3.1}$$

where γ is the Lorentz factor, g_s is the proton's gyromagnetic ratio ($\approx$5.586) and Ω_B is the spectrometer bend angle. For co-planar experiments using a vertical bending spectrometer, the normal and longitudinal spin components precess as follows:

$$\begin{aligned} p'_x &= P_N \cos\chi + hD_{LL}\sin\chi \\ p'_y &= hD_{LT} \\ p'_z &= -P_N \sin\chi + hD_{LL}\cos\chi \end{aligned} \tag{3.2}$$

where p'_i denotes components of the polarization vector at the detector package. The **x** and **y** components of this vector can be measured by performing a second scattering measurement. Denoting the polar angle of the second scattering by θ_2 and the asymuthal angle by ϕ_2, the distribution of second scattering events can be written as

$$\begin{aligned} N(\varphi_2) &= N_0 f\left\{1 + \langle A_y(\theta_2)\rangle\left[p'_x\cos\phi_2 + p'_y\sin\phi_2\right]\right\} \\ &= N_0 f\left\{1 + \langle A_y(\theta_2)\rangle\left[\left(P_N\cos\chi + hD_{LL}\sin\chi\right)\cos\phi_2 + hD_{LT}\sin\phi_2\right]\right\} \end{aligned} \tag{3.3}$$

where N_0 is the total number of events entering the spectrometer, f is the fraction of events that scatter into a useful angular range and $\langle A_y \rangle$ is the angle-averaged analyzing power of the polarimeter. The three spin components can be extracted by simultaneously flipping the beam helicity and performing a Fourier analysis on the results .

Figure 5: Spin transfer coefficients for the proton at Q^2=1·GeV^2, using $g_p=1/\mu_p$.

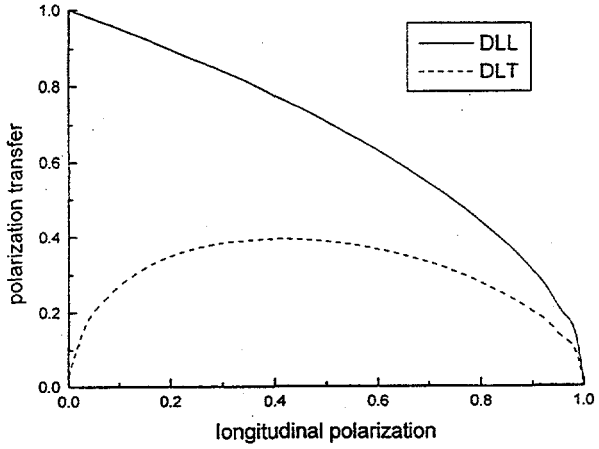

The figure of merit for the polarimeter is FOM=$f\langle A_y\rangle^2$. Typically it is about 10^{-2}. The statistical uncertainty in the measured polarization is given by

$$\Delta p' = \frac{\pi}{2\langle A_y\rangle}\sqrt{\frac{1}{fN_0}}\,. \tag{3.4}$$

The polarimeter can be calibrated, in-place, by performing elastic proton scattering and measuring both D_{LT} and D_{LL}. The ratio of the two polarizations gives g_p directly:

$$\frac{D_{LT}}{D_{LL}} = \frac{p'_y \sin\chi}{p'_x}\bigg|_{ep} = \frac{-2m_p}{(e_0 + e'_0)\tan(\vartheta_e/2)} g_p \qquad (3.5)$$

Figure 5 shows how D_{LX} varies for the proton as a function of the longitudinal photon polarization for fixed Q^2=1·GeV^2. Although the polarization-transfer coefficients go to zero for small electron scattering angles, this is a little misleading since the cross section is strongly peaked at forward scattering angles. Optimizing the kinematics for polarization measurements requires realistic averaging over spectrometer acceptances. This can be achieved by using a precision Monte Carlo code such as MCEEP[4] which has been optimized for coincidence *(e,e' p)* measurements.

4. The Spectator Model

The spectator model (Figure 6) is essentially the impulse approximation. The photon couples to the detected nucleon, putting it on its mass shell, and the residual nucleus simply recoils. The nuclear matrix is given by the product of the half-on-mass-shell nucleon transition element multiplied by the occupation probability of the initial proton having a momentum $p^*=(p-q)=-P_R$. The binding energy of the initial state is given by $\varepsilon_B = M_R + m_p - M_A$. The spectator model is most likely to be appropriate for quasielastic scattering kinematics, $(\omega = (e-e')_0 \approx Q^2/2m_p)$ or $(x \approx 1)$.

Figure 6: The spectator model.

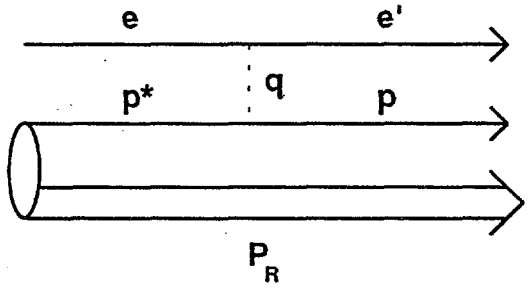

In this approximation the nuclear transition tensor factorizes. Treating the proton as a Dirac spinor gives

$$W^{\mu\nu} = \frac{1}{8m_p^2} \cdot Trace\left\{\left(\not{p}^* + m_p\right)\Gamma^\mu\left(\not{p} + m_p\right)\left(1 + i\not{\hat{S}}\gamma_5\right)\Gamma^\nu\right\} \cdot \left|\Phi\left(\vec{P}_R\right)\right|^2 \qquad (4.1)$$

where

$$\Gamma_\mu = \left(\gamma_\mu - \frac{\not{q} q_\mu}{q^2}\right) F_1\left(q^2, m^*\right) + \frac{i}{4m_p}\left[\gamma_\mu, \not{q}\right] F_2\left(q^2, m^*\right), \qquad (4.2)$$

$\hat{S}$ is the proton spin vector $(p \cdot \hat{S} = 0)$ and $\left|\Phi\left(\vec{P}_R\right)\right|^2$ is the scalar occupation probability normalized to

$$\oint \frac{M_R}{E_R} d\vec{P}_R \left|\Phi(\vec{P}_R)\right|^2 = N_{occupation}. \qquad (4.3)$$

It should be noted, however, that the definition given above for the single nucleon current operator is neither complete nor unique. Because the initial proton is off-mass-shell, some prescription is needed to completely define the electromagnetic current operator. The one normally used is to replace the half-off-shell Dirac and Pauli form factors with their on-mass-shell values:[5]

$$F_i(q^2, m^*) \rightarrow F_i(q^2, m) = F_i(q^2) \tag{4.4}$$

As the recoil momentum increases the nucleon goes further off-shell:

$$\frac{m_p{}^2 - m^{*2}}{2m_p} = \frac{\left(m_p^2 - \left(m_p - \varepsilon_B\right)^2\right) + 2T_R M_A}{2m_p} \approx \varepsilon_B + \frac{\vec{P}_R^2}{2m_p}\frac{M_A}{M_R} \tag{4.5}$$

Relativistic effects are particularly pronounced in the two body breakup of deuterium. Recent experiments at NIKHEF[6] at $Q^2 = 0.2 \cdot GeV^2$ and at SLAC[7] at $1.2 \cdot GeV^2$ have measured unpolarized the in-plane scattering asymmetry $A\phi$ which is proportional to R_{LT}:

$$A_\phi = \frac{\sigma(\phi = 0) - \sigma(\phi = \pi)}{\sigma(\phi = 0) + \sigma(\phi = \pi)} = \frac{v_{LT} R_{LT}}{v_L R_L + v_T R_T + v_{TT} R_{TT}}. \tag{4.6}$$

In both experiments there is clear preference for the relativistic treatments. Figure 7 shows the results of the SLAC experiment compared to various relativistic and non-relativistic calculations. Arenhövel[8] and Mosconi[9] have determined that most of the relativistic effect resides in the current operator, *i.e.*, keeping the higher powers of q/M removes most of the discrepancy.[10]

Figure 7: Aϕ asymmetry in *d(e,e'p)* as measured at SLAC and compared to various non-relativistic and relativistic calculations (from ref. 10). The shaded band on the SLAC data indicated the systematic error band.

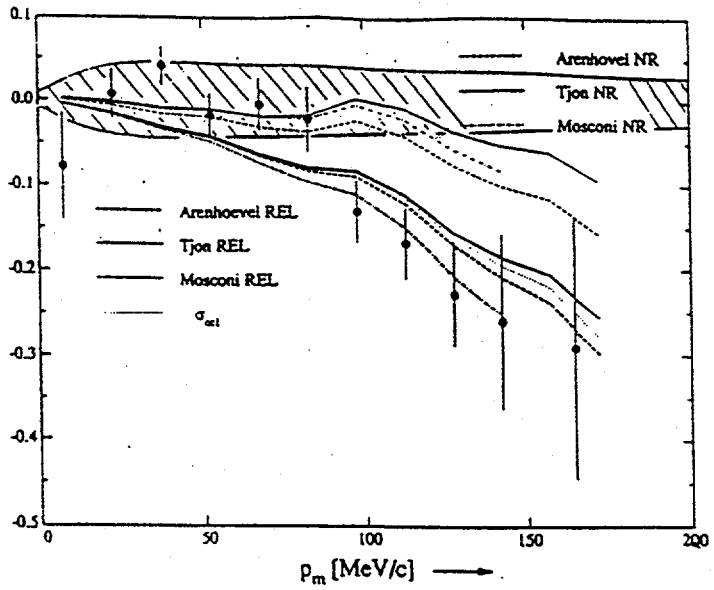

If one wishes to explore the issue of how nucleons are modified by the medium as opposed to kinematic off-shell effects, it is best to make the measurements at low recoil

momentum where the kinematical uncertainties of the prescription are the smallest. A good system for studying medium modifications is ^{4}He which has four nucleons in a relative s-state. The central density of ^{4}He is also quite high, about half that of nuclear matter. The Q^2 dependence of the $^4He(e,e'p)^3H$ reaction can shed light on the issue of nucleon swelling in the medium. Furthermore, the ratio $g^*_p=G^*_E/G^*_M$ can be tested to see how it differs from the free proton value. This is the motivation of a polarization-transfer proposal by Ent *et al.*[11] Calculations by Laget for this proposal are shown in Figure 8. In the absence of nucleon modifications, little difference from the impulse approximation is expected at low momentum.

Figure 8: Polarization observables in the ^{4}He(e,e'p)T reaction.[11] The dashed curve is the PWIA prediction, the solid curve is the complete calculation including MEC and IC effects.

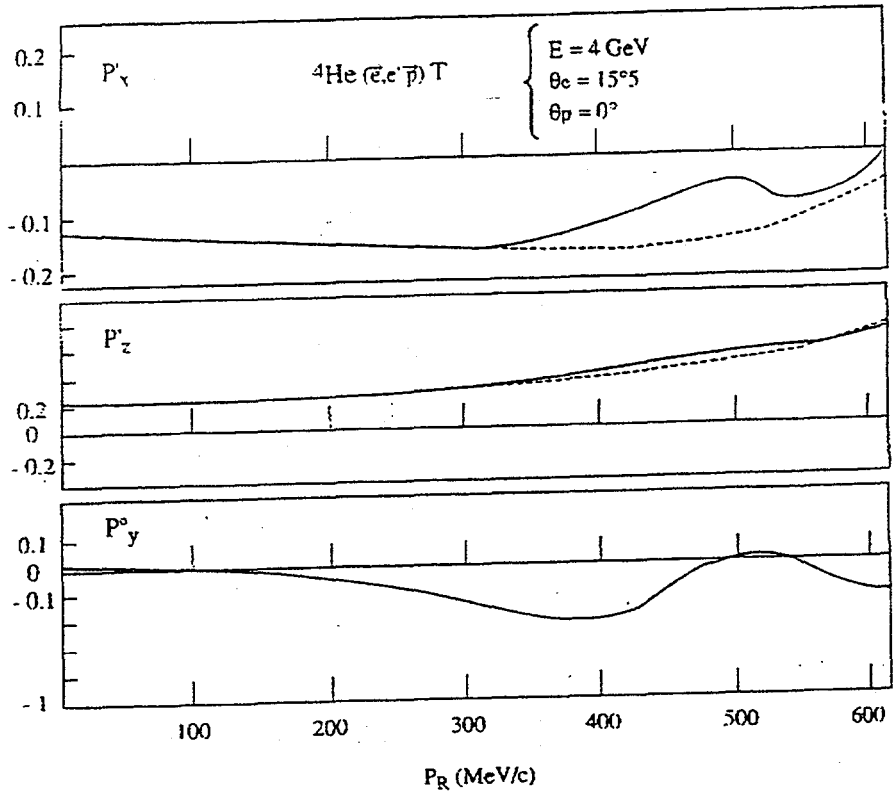

5. Final State Interactions in the Effective One-Body Interaction

The Spectator Model, although helpful in providing a conceptual framework for discussion, ignores critical features of the reaction process. In particular the nucleon-nucleus final state interaction (FSI) is both highly absorptive and explicitly spin dependent. Realistic treatments of nucleons in nuclei must account for these effects. For discussion purposes, it is useful to categorize the nuclear amplitudes into two classes:

Class I: Response functions that are present in the impulse approximation.
Class II: Response functions that vanish in the impulse approximation.

Second Class (Class II) response functions require some complexity in the interaction process to be observed. These may include FSI's, Meson Exchange currents (MEC), Isobar configurations (IC) and other two- and many-body couplings. In the case of ^{16}O, some of these effects have been studied extensively. Figure 9, provided by J.J. Kelly, shows polarizations from a typical co-planar $^{16}O(e,e'p)$ scattering experiment at kinematics appropriate for CEBAF.[12] This reaction is the subject of a Hall A commissioning experiment by Glashausser *et al.*[13] The results shown are for two FSI interaction models, the Empirical-Effective-Interaction (EEI) and a Dirac Phenomenological (DP) model. These models show little deviation in their predictions for this choice of in-plane, quasi-perpendicular scattering kinematics. The two First Class (Class I) polarization-transfer amplitudes differ little from the impulse approximation at modest recoil momentum, while the Second Class amplitude P_N is dramatically affected by the presence of final state interactions. The observation that the D_{LT} (labeled as "P_S") and D_{LL} ("P_L") responses are similar to quasifree proton knockout for modest recoil momenta is not due to the absence of FSI's but rather to the fact that the final state scattering does not significantly depolarize or otherwise alter these amplitudes. Extraction of nucleon properties via *(e,e'N)* does not depend on an absence of FSI's, but only on the insensitivity of selected amplitudes to the details of the FSI's.

Figure 9: $^{16}O(e,e'p)$ polarization observables for quasi-perpendicular kinematics at e_0=1.6·GeV and Tp=0.5·GeV.[12] The lines represent PWIA (dashed), EEI (dashed-dot) and DP (solid) calculations. The cusps at zero recoil are due to the rotation of the reaction plane basis.

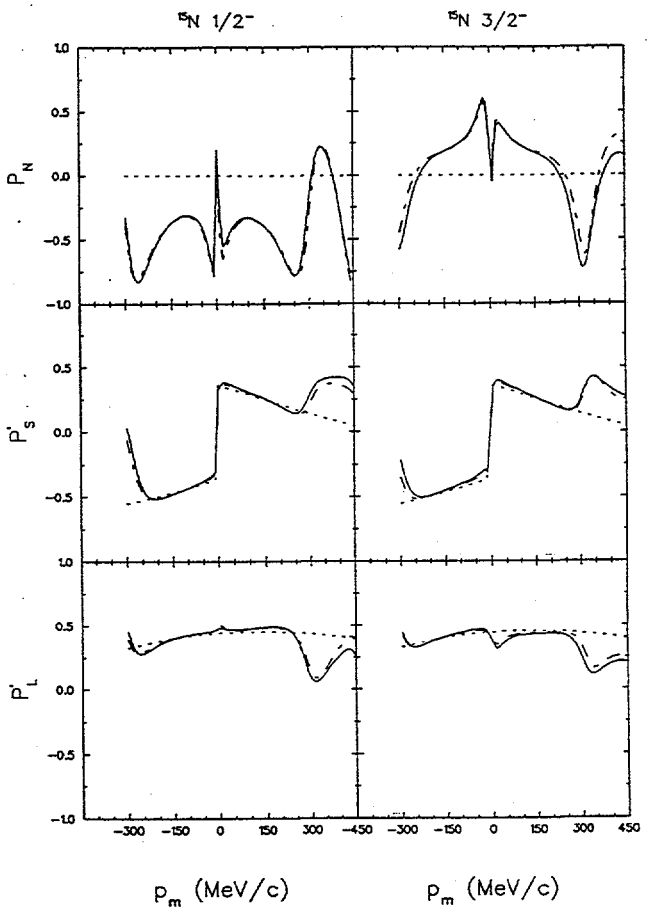

The surprisingly large values for the induced-polarization P_N is due primarily to two effects: 1) differential absorption of opposite spin states by the imaginary part of the central force, the so-called "Maris effect", and 2) the effect of the real part of the spin-orbit force.

Figure 10 illustrates the Maris effect for $p_{1/2}$ shell knockout. In this case the nucleon's orbital angular momentum has the opposite sign of the spin angular momentum. Quasifree knockout selects a fixed initial state of momenta **p***, which leads to opposite senses of orbital rotation **r**×**p*** depending on whether the scattering occurs on the front or rear face of the nucleus. Therefore the two spin components are differentially absorbed, leading to a net induced-polarization. If one sums over a closed shell

Figure 10: Illustration of the Maris effect: for $p_{1/2}$ shell knockout, scattering from the front and rear faces have different spins and absorptions.

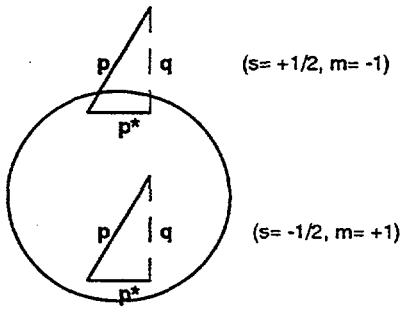

including both $p_{1/2}$ and $p_{3/2}$ states the effect averages out.

This is born out in Figure 11, which shows the effect of turning off the real and/or imaginary parts spin-orbit potential. The calculations by J.J. Kelly[12] are for the kinematics of Bates experiment E89-01.[14] In the absence of the spin-orbit term, the polarization comes primarily from the imaginary part of the central force, leading to an average polarization for $p_{3/2}$ shell knockout out that is half that for $p_{1/2}$ knockout. The real part of the spin-orbit potential is the other large ingredient in this calculation. Just as some amplitudes are insensitive to the FSI, others can be selected to explicitly study these effects.

Class II amplitudes, like the induced polarization, may help some light on the on-set of color transparency. This is the thesis of a Hall A proposal by Saha, who plans to explore the A and Q^2 dependence of the induced

Figure 11: Effect of spin-orbit potential on the induced polarization P_N at Tp=0.13 GeV (kinematics of Bates Exp. 89-01)[14] verses recoil momentum.[12] The solid line is the full EEI calculation of Kelly. The other lines are no spin-orbit potential U_{LS}=0 (long-dashed), Real U_{LS}=0 (dot-dashed), and Im U_{LS}=0 (short-dashed).

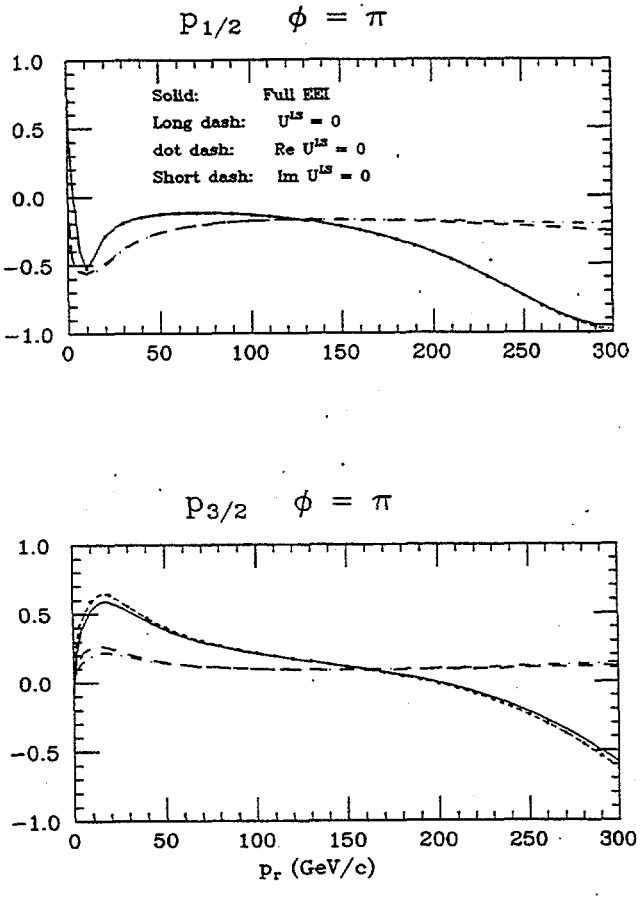

polarization.[15] Color transparency involves coupling to a small color singlet state that has weak FSI's. Therefore all Class II amplitudes should vanish at the on-set of color transparency. Whether or not color transparency can be reached at measurable beam energies, the systematics of the polarization response as a function of the energy domain may shed new light on the dynamics of the reaction mechanism.

6. Coupled Channel Calculations

Coupled channel (CC) effects for the $^{16}O(e,e'N)$ reaction have been studied by J.J. Kelly.[16] Not surprisingly, he finds that the effect depends on the coupling scheme and are somewhat larger for *(e,e'n)* than for *(e,e'p)*. Kelly's coupling scheme is shown in Figure 12. In addition to direct knockout, he includes elastic reorientation, charge exchange and inelastic scattering. The CC effects are larger for those amplitudes that vanish in the absence of FSI's. Some of the largest effects occur for responses that vanish in co-planar kinematics. Figure 13 shows some selected Class II response functions that contribute to the induced polarization and vanish in co-planar kinematics. This illustrates the need to perform out-of-plane as well as co-planar experiments.

Figure 12: Coupling scheme for $^{16}O(e,e'N)$ p-shell knockout.[16] The Heavy lines denote direct knockout, circles indicate elastic reorientation, horizontal and vertical lines indicate charge exchange, and vertical lines indicate inelastic scattering.

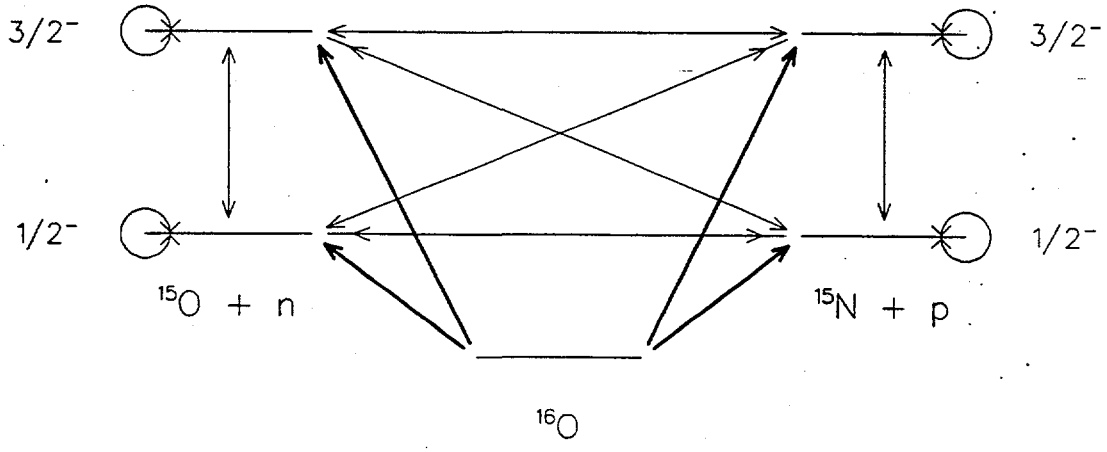

Figure 13: Selected response functions for $^{16}O(e,e'n)^{15}O$ in quasiperpendicular kinematics at e_0=0.5·GeV and T_N=0.135· GeV. [16] This set contributes to the induced-polarization, lies in the reaction plane and requires out-of-plane spectroscopy.

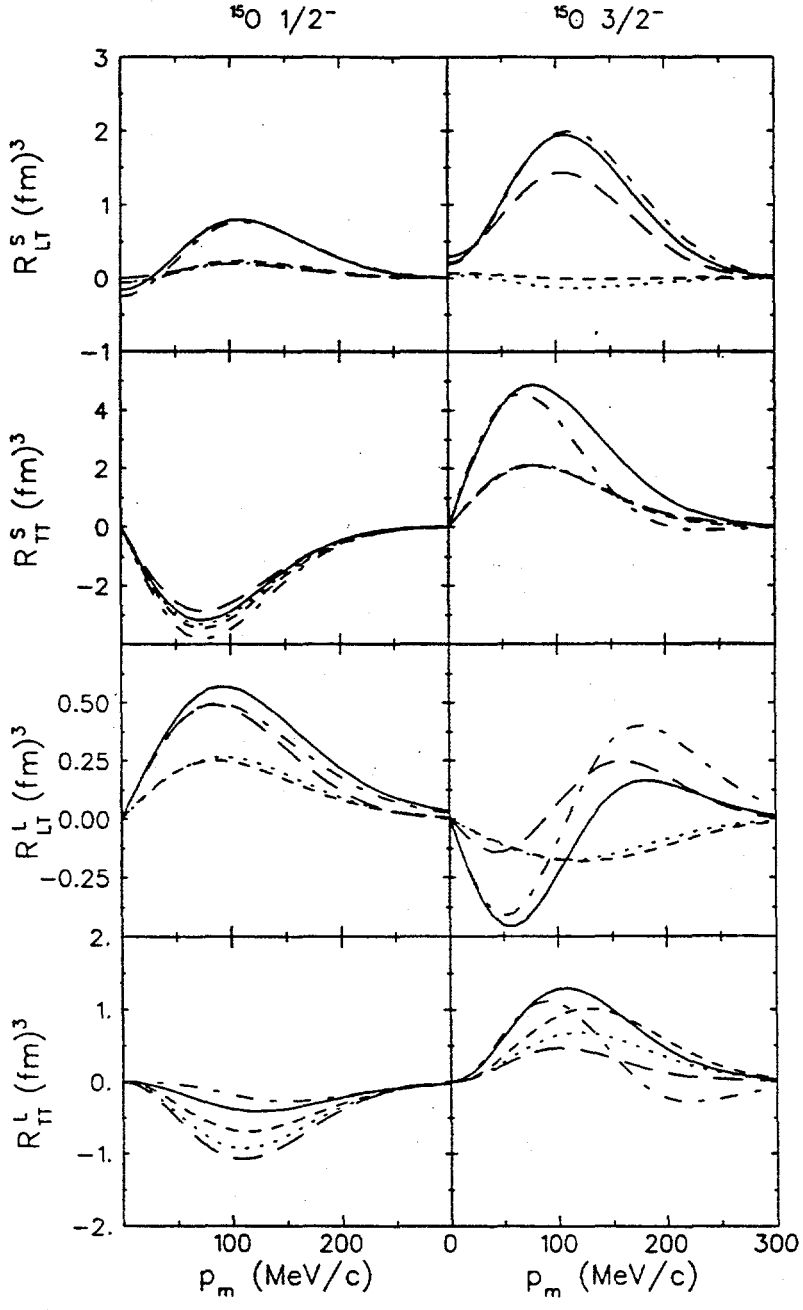

7. Two-Body Currents

Present calculations of the unpolarized *(e,e'p)* coincidence reaction, although doing a relatively adequate job of fitting the overall cross sections, have difficulty in reproducing the details of the smaller response functions. For example, results for the unpolarized $^{16}O(e,e'p)$ experiment of Spaltro et al.[17] are shown in Figure 14. The differences between the calculation and the data for the R_{LT} (W_{LT}) response in the $p_{3/2}$-shell are considered to be too great to be due soley to the choice of optical model.

Figure 14: ^{16}O(e,e'p) unpolarized response functions measured at NIKHEF by Spaltro, *et al.*[17]

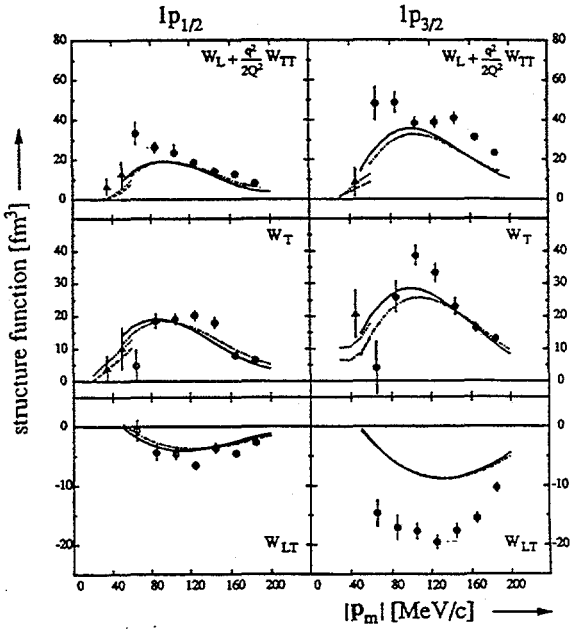

Obtaining a quantitative understanding of two-body currents in the nuclear medium is a challenging task. It must begin by exploring the *d(e,e'p)n* reaction as the fundamental benchmark for testing theoretical two-body calculations. The contributions of these currents to the spin response provides sorely needed constraints to the models.

At Bates[18] we have begun a series of measurements of the $x = Q^2/2m_p\omega$ behavior for the $d(\vec{e},e\vec{p})n$ polarization transfer reaction. Figure 15 from Arenhövel[19] shows the polarization amplitudes expected at quasifree kinematics *(x=1)*. The response of the first class amplitudes is insensitive to the details of the reaction model until one reaches relatively high recoil momenta. The situation changes dramatically as one moves to smaller x. Figure 16 shows the expected "P_L" (D_{LL}) response in the dip region between the quasielastic peak and the delta resonance excitation. This polarization amplitude is now quite sensitive to MEC and IC contributions. We plan to follow-up these experiments at CEBAF.[20] We hope to extend these explorations to cover the region *x=(0.34, 1.5)* at a probable beam energy of 1.6·GeV. This will cover the kinematical range from the delta resonance to the negative-y region. The kinematic points will be selected to emphasis different ingredients in the reaction model.

Figure 15. Calculations by Arenhövel[19] of the in-plane recoil protron polarizations for the $d(e,e'p)n$ reaction at e_0=0.9·GeV and ϑ_e=60°.[18]

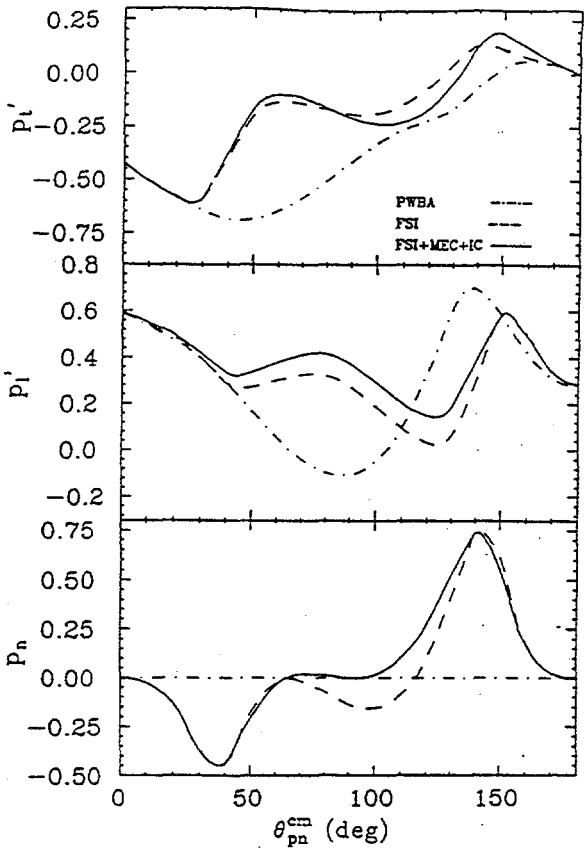

Figure 16: longitudinal proton polarization as calculated by Arenhövel for the dip region kinematics of Bates Exp. 88-21.[10] The curves are PWBA (dash double-dot), PWBA+RC (dash triple-dot), PWBA+FSI (dots), PWBA+FSI+IC (long dash), PWBA+RC (short dash), PWBA+FSI+IC+RC (solid).

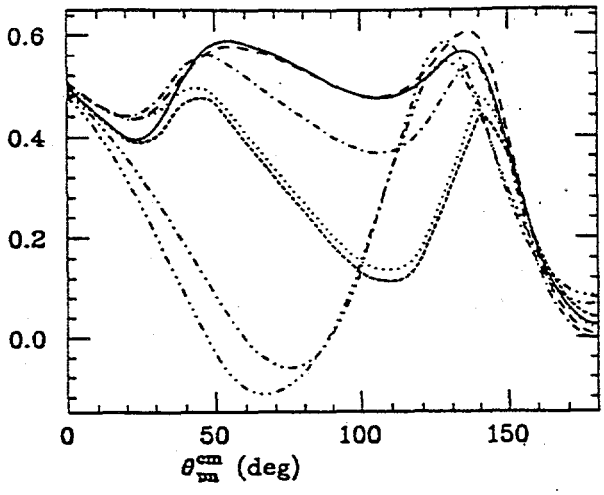

Experiments with vector polarized deuterium targets also show sensitivity to the reaction ingredients. The BLAST collaboration[2] has examined the exclusive $\vec{d}(\vec{e},e'p)n$ cross section for a internal vector polarized gas jet target in the Bates SHR. Both quasielastic and delta kinematics have been analyzed. The scattering asymmetries can be written as

$$\sigma(h,P_1^d,P_2^d)=\sigma_0\left[1+hA_e+P_1^dA_d^V+P_2^dA_d^T+h\left(P_1^dA_{ed}^V+P_2^dA_{ed}^T\right)\right]. \qquad (7.1)$$

where σ_0 denotes the unpolarized cross section. P_i^d denote the target polarization orientation parameters, and A_i are the scattering asymmetries. To separate the reaction components, the target is oriented parallel ($\theta_d=0$) or perpendicular ($\theta_d=\pi/2$) to q. As an example of the expected sensitivities, the results for the $A_{ed}^V(\theta_d,\phi_d)$ asymmetry for Δ kinematics is shown in Figure 17.

Figure 17: $A^V_{ed}(\theta,\phi)$ asymmetry in Δ kinematics (e_0=0.88·GeV, ω=0.378·GeV, and θe=31.2°). The Paris NN potential was used in the calculation. The curves are: PWIA (dots), FSI (dashes), FSI+MEC (dash-dots) and complete calculation (solid).

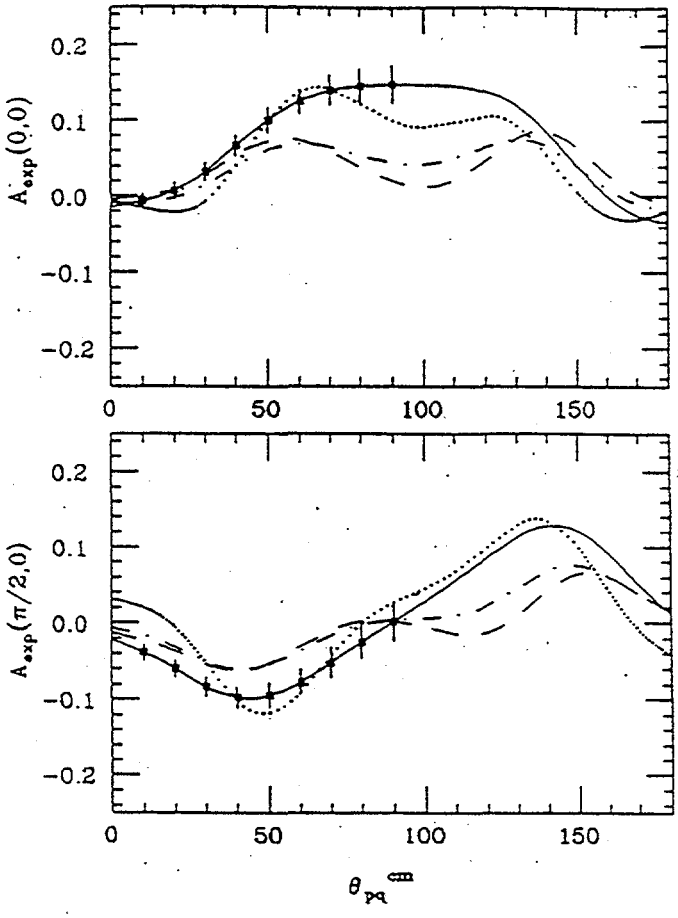

8. Comparative Methods

Recoil polarimetry has developed rapidly in recent years into a relatively mature technology. Its main limitation is the low figure of merit of FPP's which, unfortunately, is inherent to the analyzing process. One area of improvement would be to couple recoil polarimetry to out-of-plane spectroscopy. This would greatly increase the number of accessible amplitudes that could be measured.

Target polarimetry by comparison, is still a developing art form. Every target environment and nuclear species requires an unique approach. It is, however, a rapidly improving technology whose fundamental limits have not yet been reached.

Polarized target developments can be classified into three categories:

1. External targets: The major need is to improve target density and maximum luminosities.
2. Internal gas jet targets: These are used with storage rings. Beam storage lifetimes are coupled to target density, limiting luminosity.
3. Polarized colliding beams: These allow isotopically pure beams and open up the possibility of tagging the residual spectator. Construction cost and maximal luminosity are the major issues.

9. Concluding Remarks

In summary, the electromagnetic spin response of nucleons in nuclei has a rich structure. To fully explore this structure requires full decomposition of the virtual photon amplitudes as well as measurement of target and recoil polarizations. The initial spin physics experiments have thus far focused primarily on measurements of elastic nucleon form factors. One must go beyond free nucleon behavior, however, if one wants to understand how nucleons interact with nuclear matter.

Luminosity limitations in polarized target experiments and low efficiency of recoil polarimeters means that only a limited number of selected experiments can be performed. Indeed, a blast furnace like CEBAF is needed just to move the experimental effort past the conceptual proof of principle stage.

A short list of important experiments suitable for a multi-year program of *(e,e'N)* spin physics studies might include:

- Measurement of nucleon form factors to the level needed to constrain nuclear models.
- Measurement of two-body currents in a fundamental way in the deuterium system.
- Studies of the three body system, as the first truly complex nuclei and one for which complete calculations are being developed.
- A generic survey of the A and Q^2 dependence of (e,e'N) reactions to map out the basic phenomenology of the reaction mechanism.
- Detailed case studies of a few representative shell model nuclei.

Not surprisingly, there are pending proposals at all the major electron facilities which, taken together, will span these topics. If they are all carried out, the next decade should prove to be a busy one indeed for electromagnetic nuclear physics. The full exploitation of the power of the electromagnetic probe is only now becoming a reality. It is being driven by the power of the new high duty factor machines and the development of new spin physics techniques. I am confident that the next generation of electromagnetic nuclear physics will play a decisive role in our understanding of nuclear matter in terms of its fundamental degrees of freedom.

Acknowledgments

I would like to thank the organizers of the fall Division of Nuclear Physics meeting in Williamsburg for this invitation to speak at the Workshop on Spin Degrees of Freedom in Electromagnetic Nuclear Physics. I would also like to thank H. Arenhövel, J.J. Kelly, R.W. Lourie, R. Madey, J. McIntyre and P.E. Ulmer for their assistance with this talk and/or for unpublished material shown here. This work is supported in part by a grant from the National Science Foundation.

References

[1] D. Day, spokesman, CEBAF Exp. **PR-93-026**; R. Madey, spokesman, CEBAF Exp. **PR-93-038**.

[2] *A Proposal for the Bates Large Acceptance Spectrometer Toroid*, the BLAST collaboration, unpublished.

[3] A. Picklesimer and J.W. Van Orden, Phys. Rev. C **35** (1987) 266.

[4] P.E. Ulmer, CEBAF technical note **TN-91-101** (1991).

[5] T. deForest, Jr., Nucl. Phys. **A392** (1983) 232.

[6] M. van der Schaar *et al.*, Phys. Lett. **66** (1991) 2855; **68** (1992) 776.

[7] SLAC Exp. **NE-18**, R. Milner, spokesman.

[8] T. Wilbois, G. Beck, and H. Arenhövel, MAINZ preprint, **MKPH-T-93-10** (1993).

[9] B. Mosconi and P. Ricci, Nucl. Phys. **A517** (1990) 483.

[10] R.W. Lourie, Invited talk at the 14th International Conference on Few Body Problems in Physics, Williamsburg, Va. (1994).

[11] Hall A Collaboration, C R. Ent, P.E. Ulmer and J.F.J. van den Brand, spokesmen, CEBAF Exp. **PR-93-047**.

[12] J.J. Kelly, private communication.

[13] Hall A Collaboration, C. Chang, C. Glashausser, S. Nanda, and W. Van Orden, spokesmen, CEBAF Exp. **PR-89-033**,.

[14] J.M. Finn and P.E. Ulmer, spokesmen, Bates Exp. **89-01**.

[15] Hall A Collaboration, A. Saha, spokesman, CEBAF Exp. **PR-91-006**.

[16] J.J. Kelly, U. Md preprint **PP#95-22**, Submitted to Phys. Rev. C.

[17] C.M. Spaltro *et al.*, Phys. Rev. C **48** (1993) 2385.

[18] J.M. Finn, R.W. Lourie, C.F. Perdrisat, and P.E. Ulmer, spokesmen, Bates Exp **88-21**.

[19] H. Arenhövel, private communication.

[20] Hall A Collaboration, J.M. Finn and P.E. Ulmer, spokesmen, CEBAF Exp. **PR-89-028**.

POLARIMETRY IN THE FEW GeV REGION

C.F. PERDRISAT

the College of William and Mary,

Williamsburg, VA 23185, USA

October 26, 1994

ABSTRACT

The properties of polarimeters used in a number of Laboratories, to measure the polarization of secondaries produced in a nuclear target, in the range of energy 100 MeV to 12 GeV, are reviewed. The nature of polarization experiments will be discussed and several examples of new experiments used to illustrate the power of this technique. New development both for protons and for deuterons will be discussed in some details. Calibrations data and fits both for protons, to 2.4 GeV, and deuterons, to 700 MeV, will be presented.

1 Introduction

Over the last 5 years we have seen a number of new polarimeters built in medium to high energy facilities (defined here as 200 MeV to 12 GeV accelerator facilities), to measure the polarization of one of the products of a nuclear reaction. These are mostly proton or deuteron polarimeters; the most recent one is presently in construction at CEBAF for the hadron arm, one of the two HRS's in hall A, with NSF support; another one is ready to received particles at Bates, in the focal plane of OHIPS (built by a U.Va/ MIT/WM collaboration with DOE and NSF support).

First the general principle of a polarimeter for either proton or deuteron, will be outlined. Two examples of approved CEBAF experiments which will use a polarimeter, in halls A and C, will briefly be presented, to illustrate the fact that polarization is an interference phenomenon; also, the results of a measurement of the polarization transfer in inclusive dp breakup, using a proton polarimeter will be shown. A review of the principle of the polarimeter with application to protons and deuterons will follow. After presenting a short historical account of polarimeter developments over the last 20 years a short review of the present status of polarimeter calibrations will be given. It will include the most recent effort to extend the energy range of calibration of the polarimeter POMME at Saturne up to 2.4 GeV in proton. A discussion of parametrizations of these calibration results will follow. I will also outline plans for extending the energy range of both proton and deuteron polarimeters by using a hydrogen analyzer, and in the second case, selecting elastic dp events with a coincidence requirement, which are underway at Saclay. Other possible schemes for deuterons (AHEAD and POLDER) will be mentioned.

Not included in this discussion will be beam polarimeters, which are typically two- or four arm devices measuring combinations of left-right and (or) up-down asymmetries. Because of their small acceptance (both in phase-space and efficiency) these are not

appropriate to measure the polarization of the outgoing particles of a nuclear reaction at the energies considered here. However, some interesting calibrations at Saclay and KEK have used left-right coincidence geometries; their results will be included here for their relevance to future higher energy applications.

2 Polarimeters for Protons or Deuterons

The polarimeters to be discussed here are of the following general description: the track of an incident particle is defined in several position sensitive detectors; the incident particle is scattered in an analyzer, usually a bloc of graphite or liquid hydrogen, and the track of the outgoing particle(s) is (are) defined in a second set of position sensitive detectors located downstream of the analyzer; this configuration is illustrated in Fig. 1.

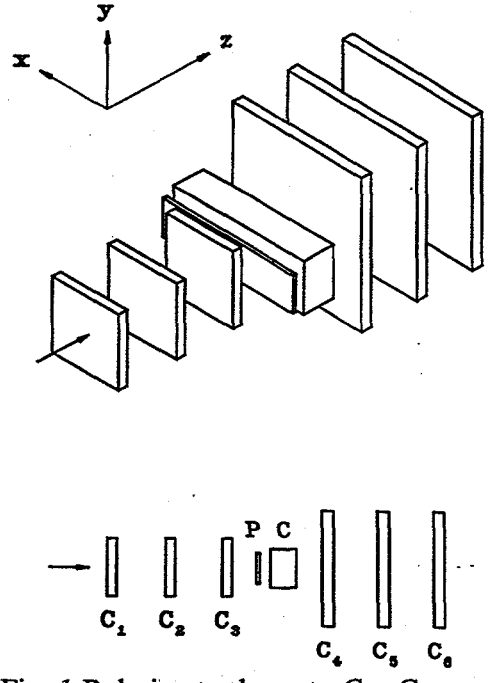

Fig. 1 Polarimeter layout : $C_1 \ldots C_6$ are tracking chambers, C is the analyzer and P a scintillating trigger detector.

Recently built polarimeters have an azimuthal acceptance of 2π, and a polar acceptance of 15 to 30^0. The tracking detectors are now universally wire chambers, either MWPC or Drift Chambers. In the future combinations of scintillating fibers and position sensitive Photomultipliers may provide faster and simpler solutions (Perdrisat et [al]).

The trigger of a polarimeter is provided by a set of scintillation detectors determining the arrival of a particle and its exit from the downstream chambers; multitrack events are rejected. In general no attempt is made to identify the outgoing particle, so these polarimeter use the semi inclusive reaction C(p,charged particle)X; an exception we will discuss later is POMME used with deuterons, where the outgoing particle is required to be a deuteron using a range technique.

The polarization of the incident particle scattered in the analyzer produces an azimuthal distribution which, for spin-1/2 particles, is of the general form:

$$N(\theta,\phi) = N_0(\theta)\,[1 + A_y(\theta)\,(P_y \cos\phi - P_x \sin\phi)] \qquad (1)$$

where θ and ϕ are the polar and azimuthal angles of scattering at the analyzer. $N(\theta,\phi)$ and $N_0(\theta)$ are the number of particles recorded after the analyzer, for polarized and unpolarized beam, respectively; $A_y(\theta)$ is the analyzing power, which depends upon the material of the analyzer, the energy of the particle and the polar angle; P_y and P_x are the projections of the polarization onto the vertical- and horizontal-axis, respectively and these can be determined by Fourier analysis of the empirical azimuthal distribution $N(\theta,\phi)$.

Typical polar and azimuthal distributions for 1.8 GeV protons are seen in Fig. 2a and b, respectively (Cheung et al[2]). The amount of material in the analyzer does determine the probability of nuclear interaction, and therefore the efficiency of the polarimeter.

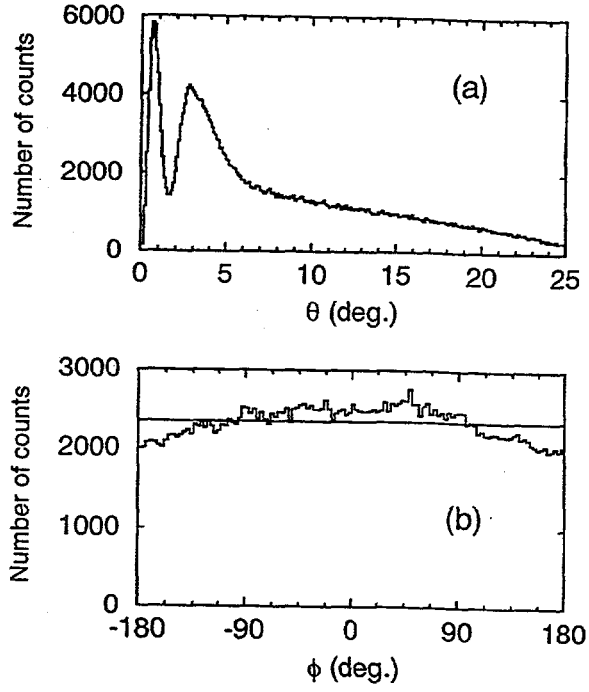

Fig. 2 a) Polar- and b) azimuthal angular distribution at T_p=1.8 GeV.

In first approximation, valid at the energies considered here, the probability of (any) nuclear interaction in the analyzer material is given by the nuclear collision length, which for carbon is 60.2 gcm^{-2}. The probability for nuclear interaction is then $\epsilon_{nuclear} \sim (1\text{-}e^{-\ell/60.2})$. In fact this is an overestimate; neutrals in the final state will not be detected, and the efficiency is typically one fourth $\epsilon_{nuclear}$. The actual efficiency depends on the configuration of the trigger and the geometrical acceptance of the detectors. We will discuss the criteria for choosing the proper amount of analyzer material later. The quantity $\langle \epsilon A_y^2 \rangle^{1/2}$ obtained

by integrating over the accepted polar angle range is called the "coefficient of merit". It enters directly into estimates of the statistical uncertainty calculation; for a measurement of the polarization components P_x and P_y, the statistical uncertainty is given by:

$$\Delta P_x = \Delta P_y \sim \sqrt{\frac{2}{\langle \varepsilon A_y^2 \rangle N}} \qquad (2)$$

Here N is the total number of particles incident on the polarimeter. In fact the statistical uncertainties are directly determined by the Fourier analysis of $N(\theta,\phi)$.

3 Nature of Polarization Observables

Generally polarization observables are the results of an interference between several amplitudes contributing to the same transition. This is most easily illustrated for elastic scattering of longitudinally polarized electrons with on unpolarized protons. In this case there are two components of the recoil proton polarization, P_t and P_l. These are related to the elastic electric and magnetic form factors of the proton, G_{Ep} and G_{Mp}, as follows:

$$P_t = \frac{-2\sqrt{\tau(1+\tau)}\,G_{Ep}G_{Mp}\tan(\theta_e/2)}{I_0} \qquad (3)$$

$$P_l = \frac{\frac{E_e+E'_e}{M}\sqrt{\tau(1+\tau)}\;G_{Mp}^2\tan^2(\frac{\theta_e}{2})}{I_0} \qquad (4)$$

$$I_0 = G_{En}^2(Q^2) + \tau G_{Mn}^2[1+2(1+\tau)\tan^2(\frac{\theta_e}{2})] \qquad (5)$$

$$\tau = \frac{Q^2}{4M_p^2} \qquad (6)$$

Hence the transverse polarization is the result of an interference of G_{Ep} and G_{Mp}. In general

$G_{Ep}G_{Mp}$ is larger than G_{Ep}^2; the polarization method is sensitive to small amplitudes. The standard way to determine G_{Ep} is of course the Rosenbluth separation:

$$\frac{d\sigma}{d\Omega_e} = \frac{d\sigma}{d\Omega_{Mott}}\left[G_{En}^2(Q^2) + \tau G_{Mn}^2\left[1+2(1+\tau)\tan^2\left(\frac{\theta_e}{2}\right)\right]\right] = \frac{d\sigma}{d\Omega_{Mott}} I_0 \qquad (7)$$

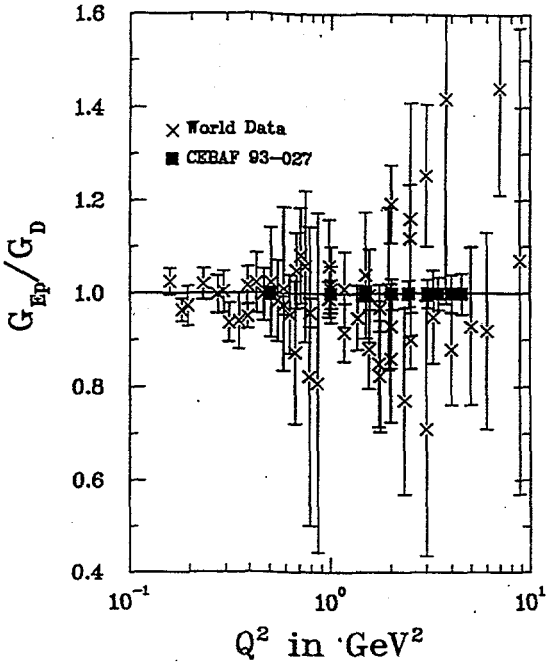

Fig. 3 Expected error bars for G_{Ep} in ref. 3.

Approved experiment 93-027[3] at CEBAF will measure P_t and P_l, and obtain G_{Ep} over G_{Mp}. The performance anticipated for this experiment is shown in Fig. 3. A similar idea is the basis of the study of the same reaction in the quasielastic domain on the deuteron (CEBAF 89-028[4]) and on ^{4}He (CEBAF 93-049[5]). An important factor in deciding to build a polarimeter in hall A, was the expectation that it would be a more sensitive technique to determine small amplitudes than cross section measurements, because of the interference nature of polarization. This is a good example of the power of this technique.

Another example is the measurement of the t_{20}-polarization of the recoil deuteron in elastic ed ; t_{20} is connected to the 3 from factors of the deuteron, G_C, G_M and G_Q as follows:

$$t_{20} \times I_0 = -\frac{1}{3\sqrt{2}}\eta\left[8\, G_Q\left(G_C + \frac{1}{3}\eta G_Q\right) + G_M^2\left(1 + 2(1+\eta)\tan^2\left(\frac{\theta_e}{2}\right)\right)\right] \qquad (8)$$

In this case the interference is between G_C and G_Q; t_{20}-data combined with the existing data base for $A(Q^2)$ and $B(Q^2)$ allows separation of the 3 form factors; this is an approved experiment in hall C at CEBAF[8]; a recent measurement of t_{20} has brought the Q-range over which the 3 form factors are separated to 4.6 fm^{-1} (Garçon et al.[7]).

Hadronic reactions present a similar demonstration of interference within the impulse approximation (IA). For inclusive breakup of polarized deuterons on hydrogen, with proton detected at 0^0, the vector polarization transfer coefficient, from the deuteron to the proton, κ_0, is entirely determined by the deuteron S- and D-wave functions in momentum space:

$$\kappa_0 = \frac{u^2 - w^2 - \frac{uw}{\sqrt{2}}}{u^2 + w^2} \quad (9)$$

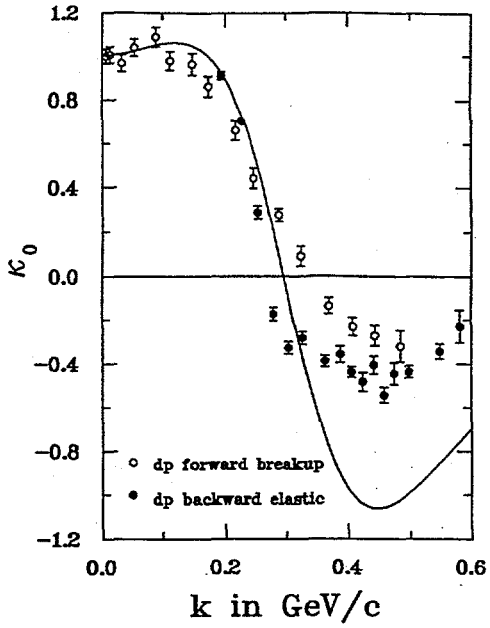

Fig.4 Polarization transfer ratio κ_0 in dp breakup and backward elastic scattering

Within the IA then, the polarization transfer coefficient results from an interference also; Fig. 4 shows the data for κ_0 in inclusive dp breakup (V. Punjabi et al[7]).

4 Early Polarimeters

One of the earlier polarimeters with 2π acceptance was built at the CERN synchrocyclotron in the early 70's. The setup is shown in Fig. 5 (Aebischer et al[9]). The polarimeter was

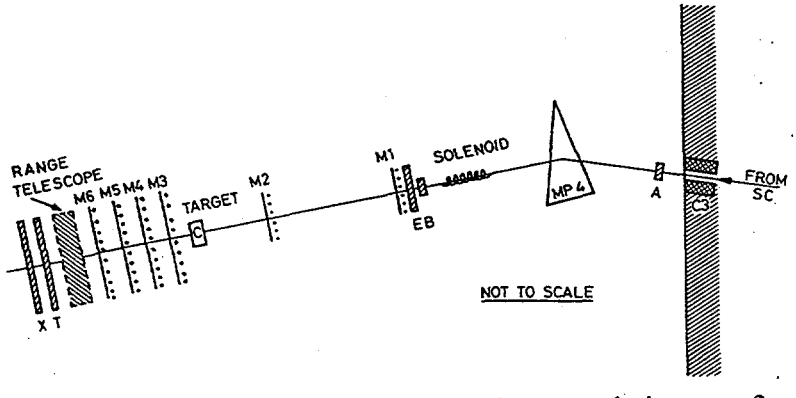

Fig. 5 Layout of CERN synchrocyclotron polarimeter of ref. 9.

calibrated from 400 to 576 MeV. Interestingly, requiring near-elasticity with an iron absorber

in front of scintillator T in Fig. 5, was observed to result in significantly larger analyzing powers; however, particle losses in this absorber cancelled the gain in analyzing power.

A short time later a similar polarimeter was built at TRIUMF on the neutron beam, by the NN group (Waters et al[10]). Their calibration results are shown in Fig. 6, where the CERN results at 399 and 462 MeV are also shown to emphasize the effect of removing inelastic events.

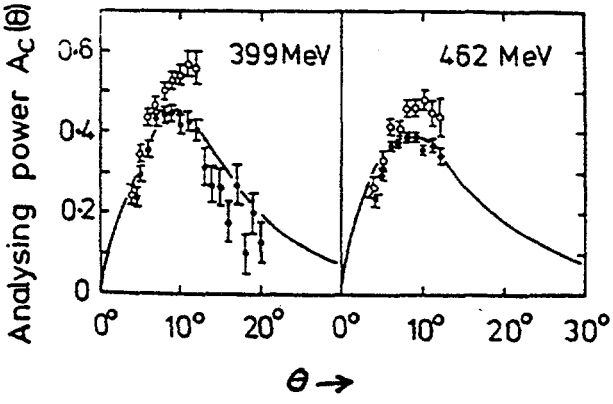

Fig. 6 TRIUMF calibration data compared of ref. 10 to CERN data (ref.9).

Most illustrative of this series of polarimeters is one built and studied at LAMPF (JANUS) in the early 80's (Ransome et al[11] and McNaughton et al[12]).

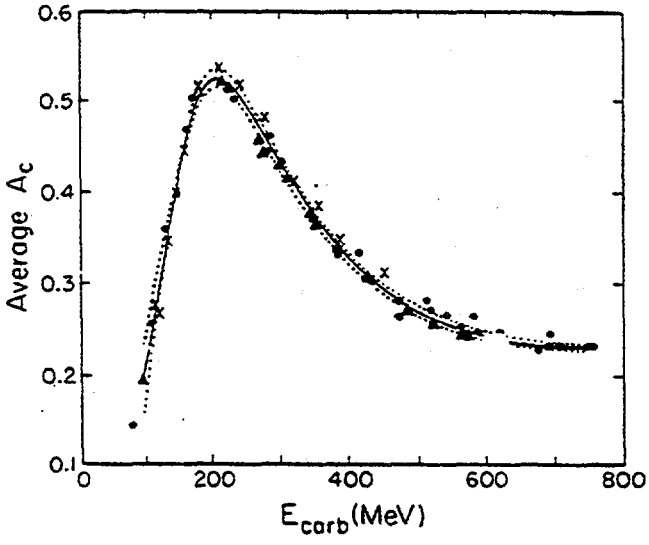

Fig. 7 Energy dependence of A_y^C data from LAMPF(ref. 12), SIN (ref. 13) and (ref.10).

Their systematic calibration results, from 100 up to 750 MeV, when compared with similar work at SIN[13] and TRIUMF (ref. 10) demonstrated for the first time, that such devices were almost universal, as seen in fig. 7 taken from ref. 12: it follows that a calibration made with one polarimeter can be used with a polarimeter of similar design in another laboratory, with an accuracy of a few percents over this energy range.

All these polarimeters used relative small thicknesses of graphite, to limit the amount of multiple scattering. With small Carbon thickness a large fraction of the protons traverse without nuclear interaction; these events appear as a very prominent 0^0 peak in the θ-spectrum, and have no usable analyzing power. Many electronic schemes have been designed

to reject such Coulomb events with a fast analogic or logic decision. These will not be discussed here for lack of time. The various references cited here provide the information.

The calibration of the polarimeter POMME at Saturne in 1988 lead to the conclusion that significantly larger coefficients of merit could be obtained from a search for the optimum value of the thickness of the analyzer (see Bonin et al[14]). The larger coefficients of merit or ref. 14 increase the range of usefulness of polarimeters considerably, both in energy and sensitivity. Multiple Coulomb scattering is not a problem. At 500 MeV, increasing the Carbon thickness from 12.7 (ref.12) to 31.2 cm (ref. 14) increases $<\theta^2>^{1/2}$ from 17 to 27 mr; but this increase of thickness more than doubles the efficiency; in addition the analyzing power is also slightly increased.

5 Recent Calibrations for Protons

The most recent polarimeter for 100 to 1000 MeV protons was built for the OHIPS spectrometer at Bates by a U.Va./MIT/WM collaboration[15]; it accepts graphite analyzer blocs up to 30 cm thickness. Prior to its installation at Bates it was calibrated at IUCF from 120 to 200 MeV (Baghei et al and Lourie et al[16]). Some results for 177 MeV are shown in Fig. 8 together with SIN and LAMPF results; the polarimeter is now installed in OHIPS for polarization transfer measurements in ^{1,2}H(e,e'p) with polarized electrons. It uses commercial ECLine hardware to reject small angle events in typically 180 ns; including the readout time the dead time is 600 ns.

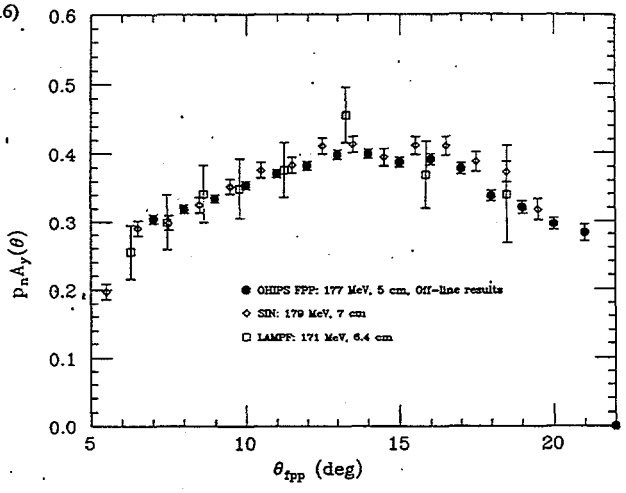

Fig. 8 Calibration data of new Bates polarimeter (ref. 15).

As a basis for several experiments to measure polarization transfer in inclusive dp breakup and in backward dp elastic scattering in Saclay, the calibration of the proton polarimeter POMME was extended in 1991-3, from the original range 200 to 1200 MeV (see

ref. 14), to 2400 MeV. The results of this calibration are to be published (ref. 2); they are shown in Fig. 9, together with a fit explained in the appendix. These calibrations were made with 31.2 cm of graphite of density 1.7 gcm^{-3}. With such thickness the fraction of events rejected with a fast small angle rejection system becomes about 50%; on-line small angle rejection is not critical as fast storage media make this overhead relatively unimportant. As expected on the basis of simple consideration about interaction in a thick bloc of material, the efficiency of the polarimeter is largely independent of energy, and close to 0.15 for 31.2 cm.

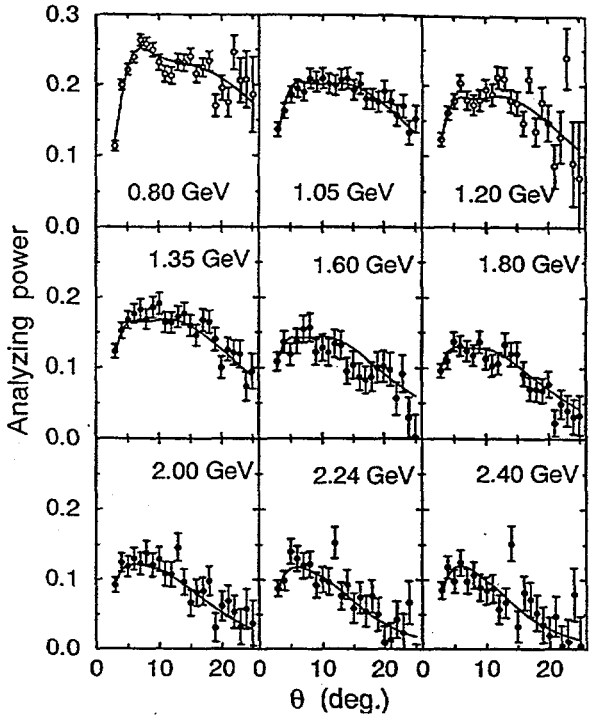

Fig. 9 Calibration data of polarimeter POMME up to 2.4 GeV (ref. 2).

The analyzing power, and therefore the coefficient of merit $<\epsilon A_y^2>^{1/2}$, both decrease monotonically with energy; the coefficient of merit is still 0.035 at 2.4 GeV.

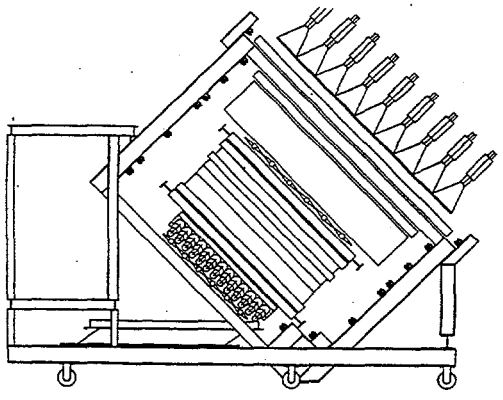

Fig. 10 View of the hadron arm detector package for hall A at CEBAF.

A large polarimeter is being constructed for the hadron HRS in hall A at CEBAF by a Rutgers-WM-Georgia-NSU[17] collaboration. It will cover the whole 10 % momentum acceptance of the spectrometer and uses a graphite analyzer. It can accommodate up to 60 cm of graphite and should operate at least to 2.4 GeV proton energy; multiple scattering angle will be 10 mr at this energy. The general configuration of the hall A polarimeter is shown in Fig. 10.

Use of a graphite analyzer at energies larger than 2.4 GeV is not impossible. Bystricky

et al[18] have measured the ratio $A_y^c(p,2p)/A_y^{pp}$ up to 2.8 GeV, without energy selection; the ratio appears to be constant above 2 GeV and equal to 0.4, in excellent agreement with the data of ref.2 at 2.4 GeV. Ohmori et al[19] have measured the exclusive ratio $A_y^C(p,2p)/A_y^{pp}$ at 3.5 GeV proton energy and found 0.72; see Fig. 11. One would expect the exclusive (p,2p) analyzing power to increase monotonically with energy towards 1; Fig. 11 indicates that the inelasticity, starting around 1 GeV, decreases the analyzing power drastically.

The authors of ref. 19 explain the difference with the results of ref. 18 as due to the inelasticity in these data; in ref. 19 pion production is excluded because both protons are selected with magnetic analyzers. In ref. 19 it is also shown that for a deuterium target, the ratio $A_y^d(p,2p)/A_y^{pp}$ is 0.62, but that the same ratio decreases to 0.4 when events containing pions are included.

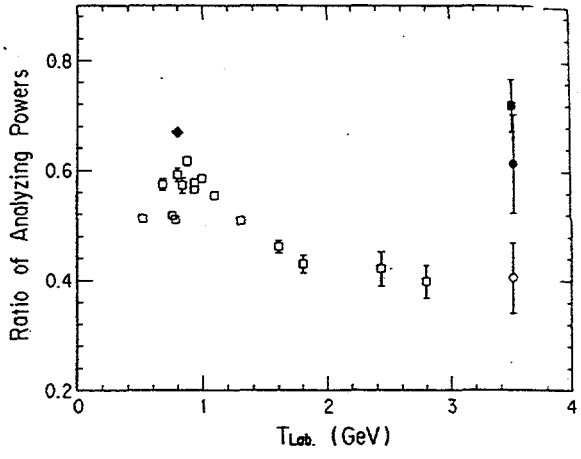

Fig. 11 Ratio $A_y^C(p,2p)/A_y^{pp}$ versus proton energy (data of ref. 18 and 19).

It appears then that selecting "elastic or quasi elastic" events increases the analyzing power of a Carbon analyzer by as much as a factor of 2; but the selection of such events must not be made at the cost of efficiency if the figure of merit is to be improved!

Based on the work of references 18 and 19 one can predict that the inclusive Carbon analyzing power will keep decreasing slowly above 2.8 GeV; using the pp polarization data of Spinka et al[19] one can predict that at 4 GeV/c (≈3.2 GeV) the value of A_y^C will still be approximately 0.08. With 32 cm of graphite the expected ϵ should be 0.15; increasing the Carbon thickness to 60 cm (as will be done at CEBAF) will double ϵ, for a predicted $\langle \epsilon A_y^2 \rangle^{1/2} = 0.04$ at 3.2 GeV.

Another interesting solution consists in replacing the Carbon by liquid Hydrogen, thus increasing A_y from 0.08 to 0.2 at 3.2 GeV. A 27 cm long LH_2 cell would have the same coefficient of merit as a 32 cm graphite analyzer if (p,2p) events are selected. To extend this technique to yet larger energies appears difficult. As discussed in ref.18 and 19, the reason for the decrease of the pC analyzing power with increasing energy has to do with the inclusive

nature of the reaction used.

6 Deuteron Polarimeters

It has been demonstrated by Bonin et al.[21] that a deuteron polarimeter with good analyzing power could be obtained by modifying the trigger of a 2π- polarimeter like POMME: adding an absorber in front of the exit scintillator so as to select deuterons only, stopping most of the breakup protons gives good (iT_{11}) and T_{22}, with practically no T_{20} or T_{21} analyzing power; the calibration extends to 700 MeV. This should be compared with the dp polarimeter AHEAD in ref. 7, for which all 4 analyzing powers are non-zero, but with an energy range limited to 250 MeV, and to the (d,pp) polarimeter POLDER[22] which has no usable vector analyzing power, but good tensor analyzing powers and can be used to about 500 MeV.

For deuterons the angular distribution has a sin ϕ and cos ϕ, as well as a cos 2ϕ term:

$$N(\theta,\phi) \quad N_0(\theta)[1 + t_{20}T_{20} + 2[(it_{11})(iT_{11}) + t_{21}T_{21}]\cos\phi + 2[t_{11}T_{11} + (it_{21})(iT_{21})]\sin\phi + 2t_{22}T_{22}\cos 2\phi] \qquad (10)$$

At deuteron energies larger than 1 GeV it is necessary to use a hydrogen analyzer; the elastic dp reaction is known to have large analyzing powers in the whole energy range 1 to 2 GeV. The simplest way to select elastic dp is to detect both particles in coincidence, and reconstruct the angle $\theta_p + \theta_d$ to reject inelastic events. A modification of POMME is being proposed with the Carbon analyzer replaced by 3 or 4 cylinders of LH_2 oriented perpendicularly to the polarimeter axis as shown

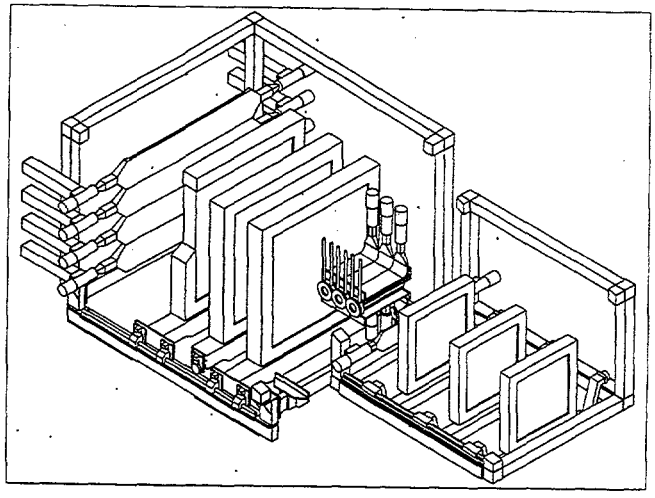

Fig. 12 Proposed modification of POMME to extend deuteron energy range to 2 GeV.

in Fig. 12. Each hydrogen cell would be 7 cm in diameter and 50 cm long. The proton angle will be detected in two planes of multilayered straw drift tubes. Monte Carlo simulations (see Tomasi -Gustafsson and Yonnet[23]) indicate that $<\epsilon T_{11}^2>^{1/2} = 0.017$ and large values of T_{22} and T_{21} at 1.6 GeV. Tests of such a device are expected to occur in 1995.

7 Conclusions

In the last 20 years polarimeters have been developed to measure the polarization of protons and deuterons emitted in nuclear reactions with energies in the range 100 MeV to 2.4 GeV. These instruments have been calibrated and, for designs with 2π azimuthal acceptance, these calibrations have been found to be universal to the level of 3-5% accuracy up to 800 MeV. Carbon polarimeters have large vector analyzing power for deuterons up to at least 700 MeV. Use of hydrogen and coincidence detection will extend the range of application for deuterons to at least 2 GeV.

The interference nature of polarization opens a large number of vistas, when an interesting but small amplitude can be measured because it "beats" against a large amplitude. The program in hall A at CEBAF is expected to receive great strength from its polarimeter.

The author wishes to express his gratitude to Drs. Vina Punjabi, Mark Jones and Naipor Cheung for helpful discussions and careful reading of the manuscript.

Appendix

The Saclay proton analyzing power data from 800 MeV to 2.4 GeV have been fitted with a new 14-parameters expression which better corresponds to the natural shape of these distributions. The expression used is as follows:

$$A_p^C(\theta, p_{mid}) = a\, x^r \exp^{-bx} + c\, x^s \exp^{-dx}$$

where $x = p_{mid} \sin\theta$

p_{mid} is momentum at center of Carbon

$$a = a_0 + a_1 p' + a_2 p'^2$$

$$b = b_0 + b_1 p' + b_2 p'^2$$

$$c = c_0 + c_1 p' + c_2 p'^2$$

$$d = d_0 + d_1 p' + d_2 p'^2$$

$$r = r_0 \quad , \quad s = s_0,$$

where $p' = p_{mid} - 2.3GeV$.

Table 1 Optimum values for the 14 parameter fit of the inclusive pC analyzing power data (ref. 2).

	0	1	2
a	5758±6665	-9910±12289	4543±5997
b	26.45±3.14	-7.018±1.957	-3.448±1.399
c	6.015±3.029	-4.492±2.855	3.654±2.564
d	4.676±0.561	-0.2947±0.2357	0.6398±0.3732
s	2.066±0.321		
r	3.869±0.419		

References

1) C.F. Perdrisat et al, *to be pub. in Rev. Sc. Inst.*

2) N.E. Cheung et al , submitted to NIM in Phys.Res. (1994)

3) C.F. Perdrisat, V. Punjabi and hall A collaboration, *CEBAF* **93-027**

4) J.M. Finn, P. Ulmer and hall A collaboration;, *CEBAF* **89-028**

5) R. Ent P. Ulmer and J.F.J. Brand, *CEBAF* **93-049**

6) S. Co and al., *CEBAF* **94-018**

7) M. Garçon et al. *Phys. Rev.* **C**, (1994) 2516

8) V. Punjabi et al, *submitted to Phys. Rev. Lett.* (1994)

9) D. Aebisher et al *NIM* **124** (1975) 49

10) G. Waters et al *NIM* **153** (1978) 401

11) R.D. Ransome et al *NIM* **201** (1982) 315

12) M.W. McNaughton et al *NIM* **241** (1985) 435

13) E. Aprile-Giboni et al *NIM* **215** (1983) 147

14) B. Bonin et al. *NIM in Phys. Res.* **A288** (1990) 379

15) DOE grant to University of Virginia.,
and NSF grant to College of William & Mary

16) H. Baghei et al, *Calibration report, unpublished*, and Lourie et al, *private communication*

17) NSF grant to Rutgers University and College of William and Mary (1992)

18) J. Bystricky et al. *Lett. Nuov. Cim.* **40**, (1984) 466

19) C. Ohmori et al *Phys. Lett.* **B243** (1990) 29.

20) H. Spinka et al. *NIM* **211** (1983) 239

21) B. Bonin et al. *NIM in Phys. Res.* **A288** 389 (1990) 239

22) S. Cox et al, *to be published in NIM in Phys. Res.* (1994)

23) E. Tomasi-Gustaffson and J. Yonnet, *private communication* (1994).

Polarized Photons for Nuclear and Particle Physics

Blaine E. Norum
Department of Physics, Univiersity of Virginia, Charlottesville, VA 22901
(June 19, 1995)

Polarized or unpolarized γ's in the energy range of a few MeV to many GeV are produced using one of two methods: by Bremstrahlung radiation emitted when electrons strike a target or by Compton scattering of low energy photons from extremely relativistic electrons. Both methods can produce either linearly or circularly polarized γ's but other characteristics of the γ beams produced by the two methods differ substantially. The characteristics of beams produced by each method, the parameters of facilities using each method, and the expected capabilities of newly proposed facilities are discussed.

I. INTRODUCTION

The growing appreciation of the importance of understanding the polarization aspects of photon interactions with nuclei and nucleons has led to the development and refinement of many techniques for producing polarized photons. The need to have access to both linearly and circularly polarized photons necessitates the use of varied approaches. The production of high energy photons starts with an electron beam and the availability of accelerators capable of delivering suitable beams demands further flexibility. However, the interest in gaining access to the polarization degrees of freedom has been sufficiently intense to generate an impressive number of viable options.

The parameters of importance when evaluating a particular source of polarized photons include the γ energy, the flux, the polarization, the tagging efficiency (in the case of tagged beams), the levels of associated backgrounds of all kinds, the ease with which systematic erros can be controlled, and the γ energy resolution. No one approach can simultaneously be optimimal with respect to all of these concerns. Consequently, a variety of approaches must be pursued.

The two basic means of producing high energy γ's are by bremstrahlung radiation when an electron beam strikes a target or radiator and by the Compton backscattering of light from an electron beam. Each will be discussed in turn, after which a compendium of representative parameters will be presented, and conclusions drawn.

II. POLARIZED BREMSTRAHLUNG SOURCES

The most widely used source of high energy γ's for nuclear and particle physics is the bremstrahlung radiation emitted when an electron beam strikes a target. The cross section [1] for the process is large so a usable flux of γ's can be produced by a low intensity beam and a thin target or radiator. Photons with energies from zero up to the energy of the electron beam are emitted in a cone centred on the electron beam direction and with a characteristic opening angle of $1/\gamma$, where γ is the relativistic gamma factor for the electrons. The energies of individual γ's are "tagged" by measuring the energy of the electron which emitted the γ. The principle advantage of a bremstrahlung source is that it can produce a high flux limited only by the rate at which the electrons can be tagged and that the equipment required is a straightforward addition to an existing electron accelerator facility. A principle disadvantage of a bremstrahlung source is that the cross for bremstrahlung radiation diverges towards low energies so the γ spectrum is dominated by low energy photons when typically the photons of interest have higher energies. It is not possible to detect electrons with energies either very near zero or very near the beam energy so there is a significant flux of untagged high and low energy photons in the γ beam produced. In addition, when the electron beam strikes a target processes other than bremstrahlung radiation can occur. These can generate secondary radiation that constitutes an undesirable background for an experiment.

The bremstrahlung radiation emitted along the electron beam direction when an unpolarized beam strikes an amorphous or non-aligned target is itself unpolarized. Bremstrahlung emitted at an angle to the electron beam, or emitted by a polarized electron beam, or produced in an aligned crystalline target possesses a finite degree of polarization. Each of these conditions is being used to generate polarized photons.

A. Off-Axis Bremstrahlung

The existence of finite linear polarization in the bremstrahlung radiation emitted in directions other than that of the electron beam was first noted by Bethe and Heitler [1]. However, determining the polarization of γ's emitted in a particular direction requires precise knowledge of the direction of the emitted photon and that of the recoiling electron. Recently, the technique has been investigated at the Saskatchewan Accelerator Laboratory (SAL) and found to promise a $\vec{\gamma}$ beam with very reasonable polarization properties. [2] Figure 1 shows the degree of polarization for 50 MeV γ's emitted by a 100 MeV electron beam at horizontal angles $theta(k)$ and vertical angles $phi(k)$ with respect to the initial electron beam direction when the final electron direction is constrained to lie between ± 25 mrad in the horizontal plane and between 0 mrad and 10 mrad in the vertical plane. Regions in which the polarization exceeds 50% are clearly seen.

The principle advantage of this technique is that it is reasonable easy to implement. Collimators can be used to define both the final electron and emitted γ directions. One disadvantage is that the polarization is a complex and sometimes rapidly varying function of the angles involved. Another disadvantage is that changing the direction of polarization entails moving and accurately repositioning a collimator.

B. Coherent Bremstrahlung

A second very effective technique for producing linearly polarized γ's is through the use of a precisely aligned crystalline target. Interference effects in the cross section for production of bremstrahlung radiation from planes of a single crystal were first calculated by Überall [3]. He also showed that for selected energies the γ's could have a high degree of polarization. [4] Experiments and theoretical refinements followed until by the late 1960's the process was well understood [5].

The bremstrahlung emitted from an oriented crystal has two components: coherent and incoherent. The incoherent contribution parallels the spectrum obtained using an amorphous target and is a smoothly varying function of γ energy. The coherent contribution, by comparison, is a complex, sharply peaked function of the γ energy. Figure 2(a) taken from reference [6] shows the spectrum of photons emitted from a diamond radiator placed in the 855 MeV beam of the MAMI accelerator of the University of Mainz. The agreement between theory and experiment is clearly excellent, generating confidence that despite the complexity of the energy dependence of the polarization it can be accurately calculated.

The maximum degree of polarization shown in fig. 2(b) is only 30%. However, it was noted that by collimating the γ beam the degree of maximum degree of polarization could be increased, albeit at the expense of reduced tagging efficiency and reduced energy range over which the polarization is significant. Figure 3 also taken from reference [6] shows the effects of collimation on both the intensity and the polarization characteristics of the γ beam.

The principal advantage of this technique is the high degree of polarization that can be attained and the fact that both the intensity and polarization are sensitive to the same parameters. As a result, one can monitor the stability of the polarization by monitoring the intensity of the beam. It is also reasonable inexpensive to install. Changing the direction of polarization requires changing the orientation of the crystal so precise calibration is difficult. However, it has been shown that the polarization can be measured and monitored at the $\pm$ 2% level. [7] In comparison with most of the Compton backscattering sources to be discussed later this technique also has the advantage when the electron energy is below a few GeV of producing polarized γ's with energies of a larger fraction of the electron energy. However, it has the disadvantages that only a small fraction of the γ beam is polarized and, in common with all bremstrahlung sources, that there are many untagged γ's as well as other background radiation generated.

This technique is also being pursued at CEBAF.

C. Circular Polarization from Polarized Electrons

Several of the most interesting experiments being planned in the field of photonuclear physics require circularly polarized γ's. The previously discussed techniques can produce linear polarization but not circular polarization. To produce circular polarization using the bremstrahlung radiation process one requires circularly polarized photons but no special radiator. When an electron beam with longitudinal polarization P_{el} strikes a radiator the circular polarization (P_{circ}) of the emitted bremstrahlung is given to first approximation by:

$$P_{circ} = P_{el}\left(4x - x^2\right) / \left(4 - 4x + 3x^2\right) \quad (1)$$

where $x = k/E_0$, k is the emitted photon energy, and E_0 is the initial electron energy. The polarization scales with the electron polarization so the recent development of polarized electron sources (using strained GaAs crystals) capable of 85% polarization makes this technique extremely attractive. Screening of the field of the nucleus by the atomic electrons and collimation of the emitted γ beam produce minor corrections. Figure 14 taken from reference [8] shows the γ polarization and the influence of these effects. Unlike the case of linearly polarized coherent bremstrahlung the polarization in this case peaks at the maximum energy. The smooth variation with energy is also clearly seen.

Several laboratories are preparing to use this technique: Mainz, Bonn, and CEBAF.

III. COMPTON BACKSCATTERING

The use of Compton scattering of light from high energy electrons as a means of producing high energy, polarized photons was first suggested in 1962 by R. H. Milburn [9] and by F. R. Arutyunian *et al.* [10] Since then the technique has been employed at many laboratories: CEA, [11] the Lebedev Institute, [12] SLAC, [13] and Brookhaven (LEGS). [14,15] Accordingly, the basic theory and practice are well established.

The principal advantages of this technique over others for producing polarized photons are:

- Polarization: The degree of polarization in the uppermost 20% of the spectrum exceeds 90% (80%) for linearly (circularly) polarized photons. The γ polarization is given by the product of the laser photon polarization and a smoothly varying function of the γ energy. Laser polarization is extremely stable and can be monitored on-line. The smooth dependence on γ energy further reduces possible systematic uncertainties. Finally, the polarization of the laser (and hence the γ beam) is easily and quickly reversed (in the case of circular polarization) or rotated (in the case of linear polarization) with *no change in the geometry of either the electron or γ beam.* The direction of linear polarization can be varied smoothly and easily over the entire range, thus reducing significantly systematic uncertainties arising from other components of the experimental system.

- Tagging Efficiency: The kinematics of Compton scattering place a firm upper limit on the energies of the γ's produced. Accordingly, there are no untagged high energy γ's. Compton scattering is a two-body scattering process so there exists a correlation between the γ energy and γ emission angle. A collimator limiting the γ angle places a lower limit on the energy of transmitted γ's. Thus, the energies of the transmitted γ's can be firmly restricted.

- Backgrounds: There is no material target in the path of the electron beam so the principal sources of backgrounds associated with Bremstrahlung photon beams are eliminated. Low energy Bremstrahlung emitted parallel to the electron beam is absent. Secondary radiation produced when either scattered electrons or recoiling nuclei strike the vacuum chamber is similarly eliminated. The remaining source of background is Bremstrahlung from residual gas in the beam line. In all applications of interest here this contribution is negligible.

The only serious limitation to this technique is that for electron energies below tens of GeV and near-visible laser photons the maximum energy of the γ's produced is significantly less than that of the electron beam.

A. Basic Process

When a photon of energy E_{laser} collides head on with an electron of energy E_{beam} and is scattered backwards, emerging at an angle θ_γ with respect to the incident electron energy, its energy is given by

$$E_\gamma = \frac{E_{laser}\,(E_{beam} + P_{beam})}{E_{beam} + E_{laser} - (P_{beam} - E_{laser})\cos\theta_\gamma} \tag{2}$$

$$\approx \frac{4\gamma^2 a E_{laser}}{[1 + a(\gamma\theta_\gamma)^2]} \tag{3}$$

where

$$a = \left[1 + \frac{4\gamma E_{laser}}{m_e}\right]^{-1}, \tag{4}$$

$$\gamma = E_{beam}/m_e, \text{ and} \tag{5}$$

$$m_e = \text{electron rest mass.} \tag{6}$$

The maximum achievable γ energy (E_γ^{max}) for intermediate energies and available laser energies is shown in figure 4.

The cross section for Compton scattering under the conditions being considered is given (in the laboratory frame) by

$$\frac{d\sigma}{dE_\gamma} = \frac{2\pi r_e^2 a}{E_\gamma^{max}} \left(\frac{\rho^2 (1-a)^2}{1-\rho(1-a)} + 1 + \left[\frac{1-\rho(1+a)}{1-\rho(1-a)} \right]^2 \right) \tag{7}$$

where r_e is the classical radius of the electron (= 2.818 fm) and $\rho = E_\gamma / E_\gamma^{max}$. The dependence of the cross section upon γ energy is shown, again for representative conditions, in figure 6. It is significant that the cross section is flat to within a factor of two across the entire energy range; the low energy divergence characteristic of Bremstrahlung beams is conspicuously absent.

The polarization of the γ beam (P^γ) is proportional to that of the laser beam (P^{laser}) and is a function of ρ and a as defined above. For the case of linear polarization

$$\left| \frac{P^\gamma}{P^{laser}} \right| = \frac{(1-\cos\theta_0)^2}{2\left[\kappa + 1 + \cos\theta_0{}^2\right]} \tag{8}$$

and for the case of circular polarization

$$\left| \frac{P^\gamma}{P^{laser}} \right| = \frac{[\kappa+2]\cos\theta_0}{2\left[\kappa + 1 + \cos\theta_0{}^2\right]} \tag{9}$$

where

$$\kappa = \frac{\rho^2 (1-a)^2}{1-\rho(1-a)} \text{ and} \tag{10}$$

$$\cos\theta_0 = \frac{1-\rho(1+a)}{1-\rho(1-a)}. \tag{11}$$

The dependence of the γ polarization upon γ energy is shown, again for representative conditions, in figure 7. The very high polarization at the maximum γ energy is clearly shown.

B. Facilities

As the Compton scattering cross section is relatively small a high luminosity is required in the photon-electron collision region. The power of typical lasers is limited to a few tens of watts so an intense electron beam is required to achieve a useful γ flux. Electron storage rings such as the X-ray ring of the National Synchrotron Light Source (NSLS) are the most accessible source of such intense electron beams.

The only currently operational $\vec{\gamma}$ source based on Compton backscattering is the Laser-Electron Gamma Source (LEGS) which uses the X-ray ring of the NSLS [14,15] located at Brookhaven National Laboratories (BNL). Light from a laser is collided with the stored beam in a straight section of the ring. The dipole magnet directly following this straight section is used to momentum analyze the electrons which give up significant fractions of their momenta in collisions with photons. When the electron energy is maintained at 2.58 GeV (2.80 GeV) electrons corresponding to emitted γ's with energies down to 185 MeV (200 MeV) can be "tagged."

The parameters of the LEGS beam are shown in Fig. 8. [16] The total flux is restricted to 6×10^6 γ/s so that the electron current in the ring will not be depleted too rapidly. Note that by using a combination of electron and laser energies γ polarization can be maintained at above 85% for all tagged energies. The physics program at LEGS is currently focused on the study of the spin structure of the nucleon, in particular the measurement of the Spin-Polarizability [17] and Drell-Hearn-Gerasimov [18,19] Sum Rules.

Three additional $\vec{\gamma}$ sources based on synchrotron radiation storage rings are currently under development. The Grenoble Anneau Accélérateur Laser (GRAAL) is located at the European Synchrotron Radiation Facility (ESRF) in Grenoble, France. The energy of the stored electrons is 6 GeV so γ energies of about 1.5 GeV (1.8 GeV) will be attainable using a laser wavelength of 351 nm (252 nm). Tagging the γ's by detecting the recoiling electron will be accomplished in the same manner as at LEGS. An energy resolution of the order of 15 MeV is expected. Similar to the case of LEGS, the γ flux will be limited by the rate of electron beam loss to about 10^7 γ/s. The $\vec{\gamma}$ facility is expected to be operational in the latter part of 1995 and will initially be used to study various channels of strangeness

photoproduction. It will also be used to measure the higher energy contributions to the Spin-Polarizability [17] and Drell-Hearn-Gerasimov [18,19] Sum Rules, complementing the measurements to be performed at LEGS.

Another $\vec{\gamma}$ facility based at a synchrotron radiation facility is being pursued at the SPring-8 [20] facility currently under construction at the Harima Science Garden City, Hyogo, Japan. The electron energy in the SPring-8 storage ring will be 8 GeV so $\vec{\gamma}$ energies of up to 2.4 GeV (3.0 GeV) will be possible using a laser wavelength of 351 nm (252 nm). Design studies predict an energy resolution of 20 MeV. Here again, the $\vec{\gamma}$ flux is expected to be limited by electron loss rates. The storage ring is scheduled to be commissioned in 1997 and the $\vec{\gamma}$ facility to be operational somewhat later.

A third $\vec{\gamma}$ facility based on the VEPP-4 electron storage ring of the Institute for Nuclear Physics in Novosibirsk, Russia is also being developed. [21] With an electron energy of 5 GeV, $\vec{\gamma}$ energies of up to 1.4 GeV are expected. The flux, which will be limited by the possible tagging rate rather than by either laser power or electron depletion rate, is expected to be less than 10^{-6}/s.

IV. NEW IDEAS FOR INTENSE $\vec{\gamma}$ SOURCES

With the growing appreciation within the community of the interesting physics that can be addressed with high quality $\vec{\gamma}$ beams there is a corresponding drive to develop sources with increased energy, increased flux, improved energy resolution, etc. Bremstrahlung radiation sources are limited by large backgrounds and the strong energy dependence of the polarization. Sources based on Compton scattering from the stored beam at a synchrotron radiation facility are limited by low fluxes and low γ energies (relative to the electron energy); for some experiments the modest energy resolution is also a constraint. Recently, however, two projects have been proposed which promise to circumvent at least some of these limits.

The new projects are both based upon Compton scattering. The first [22] involves the use of a resonant optical cavity to increase greatly the intensity of the laser light incident on an electron beam. Consequently, an electron beam of only a few μAmps is required to obtain a high flux. It is proposed to place such a cavity in the electron beam in Hall B at CEBAF. The second [23] involves reflecting the UV radiation produced by one bunch of electrons in the Duke Free Electron Laser Laboratory (DFELL) electron storage ring back against a second bunch in the same ring. The resultant γ beam will be very intense and, due to the relatively high energy of the initial UV photons, it will have an energy that is a substantial fraction of the initial electron energy.

A. CEBAF Hall B Compton $\vec{\gamma}$ Source

In order to obtain a reasonable flux of tagged γ's using an electron beam current of the order of μA's it is necessary to obtain a very high incident photon flux. The proposed means of achieving such a high flux is a resonant cavity in which the photons from a laser are stored. In one sense, the proposed system is the mirror image of the LEGS system. At LEGS, photons of a relatively low intensity laser beam interact once with a high intensity electron beam (achieved by storing in a ring). At CEBAF, electrons of a relatively low intensity electron beam will interact once with a high intensity photon beam (achieved by storing in a resonant cavity).

A conceptual view of the proposed system is shown in figure 15. The optical cavity is configured to focus the beam at the cross-over point where the electron beam intersects it. This tight focusing enables one to achieve high luminosity despite the very short interaction region. In addition, the geometry permits the use of multiple lasers to increase the flux further.

Resonant cavities are an established technology in atomic and molecular physics. [24] Essentially, a cavity consists of four highly reflective ($R = 0.99999^{+}$), very low-loss mirrors configured to form a "figure-8" for which the total path length is an integral number of wavelengths of the light to be stored. Light (single frequency, possibly multi-mode) from a laser is directed along one axis towards the rear side of one of the mirrors. Initially, a small fraction of the light is transmitted (T = 1-R) while most is reflected. As the initially transmitted light completes a cycle of the cavity and strikes the first mirror again a small fraction (T_1) of it is transmitted out of the cavity and can interfere with the reflected portion of the incident laser light. If the phase difference between the transmitted light from the cavity and the reflected light from the laser can be made to equal $(2n+1)\pi$, then these two waves will destructively interfere; that is, the amount of laser light that is reflected will be reduced. Correspondingly, if the phase difference between the light transmitted into the cavity and the light already in the cavity is $2m\pi$, then the two will interfere constructively and the amount transmitted into the cavity will be increased. The stored power will increase until the rate at which light is transmitted into the cavity equals the rate at which light is lost due to absorption in the mirrors, diffraction

from imperfections, scattering from gas, etc. The "filling time" or, conversely, the "emptying time" for a cavity such as that proposed is of the order of 10's of milliseconds, permitting rapid change of the polarization.

In the proposed system the cavity will be approximately 1 m long. It will be fed through one of the upstream mirrors by a (nominally) 10 W Ar-ion laser (λ = 513 nm). The small flux of photons transmitted through a downstream mirror will be used to monitor polarization and flux, with the latter information being used in a feedback system to control the mirror alignment and positioning. Cavities of this type currently achieve stored power levels 30,000 times those of the lasers feeding them. Recently, mirrors with R $\approx$ 0.999999 for 513 nm light have become available [25] so higher gains appear possible.

The small laboratory-frame angles at which the light beams strike the electron beam transform into infinitesimal angles in the electron rest frame so the collisions can be regarded as being head-on. In addition, the divergence of the electron beam is small so the energy of a γ is strongly correlated to the emission angle with respect to the nominal electron direction. The size of the γ beam spot at the center of the CLAS is shown in figure 9. The angles at which the γ's of interest are emitted are extremely small; the changes in the direction of motion of the "recoiling" electrons are even smaller. Therefore, all electrons, regardless of their energies, enter the tagging spectrometer within an extremely narrow cone. Consequently, their energies can be determined simply by measuring their positions as they exit the magnet *without* relying on the focusing properties of the magnet. With an electron beam energy of 4.0 GeV the energy of a 500 MeV γ can be measured to within approximately 1 MeV through the use of a new, more finely segmented detector.

The attainable γ flux can be computed from a) the electron beam power, b) the laser power ($n_{laser} \times 10$ W), the cavity gain (30,000), and d) the laser wavelength (513 nm). It would appear that the flux could be increased arbitrarily by increasing the electron current, but the beam dump capacity currently limits the electron beam power to 10 kW. Representative results are shown in figures 10.

B. TUNL/DFELL Compton $\vec{\gamma}$ Source

The Duke Free Electron Laser Laboratory currently has an operational electron storage ring capable of storing beams at energies up to about 1.2 GeV. With an undulator magnet and related optics placed along one side it will form the basis for a free electron laser (FEL) capable of generating intense, coherent radiation at photon energies up to 12.5 eV. The intensity of the radiation produced in an FEL is roughly proportional to the square of the charge in the bunch producing it so the ring would normally operate with a single electron bunch. However, a second bunch following the first by slightly less than twice the distance from the undulator to the downstream optical cavity mirror (see Fig. 11) will collide with the light stored in the cavity and produce γ's polarized in the direction of the undulator fields (see Fig. 12 taken from reference [23].

Total tagging rates at current and planned tagged photon facilities are limited typically to about 10^7-10^8 Hz for bremstrahlung and the CEBAF Hall B Compton sources or about 10^6-10^7 Hz at Compton sources based on synchrotron radiation facilities. For those measurements in which obtaining data for a wide range of photon energies is the goal (e.g., sum rule measurements) these rates are satisfactory. For measurements where it is more important to have high statistics over a narrower (few percent) energy range the useful flux is less than 10^5-10^6Hz. At the TUNL/DFELL source extremely high fluxes will be possible due to the very high high intensity of the FEL radiation. As a result, it will be possible to make use of the close energy-angle correlation by collimating the beam to restrict the $\vec{\gamma}$ energies to a narrow range while still transmitting a very high flux. When the design current of 1 A is stored in the ring transmitted $\vec{\gamma}$ fluxes of about 10^8 Hz will be possible. It should be noted that such high fluxes will result in a very rapid depletion of the stored electron current. Thus, the $\vec{\gamma}$ source will require dedicated of the ring. Current projections are for 1000 hours per year of dedicated running.

Figure 13 shows a typical energy spectrum of a beam transmitted by a collimator of radius 1 mm located 50 m from the photon-electron collision point. Table ?? shows the $\vec{\gamma}$ beam parameters under representative conditions. The TUNL/DFELL source will be well suited to measurements of near-threshold pion production, polarizabilities, etc. Its only serious limitation is that the polarization of the $\vec{\gamma}$ beam cannot be easily varied, thus making control of systmatic uncertainties critical. Planning of the facility is well underway and initial measurements of the Compton scattering of FEL radiation is planned for Fall 1995.

V. FACILITY COMPARISON

It is impossible to compare directly in a meaningful way facilities that differ in energy by an order of magnitude and for which the experimental requires differ even more. The significance of factors such as levels of background,

the energy range over which the polarization is large, the existence of untagged low and high energy photons, and the energy resolution of $\vec{\gamma}$ beam depends upon the details of individual experiments. Consequently, we list in Table I only representative parameters.

It must be noted that parameters such as the photon energy resolution depend upon the energy of operation so the numbers given here will vary. In the case of the coherent bremstrahlung sources the maximum polarization and tagging efficiency are inversely related and can be varied to suit the needs of a particular experiment. In the case of the TUNL source, the beam is not tagged so that space is left blank. Finally, the expected energy resolution of the ROKK-2 source was not known at the time this table was prepared.

VI. CONCLUSIONS

We are at the beginning of an exciting period in the field of photonuclear physics. A wide variety of polarized γ facilities are either operational, under construction, or in the planning stages. The parameters of these beams vary widely, but the field is broad enough (and the counting rates low enough!) to require them all.

---

[1] H. A. Bethe and W. Heitler, Proc. Roy. Soc. **A146**, 83 (1934).
[2] J. Asai, private communication, 1994.
[3] H. Uberall, Phys. Rev. **103**, 1055 (1956).
[4] H. Uberall, Z. Naturforsch **17a**, 332 (1962).
[5] G. Lutz, Nuovo Cimento **53**, 242 (1968).
[6] D. L. *et al.*, Nucl. Instrum. Meth. **A343**, 494 (1994).
[7] R. Beck, private communication, 1994.
[8] Z. L. *et al.*, Helicity Structure of Pion Photoproduction on Polarized Deuterium and the GDH Sum Rule for the Neutron, unpublished, 1994.
[9] R. H. Milburn, Phys. Rev. Lett. **10**, 75 (1963).
[10] F. R. Arutyunian, I. I. Goldman, V. A. Tumanian, and Z. Eksperim, Soviet Physics, JETP **18**, 1964 (1964).
[11] C. Bensporad, R. H. Milburn, N. Tanaka, and M. Fotino, Phys. Rev. B **138**, 1548 (1965).
[12] O. F. Kulikov, Y. Y. Telnov, E. I. Filippov, and M. N. Yakimenko, Phys. Lett. **13**, 344 (1964).
[13] J. J. Murray and P. R. Klein, SLAC-TN-67-19 **19**, 1 (1967).
[14] A. M. Sandorfi *et al.*, IEEE **NS-30**, 3083 (1983).
[15] C. E. Thorn *et al.*, Nucl. Instrum. Meth. **A285**, 447 (1989).
[16] A. M. Sandorfi, LEGS Biennial Progress Report, unpublished, 1994.
[17] V. Bernard, N. Kaiser, J. Kambor, and U.-G. Meissner, Nucl. Phys. **B388**, 315 (1992).
[18] S. D. Drell and A. C. Hearn, Phys. Rev. Lett. **16**, 908 (1966).
[19] S. B. Gerasimov, Sov. J. Nucl. Phys. **2**, 430 (1966).
[20] M. H. *et al.*, in *Proceedings of the Fourth European Particle Accelerator Conference*, European Physical Society (World Scientific, London, England, 1994).
[21] V. Litvinenko, private communication, 1995.
[22] B. E. Norum and T. P. Welch, An Intense Polarized Photon Source for CEBAF Hall B, unpublished, 1993.
[23] T. S. Carman *et al.*, Production of Gamma-Rays for Nuclear Physics Using the Duke Free-Electron-Laser Facility, TUNL Technical Report, 1995.
[24] A. E. Siegman, *An Introduction to Lasers and Masers* (McGraw-Hill, New York, NY, 1971).
[25] R. Lelazari, (Particle Measuring Systems, Boulder CO) private communication.
[26] A. M. Sandorfi, private communication, 1993.
[27] T. R. Kezepambnjn, in *Electromagnetic Interactions of Nuclei*, Proceedings of the 8^{th} Seminar (NEP, Novosibirsk, Russia, 1992).
[28] T. Tamae, private communication, 1994.
[29] R. Beck, private communication, 1993.
[30] G. Anton, private communication, 1994.
[31] B. Berman, private communication, 1994.
[32] E. Hallin, private communication, 1993.

Facility	Technique	Pol. Type	E_γ^{max} [MeV]	Flux [kHz/MeV]	P_γ	Tag. Eff.	ΔE_γ [MeV]
LEGS [26]	Compton	Both	333	33	1.0	1.0	5.0
GRAAL [26]	Compton	Both	1800	6	1.0	1.0	15.0
ROKK-2 [27]	Compton	Both	1400	1	1.0	1.0	
Spring-8 [28]	Compton	Both	3000	1	1.0	1.0	20.0
CEBAF [22]	Compton	Both	1800	50	1.0	1.0	1.0
TUNL [23]	Compton	Lin.	220	10000	1.0		0.8
Mainz [29]	Coh. Brem.	Lin.	400	50	0.4	0.5	2.0
Bonn [30]	Coh. Brem.	Lin.	1200	10	0.4	0.5	10.0
CEBAF-B [31]	Coh. Brem.	Lin.	1800	50	0.4	0.5	10.0
SAL [32]	Off Brem.	Lin.	87	6000	0.4	0.4	0.6
Mainz [26]	$\vec{e}$ Brem.	Circ.	840	50	0.8	0.5	2.0
Bonn [30]	$\vec{e}$ Brem.	Circ.	2400	5	0.8	0.5	10.0
CEBAF [8]	$\vec{e}$ Brem.	Circ.	6000	2	0.8	0.5	20.0

TABLE I. Representative parameters of existing and planned polarized photon sources. As described in the text many of the parameters vary with operating energy. Listed parameters are representative of conditions when highest possible photon energy is produced. Note that the TUNL beam will be untagged.

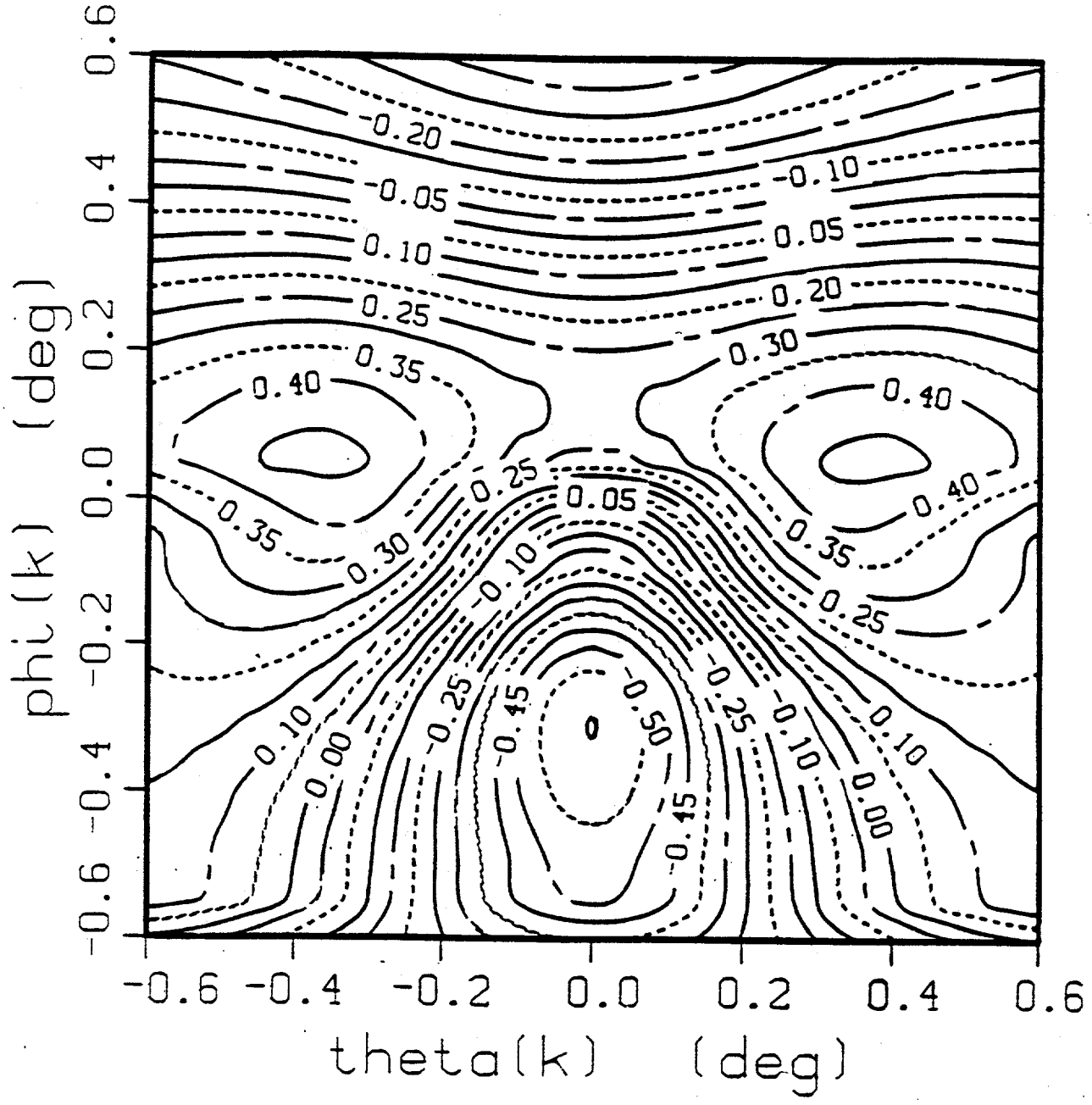

FIG. 1. Polarization of 50 MeV γ's emitted by a 100 MeV electron beam at horizontal angles *theta*(k) and vertical angles *phi*(k) with respect to the initial electron beam direction when the final electron direction is constrained to lie between ± 25 mrad in the horizontal plane and between 0 mrad and 10 mrad in the vertical plane.

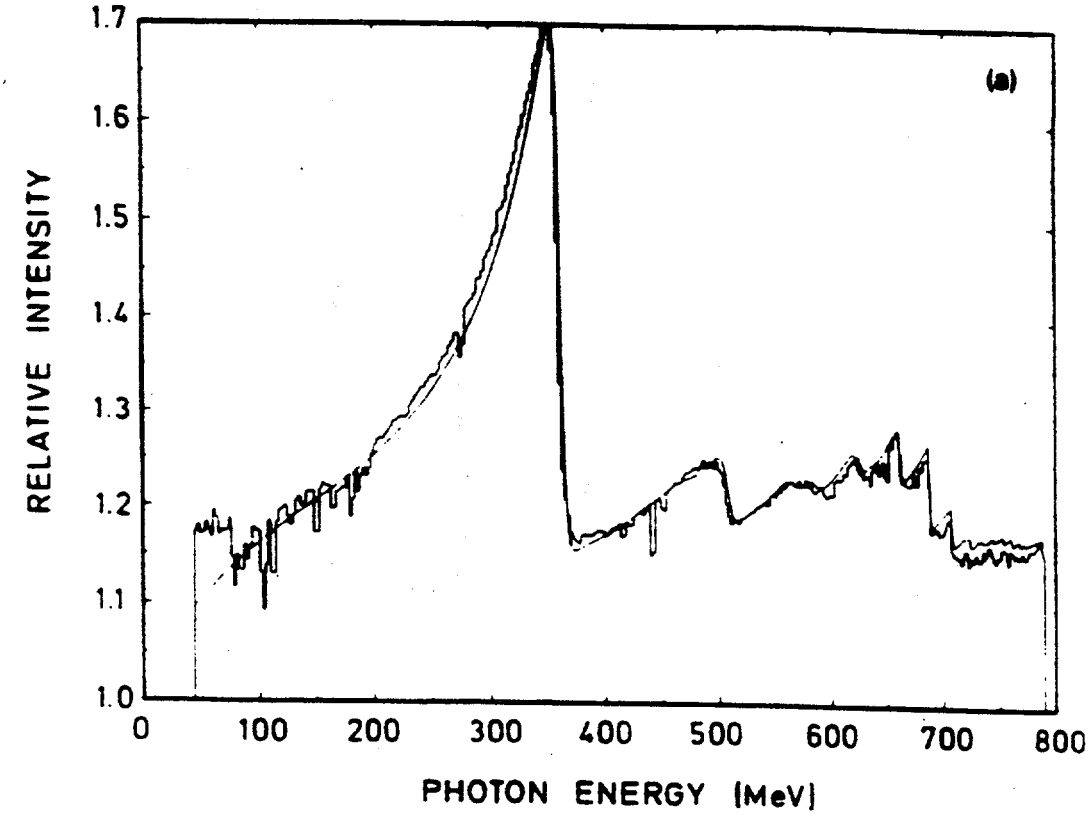

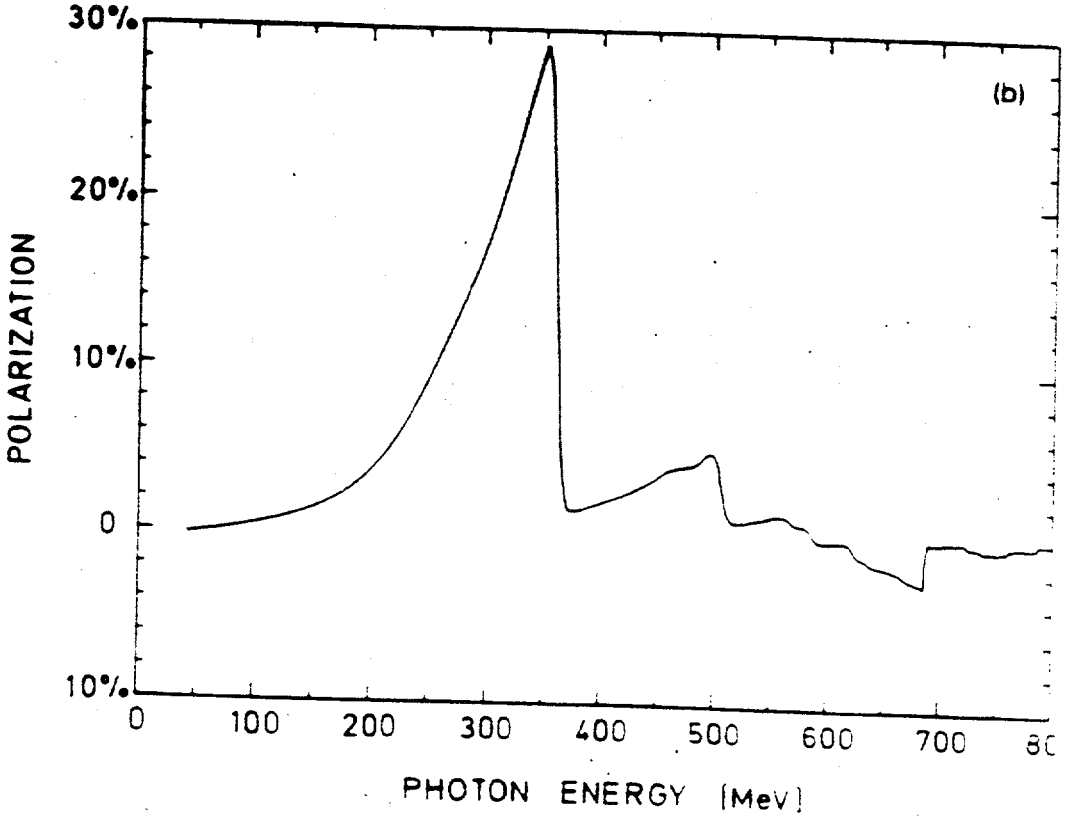

FIG. 2. (a) Relative intensity of coherent and incoherent bremstrahlung $(I_{incoh} + I_{coh})/I_{incoh}$ emitted from a diamond radiator in the 855 MeV beam of the MAMI accelerator. The histogram represents the measured results and the solid curve the calculated result. (b) Degree of linear polarization calculated using the same formalism as was used in (a).

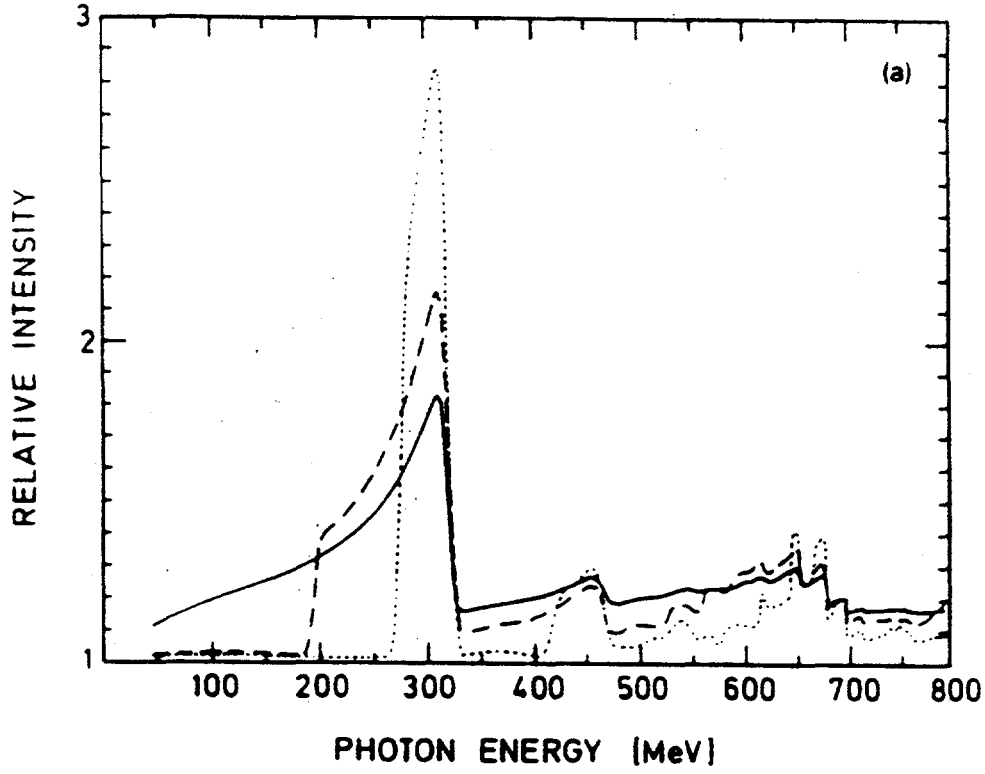

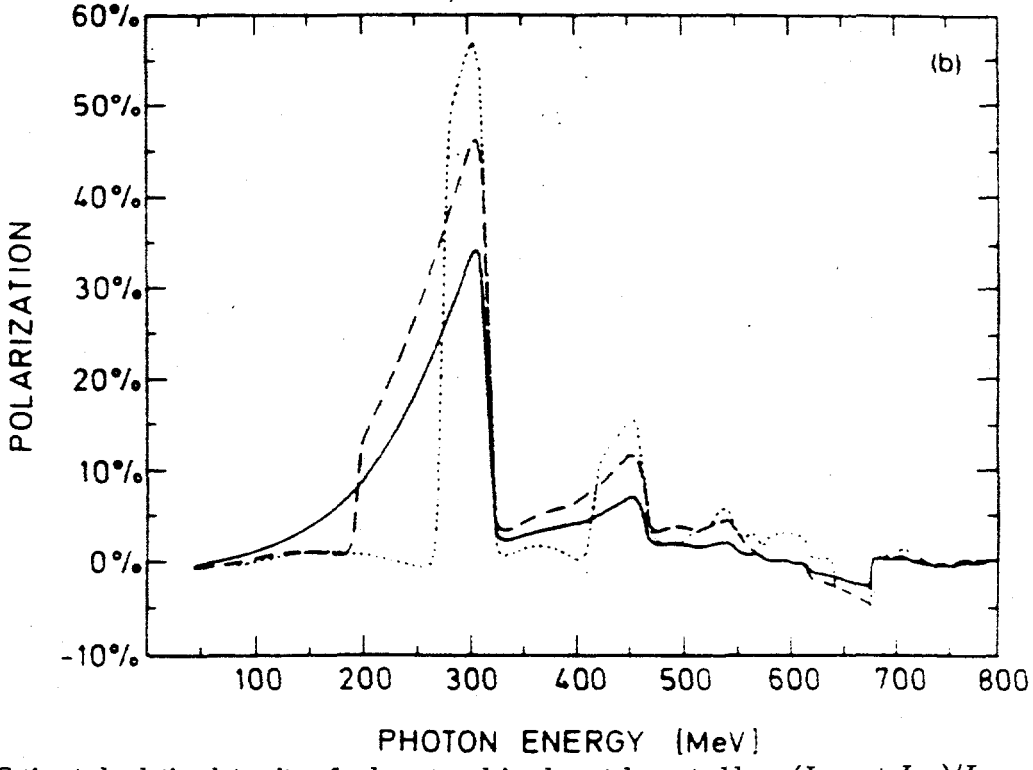

FIG. 3. (a) Estimated relative intensity of coherent and incoherent bremstrahlung $(I_{incoh} + I_{coh})/I_{incoh}$ emitted from a diamond radiator in the 855 MeV beam of the MAMI accelerator for varying degrees of collimation. The solid (dashed, dotted) line corresponds to no ($\theta_{coll} = \theta_c, \theta_{coll} = \theta_c/2$) collimation. $\theta_c = m_e/E_0$. (b) Degree of linear polarization calculated using the same formalism as was used in (a).

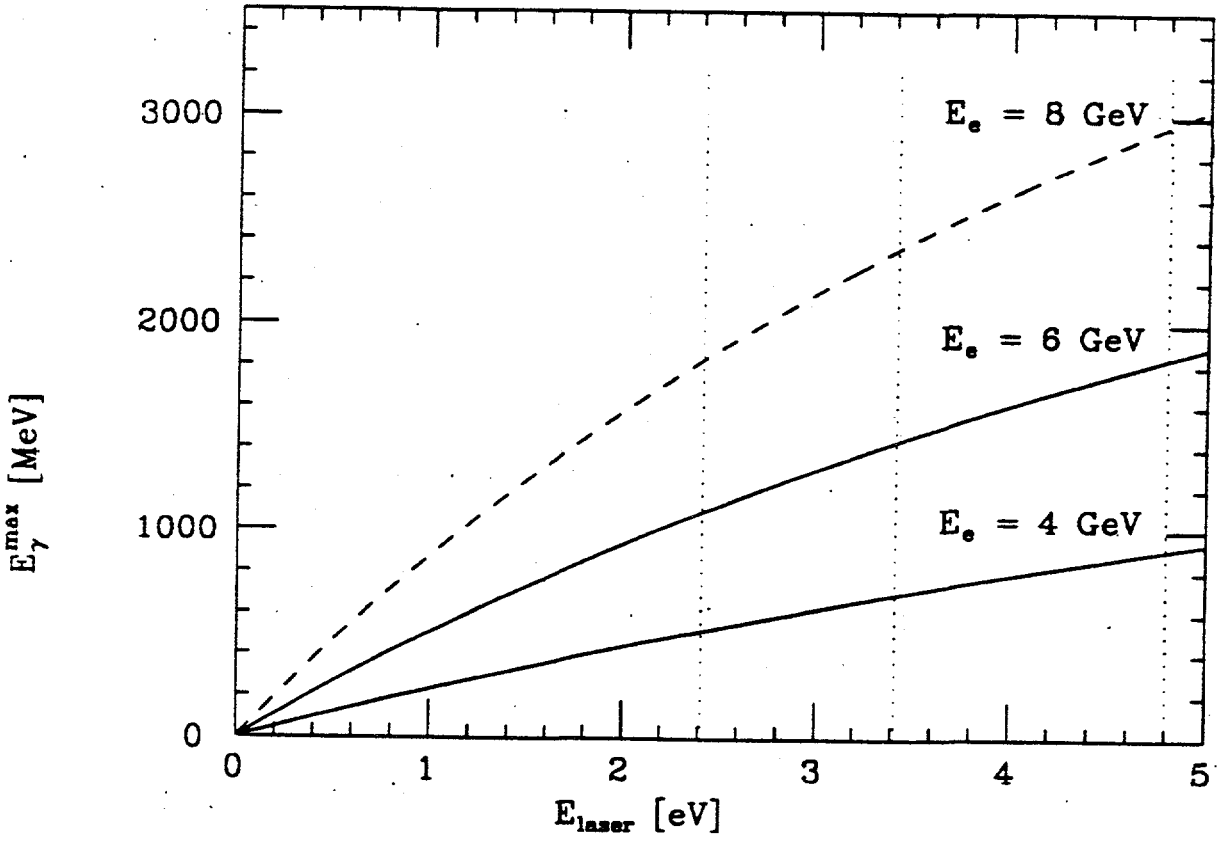

FIG. 4. Backscattered γ energy as a function of incident photon energy and electron beam energy. The first (second) dotted line corresponds to the 2.4 eV green (3.4 eV UV) line in an argon ion laser; the third corresponds to a frequency doubled 2.4 eV line.

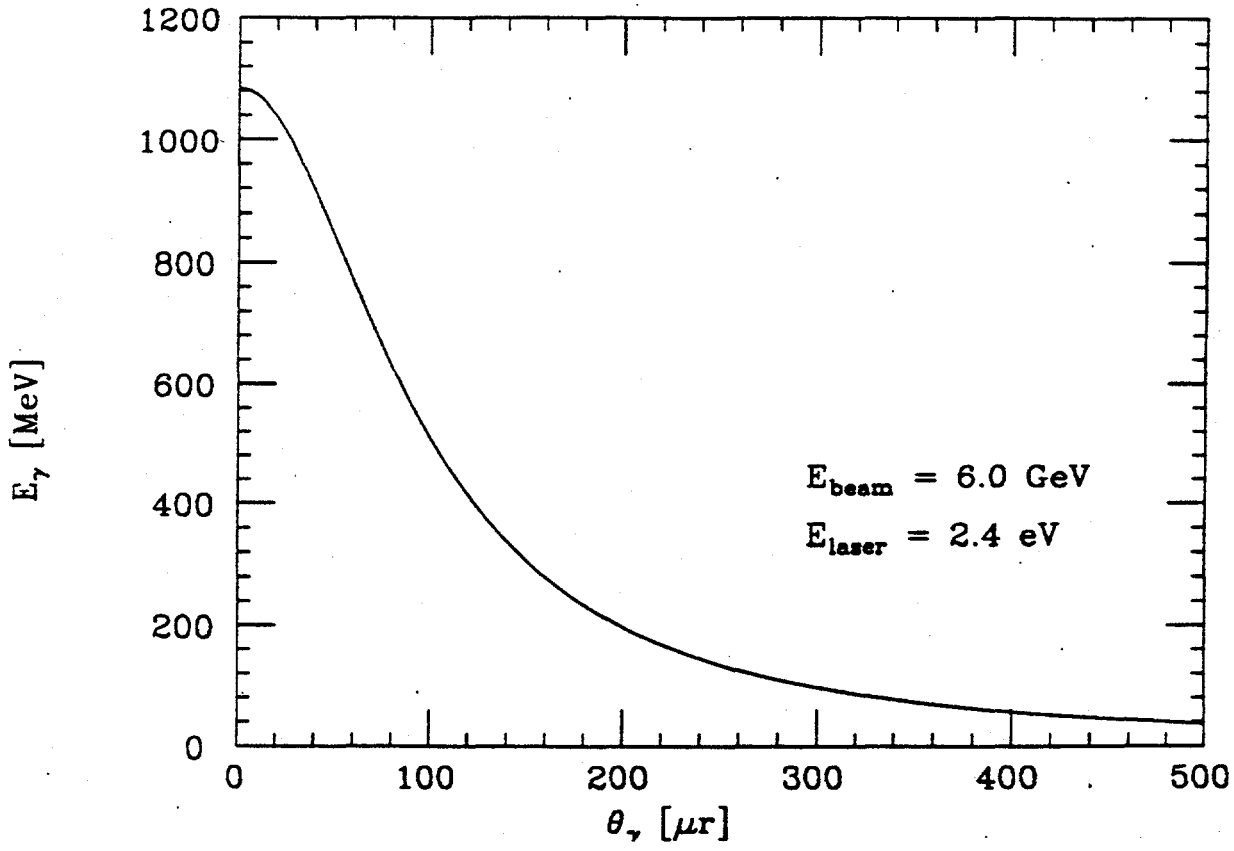

FIG. 5. Backscattered γ energy is dependent on the laboratory scattering angle with respect to the electron direction. The actual energy-angle correlation will be slightly diffused due to the ± 20 μr divergence of the electron beam.

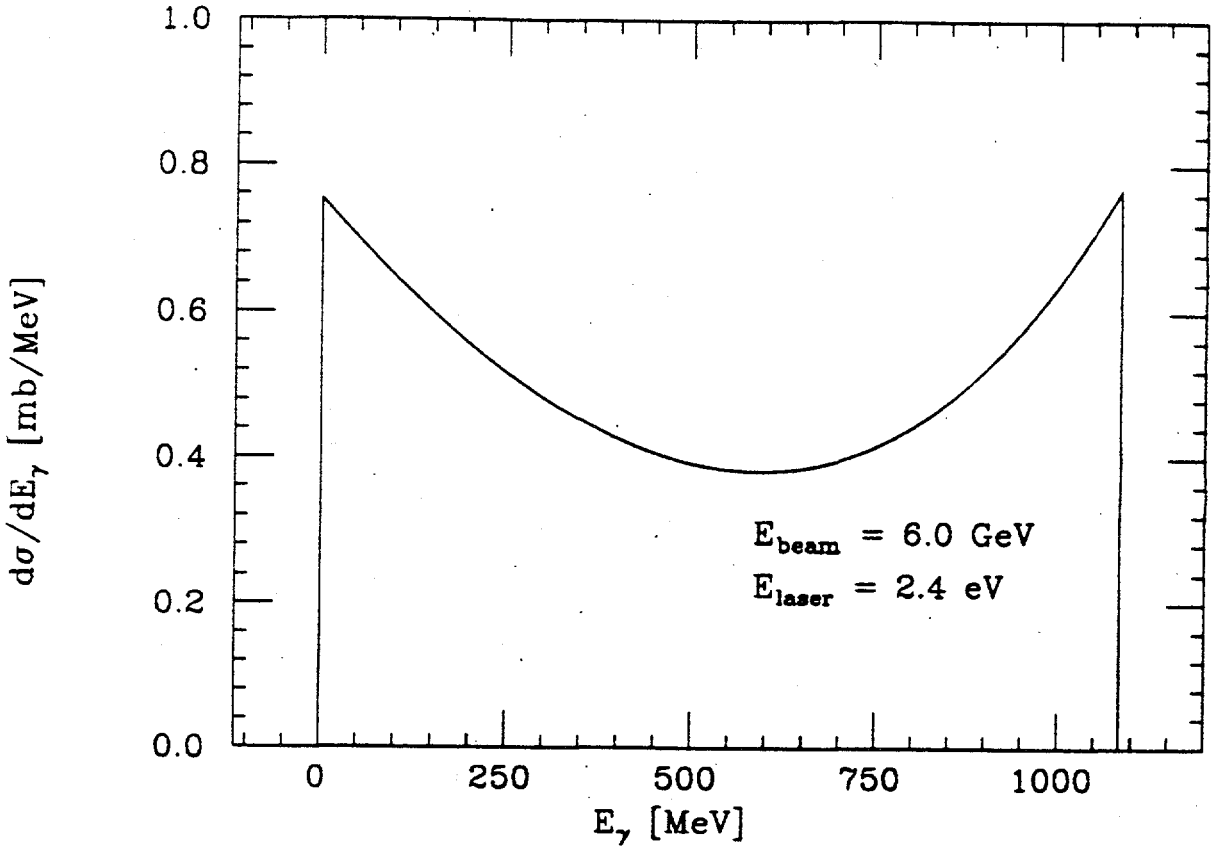

FIG. 6. Differential cross section as a function of γ energy.

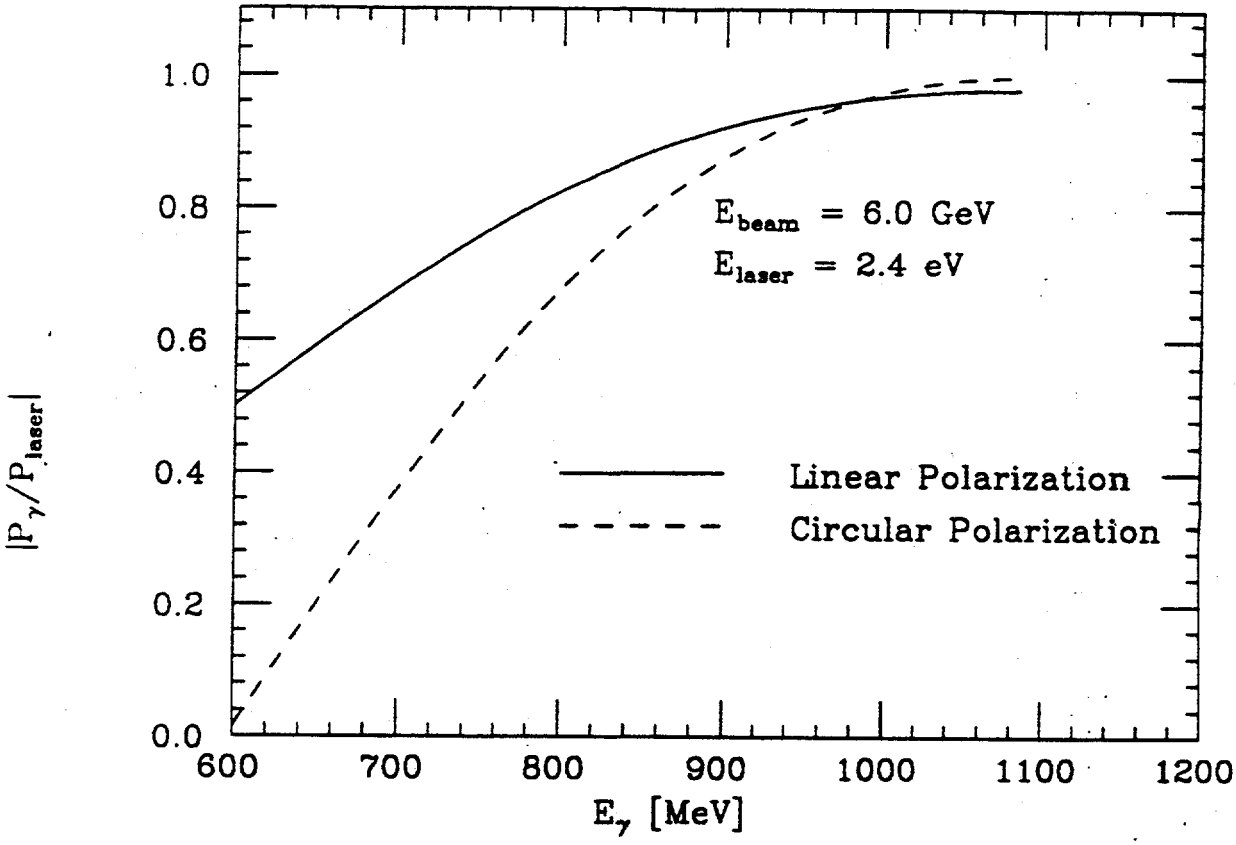

FIG. 7. Backscattered γ polarization as a fraction of the incident laser polarization.

FIG. 8. Spectra of γ-ray energies produced at LEGS for different combinations of laser and storage-ring energies (*top*). The tagged photon resolution (inset) is 5.5 MeV FWHM, nearly independent of energy. The degree of linear polarization is shown in the bottom panel.

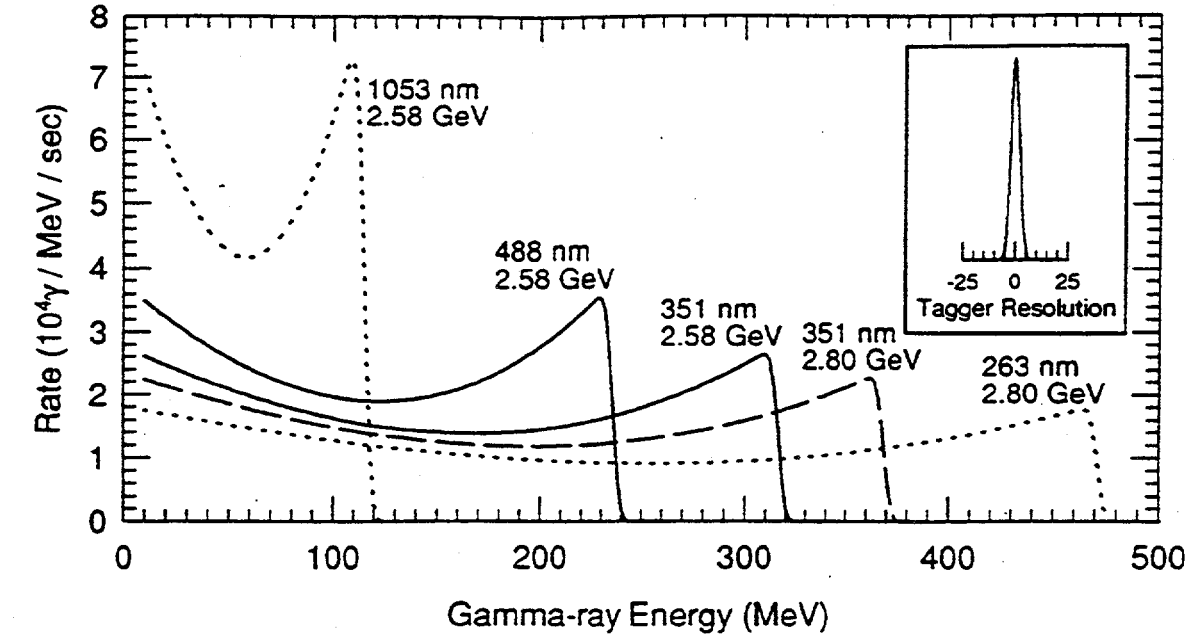

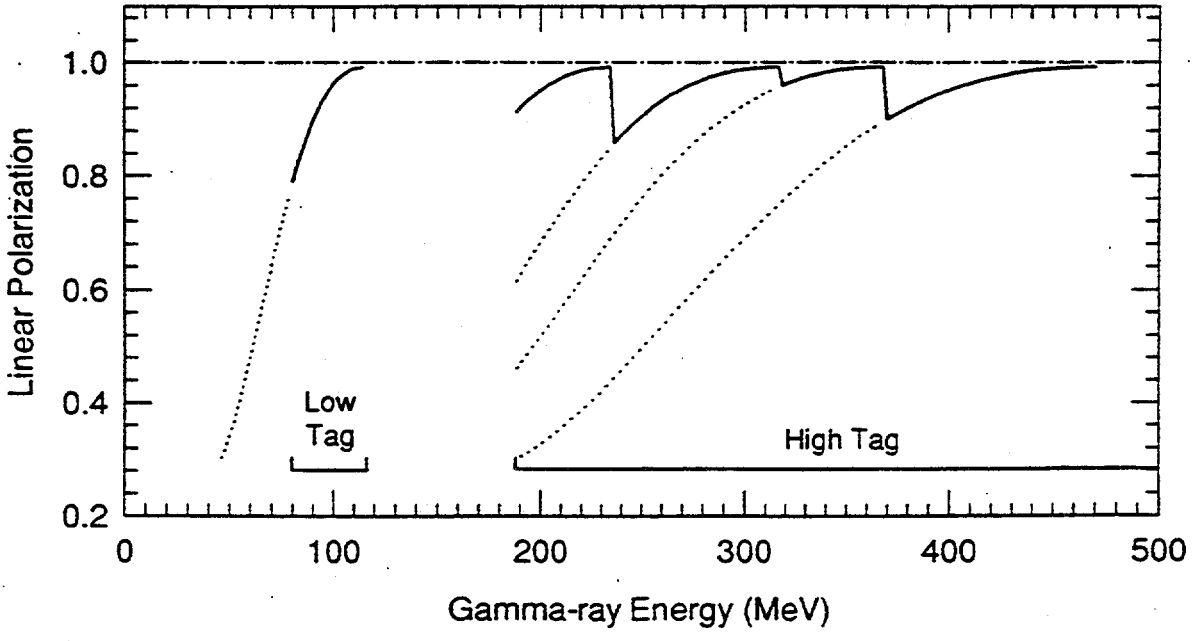

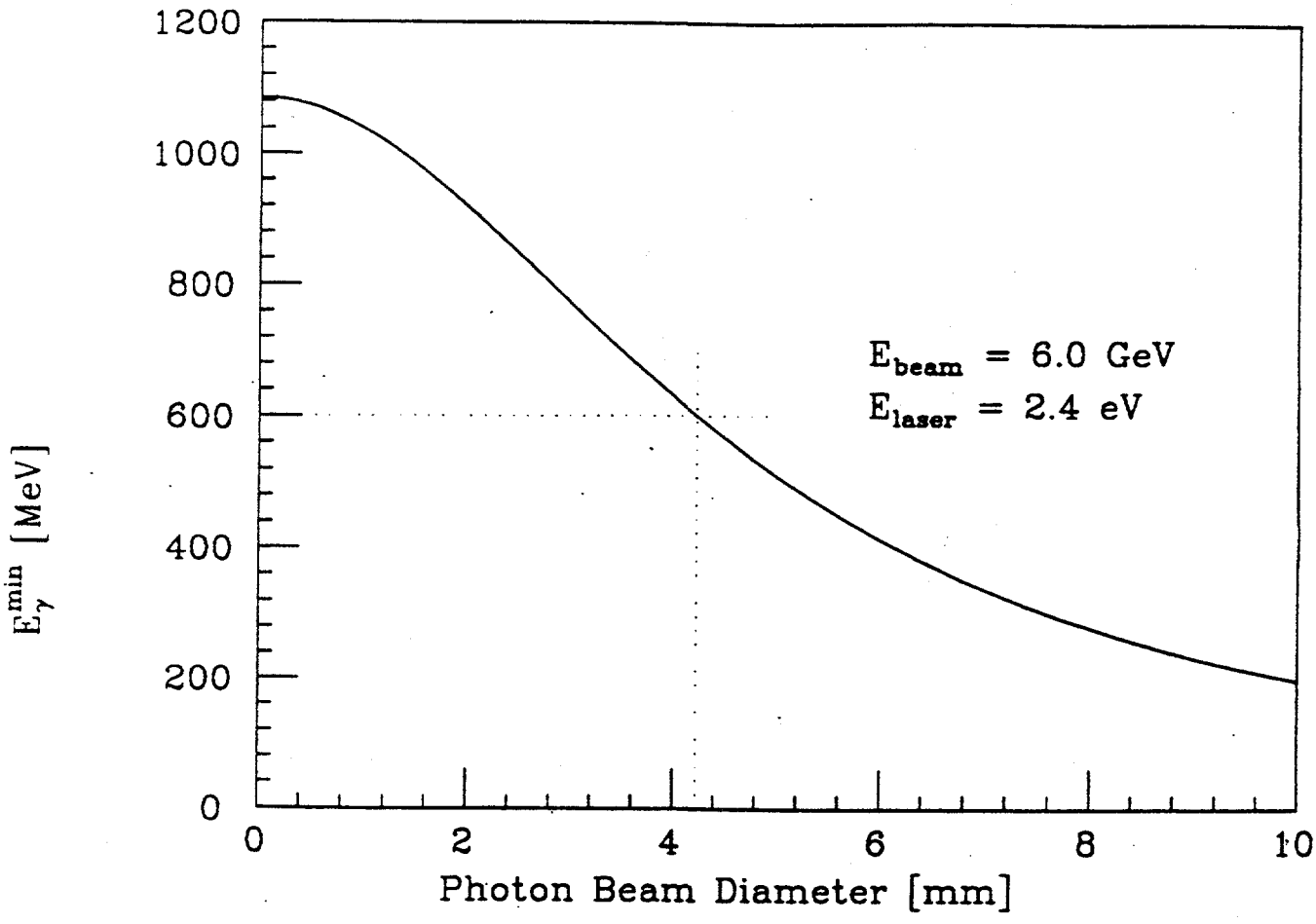

FIG. 9. Backscattered γ spot size 25 meters from a point source. Including the 4 m length of laser-electron interaction region and the effects of the $\pm 20\mu r$ divergence of the electron beam increases the spot size by $\approx$10%. By collimating we can effectively filter the γ energy.

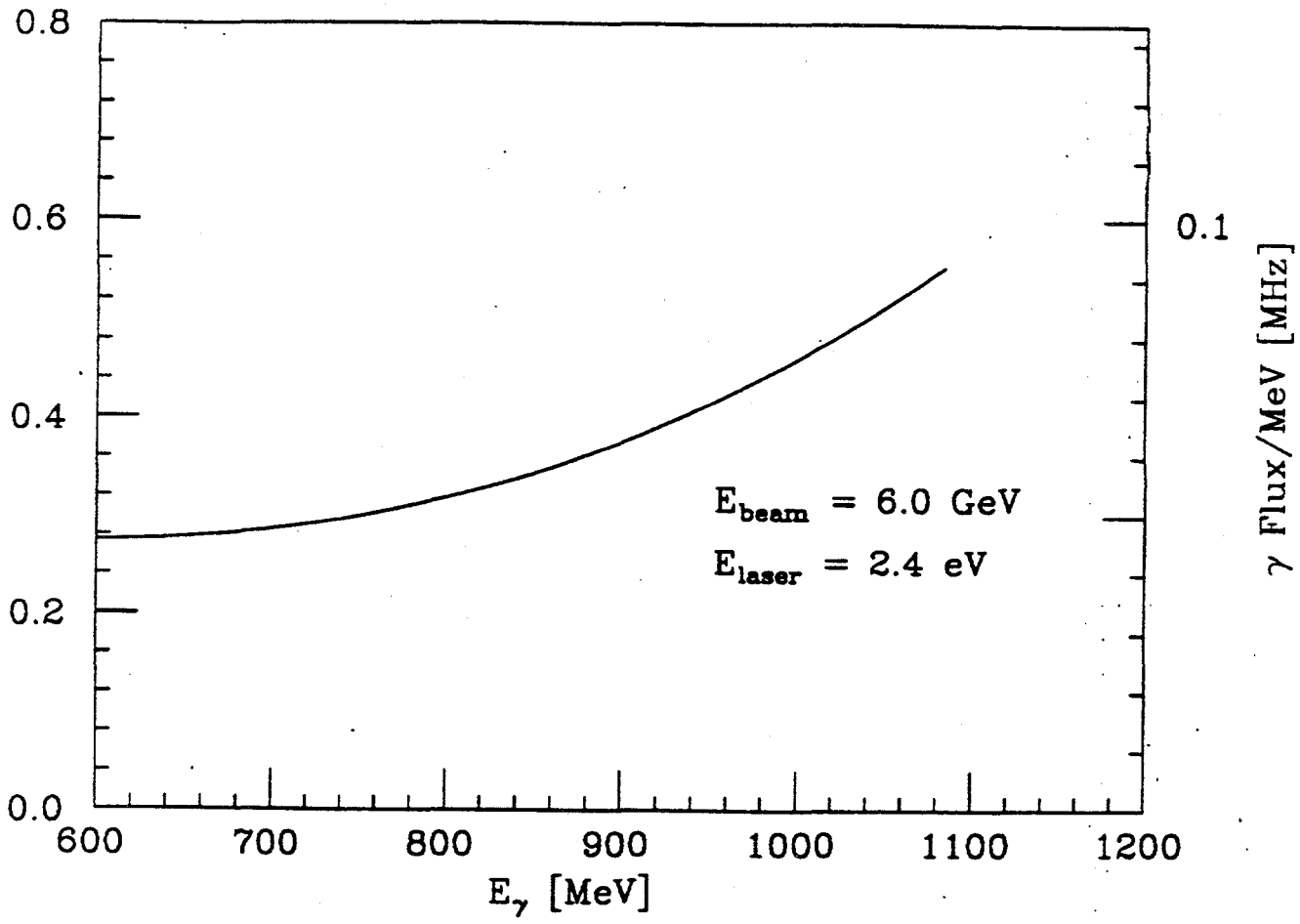

FIG. 10. Backscattered γ flux as a function of γ energy. The assumptions for this graph include a 1.6 μA, 6 GeV electron beam with a β^* of 2.5 m (σ^* of 50 μm) and a 10 watt argon ion laser using the 2.4 eV line with a cavity gain of 30,000 ($\beta^* = 0.44$ m, $\sigma^* = 100$ μm).

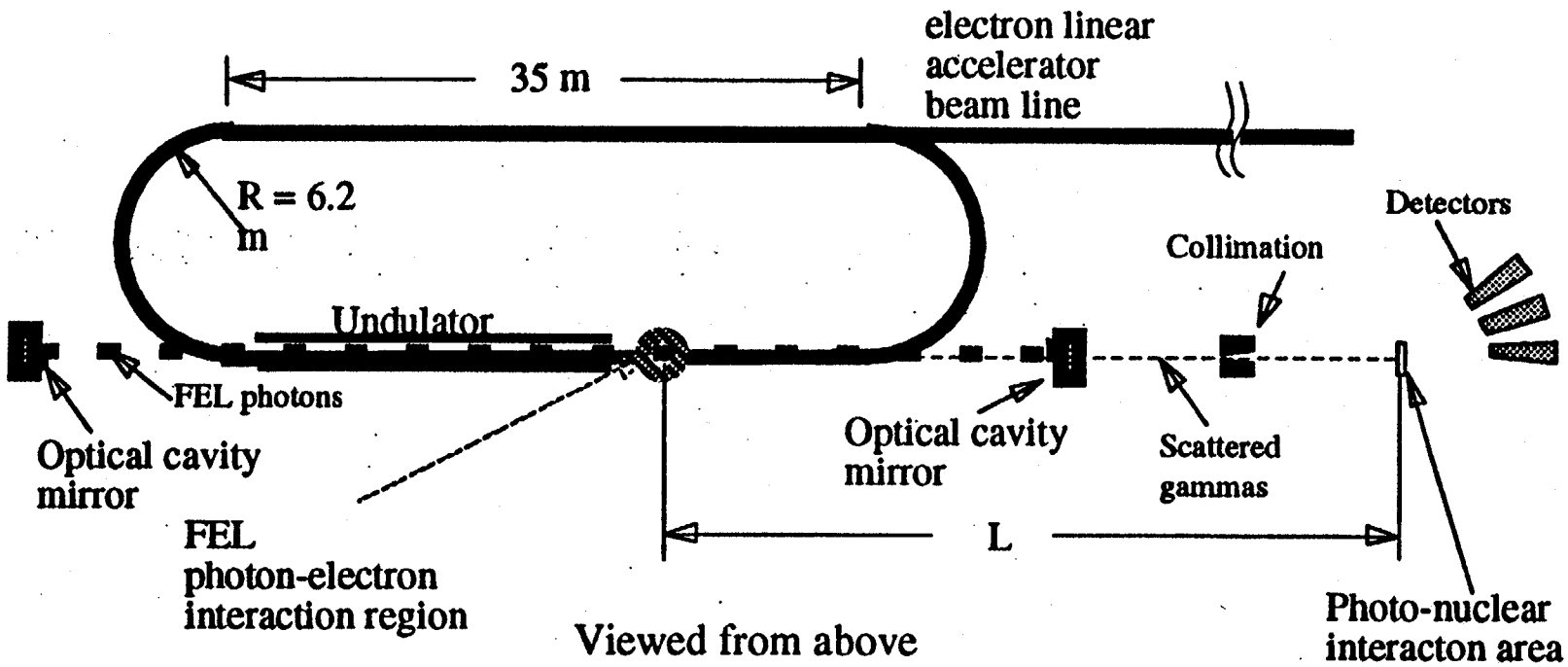

FIG. 11. Schematic layout of the TUNL/DFELL electron storage ring and Compton backscattering $\vec{\gamma}$ facility. Figure taken from reference [23].

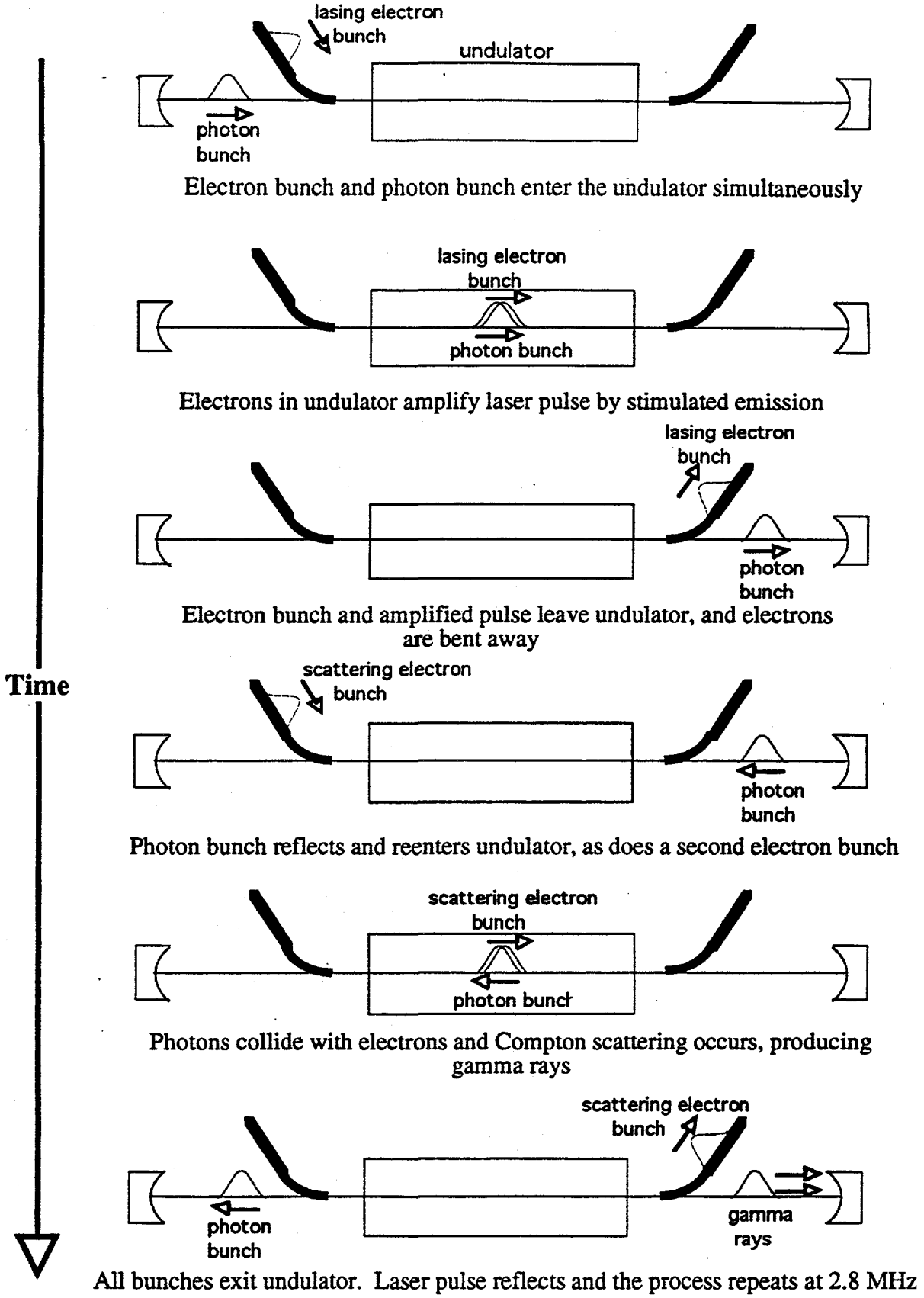

FIG. 12. Schematic timing sequence of the TUNL/DFELL $\vec{\gamma}$ source.

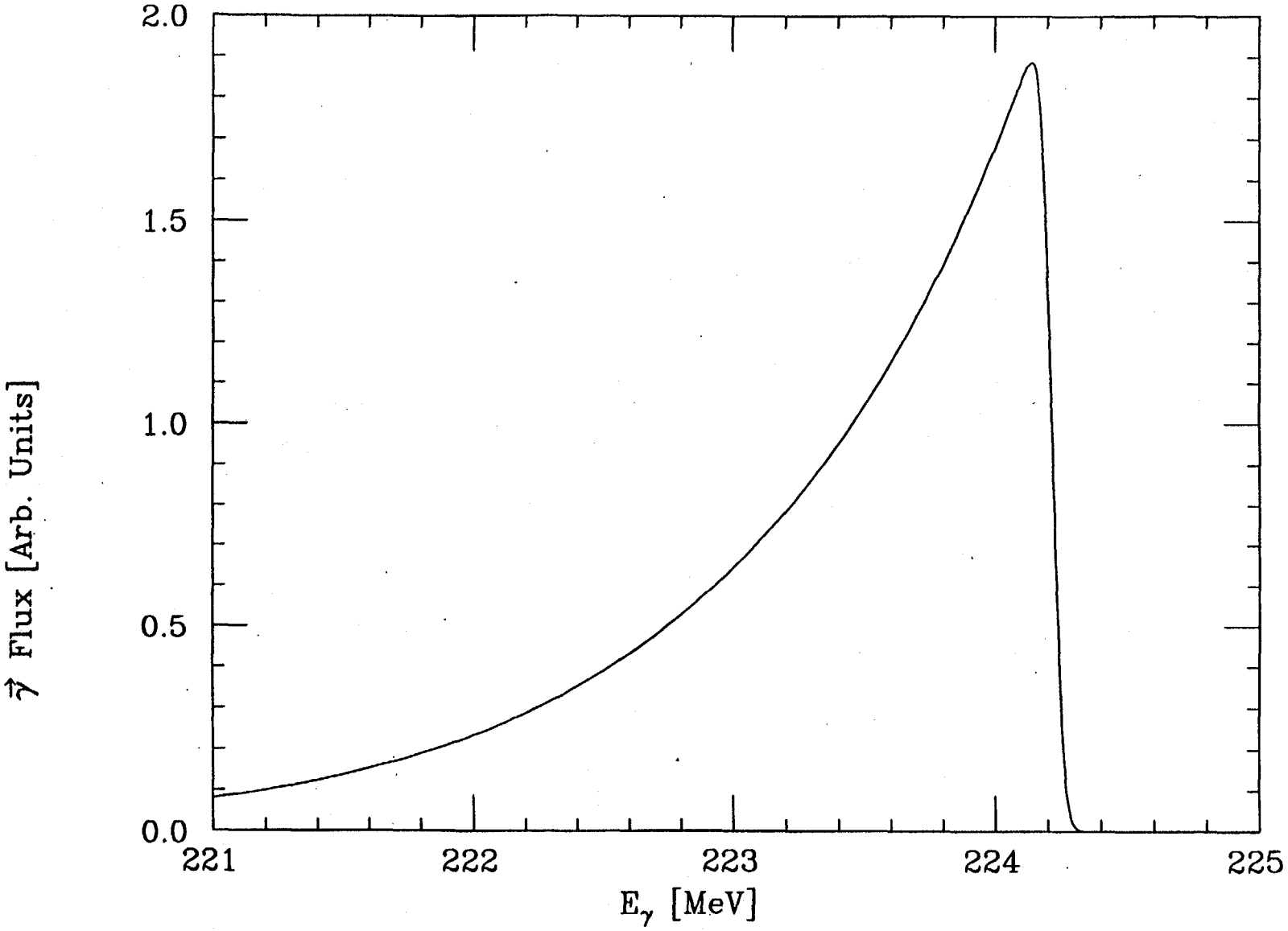

FIG. 13. Energy spectrum of TUNL/DFELL $\vec{\gamma}$ beam for an electron energy of 1 GeV, an FEL photon energy of 12.5 eV, and a circular collimator of radius 1 mm located 50 m from the photon-electron collision point.

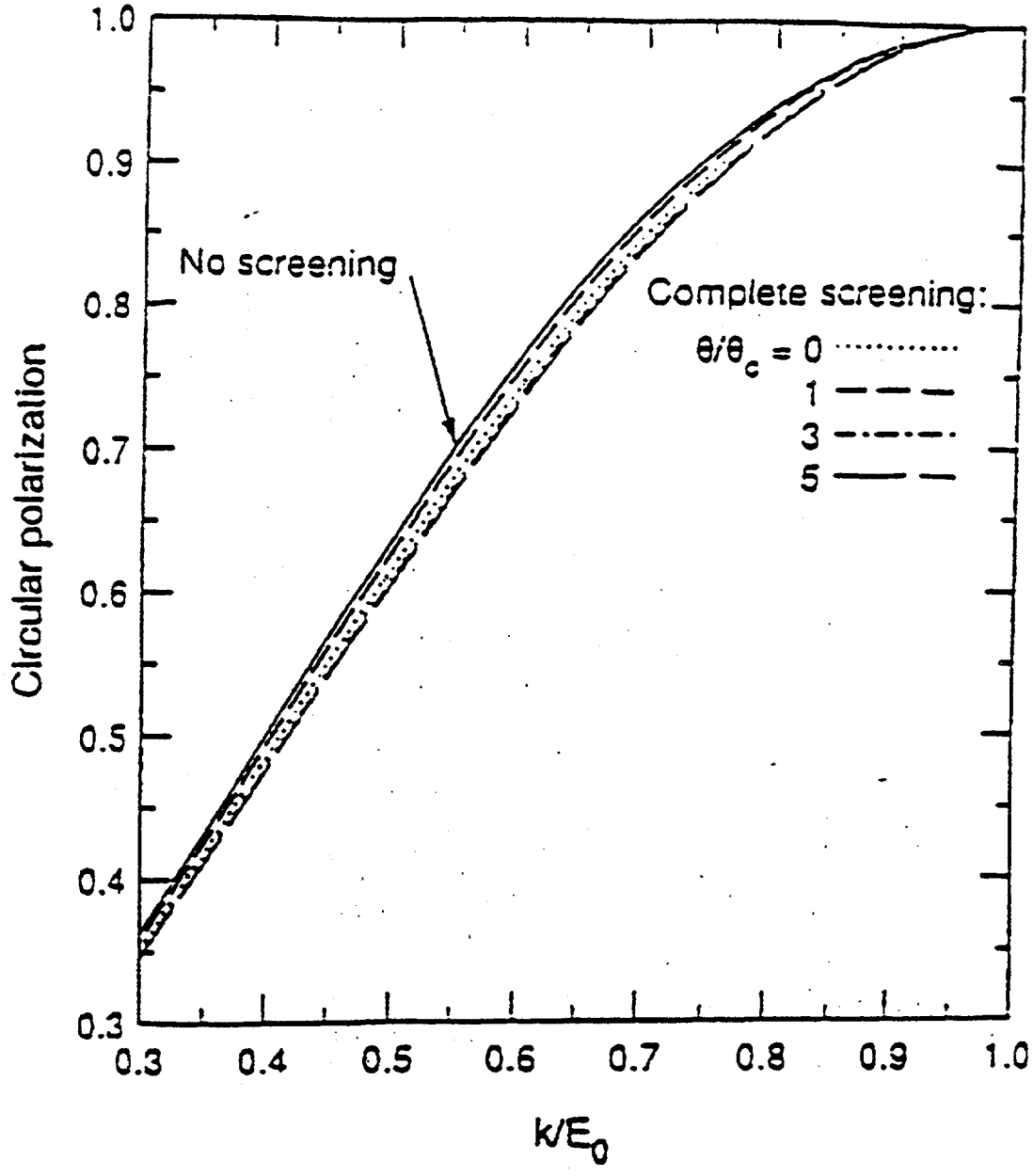

FIG. 14. Circular polarization of bremstrahlung from a 100% polarized electron. The different "complete screening" curves show the dependence on photon emission angle in units of $\theta_c = m_e/E_0$.

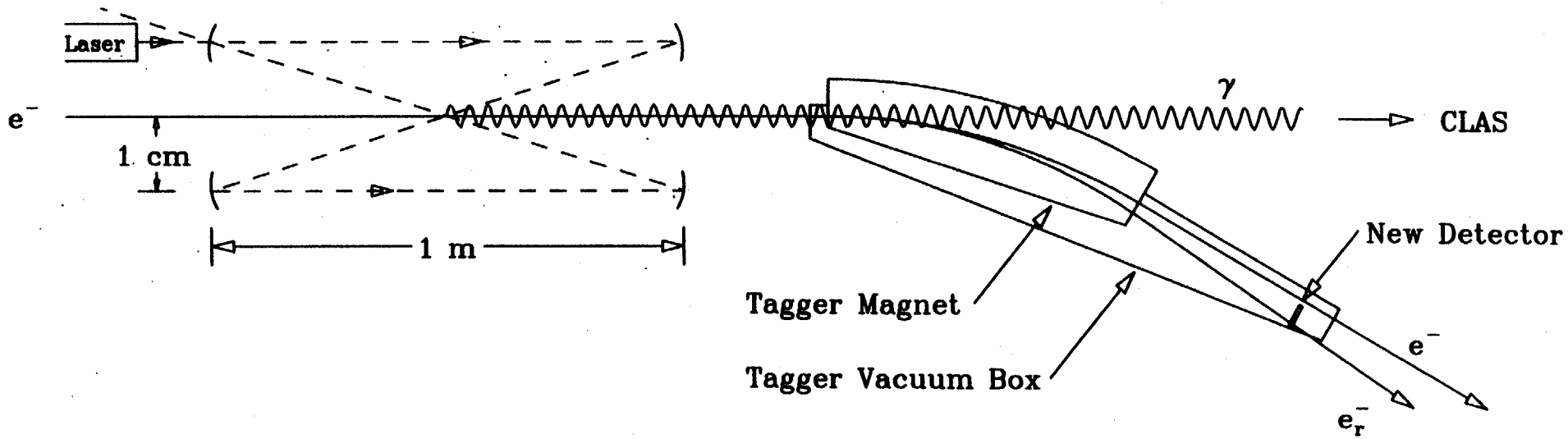

FIG. 15. Schematic layout of the Compton backscattering $\vec{\gamma}$ source proposed for CEBAF Hall B